



Geodynamics of the Yellowstone hotspot and mantle plume: Seismic and GPS imaging, kinematics, and mantle flow

Robert B. Smith^{a,*}, Michael Jordan^{a,f}, Bernhard Steinberger^b, Christine M. Puskas^a, Jamie Farrell^a, Gregory P. Waite^{a,c}, Stephan Husen^{a,d}, Wu-Lung Chang^{a,g}, Richard O'Connell^e

^a Department of Geology and Geophysics, University of Utah, Salt Lake City, Utah

^b Center for Geodynamics, Geological Survey of Norway, Trondheim, Norway

^c Department of Geological and Mining Engineering and Sciences, Michigan Technological University, Houghton, Michigan

^d Swiss Seismological Service, Swiss Federal Institute of Technology, Zurich, Switzerland

^e Department of Earth and Planetary Sciences, Harvard University, Boston, Ma

^f Seismic and Reservoir Technology, SINTEF Petroleum Research, Trondheim, Norway

^g Department of Earth Sciences, National Central University, Taiwan

ARTICLE INFO

Article history:

Received 11 June 2008

Accepted 15 August 2009

Available online 6 September 2009

Keywords:

Yellowstone
Snake River Plain
volcanism
hotspot
plume
tomography
earthquakes
dynamics
kinematics
convection

ABSTRACT

Integration of geophysical and geological data show that the Yellowstone hotspot resulted from a mantle plume interacting with the overriding North America plate, a process that has highly modified continental lithosphere by magmatic and tectonic processes and produced the 16–17 Ma, 700-km-long Yellowstone–Snake River Plain (YSRP) silicic volcanic system. Accessibility of the YSRP allowed large-scale geophysical projects to seismically image the hotspot and evaluate its kinematic properties using geodetic measurements. Seismic tomography reveals a crustal magma reservoir of 8% to 15% melt, 6 km to 16 km deep, beneath the Yellowstone caldera. An upper-mantle low-P-wave-velocity body extends vertically from 80 km to 250 km beneath Yellowstone, but the anomalous body tilts 60°WNW and extends to 660 km depth into the mantle transition zone. We interpret this conduit-shaped low-velocity body as a plume of up to -3.5% V_p and -5.5% V_s perturbation that corresponds to a 1–2% partial melt. Models of whole mantle convection reveal eastward upper-mantle flow beneath Yellowstone at relatively high rates of 5 cm/yr that deflects the ascending plume into its west-tilted geometry. A geodynamic model of the Yellowstone plume constrained by V_p and V_s velocities and attenuation parameters suggests low excess temperatures of up to 120 K, corresponding to a maximum 2.5% melt, and a small buoyancy flux of 0.25 Mg/s, i.e., properties of a cool, weak plume. The buoyancy flux is many times smaller than for oceanic plumes, nonetheless, plume buoyancy has produced a ~400-km-wide, ~500-m-high topographic swell centered on the Yellowstone Plateau. Contemporary deformation derived from GPS measurements reveals SW extension of 2–3 mm/yr across the Yellowstone Plateau, one-fourth of the total Basin–Range opening rate, which we consider to be part of Basin–Range intraplate extension. Locally, decadal episodes of subsidence and uplift, averaging ~2 cm/yr, characterize the 80-year Yellowstone caldera monitored history and are modeled as hydrothermal–magmatic sources. Moreover a recent episode, 2004–2009, of accelerated uplift of the Yellowstone caldera at rates up to 7 cm/yr has been modeled as resulting from magmatic recharge of a 10-km-deep sill at the top of the crustal magma reservoir. Regionally, gravitational potential energy of the Yellowstone swell drives the lithosphere southwest and “downhill” from the Yellowstone Plateau 400 km where it coalesces with Basin–Range province-wide westward extension. Based on the geometry and its assumed 660 km depth, we extrapolate the plume source southwest to its original location at 17 Ma and 600 km southwest and 200 km north of the YSRP. Importantly, this location is beneath the southern part of the Columbia Plateau flood basalt field of the same age and implies that the Yellowstone mantle plume may be the common source for both of these large volcanic fields. Our time-progression model suggests that the original plume head rose vertically behind the Juan de Fuca plate, but at ~12 Ma it lost the protection of the subducting plate from eastward mantle flow and encountered cooler, thicker continental lithosphere, becoming entrained in eastward upper-mantle flow. These results reveal that Yellowstone plume–plate processes have had a profound effect on Late Cenozoic geologic evolution and topography of a large part of the western U.S.

© 2009 Elsevier B.V. All rights reserved.

* Corresponding author. Department of Geology and Geophysics, 115 S. 1460 E., rm. 243, Sutton Bldg., University of Utah, Salt Lake City, Utah, 84112.
E-mail address: robert.b.smith@utah.edu (R.B. Smith).

1. Introduction

In its isolation from a plate boundary, the Yellowstone hotspot is a classic example of a continental hotspot. It is responsible for creating the age-transgressive 700-km-long Yellowstone-Snake River Plain (YSRP) silicic volcanic province over the last ~17 Ma and has systematically modified the composition and strength of the overriding North America plate (Figs. 1, 2) (Morgan, 1971, 1972; Matthews and Anderson, 1973; Smith and Sbar, 1974; Armstrong et al., 1975; Smith, 1977; Bonnicksen, 1982; Leeman, 1982; Morgan et al., 1984; Pierce and Morgan, 1990, 1992; Kuntz et al., 1992; Smith and Braile, 1994; Morgan et al. 1995; DeNosaquo et al., 2009-this volume). However the

sub-lithospheric structure of the YSRP and hotspot-related magmatic processes have been poorly understood largely because of the lack of definitive data (e.g., Morgan, 1972; Smith et al., 1974; Smith and Sbar, 1974; Eaton et al., 1975; Anders et al., 1989; Pierce and Morgan, 1990, 1992; Christiansen et al., 2002).

The first part of this paper describes the geophysical and geological signature of the active part of the YSRP, the 2.05-Ma Yellowstone Plateau volcanic field, centered at Yellowstone National Park (hereafter termed Yellowstone, Fig. 3) and how its tectono-magmatic processes have played a key role in the Cenozoic evolution of the western U.S. (Boyd, 1961; Christiansen, 1972; Smith and Sbar, 1974; Smith, 1977; Christiansen, 1984; Pierce and Morgan, 1990; Draper,

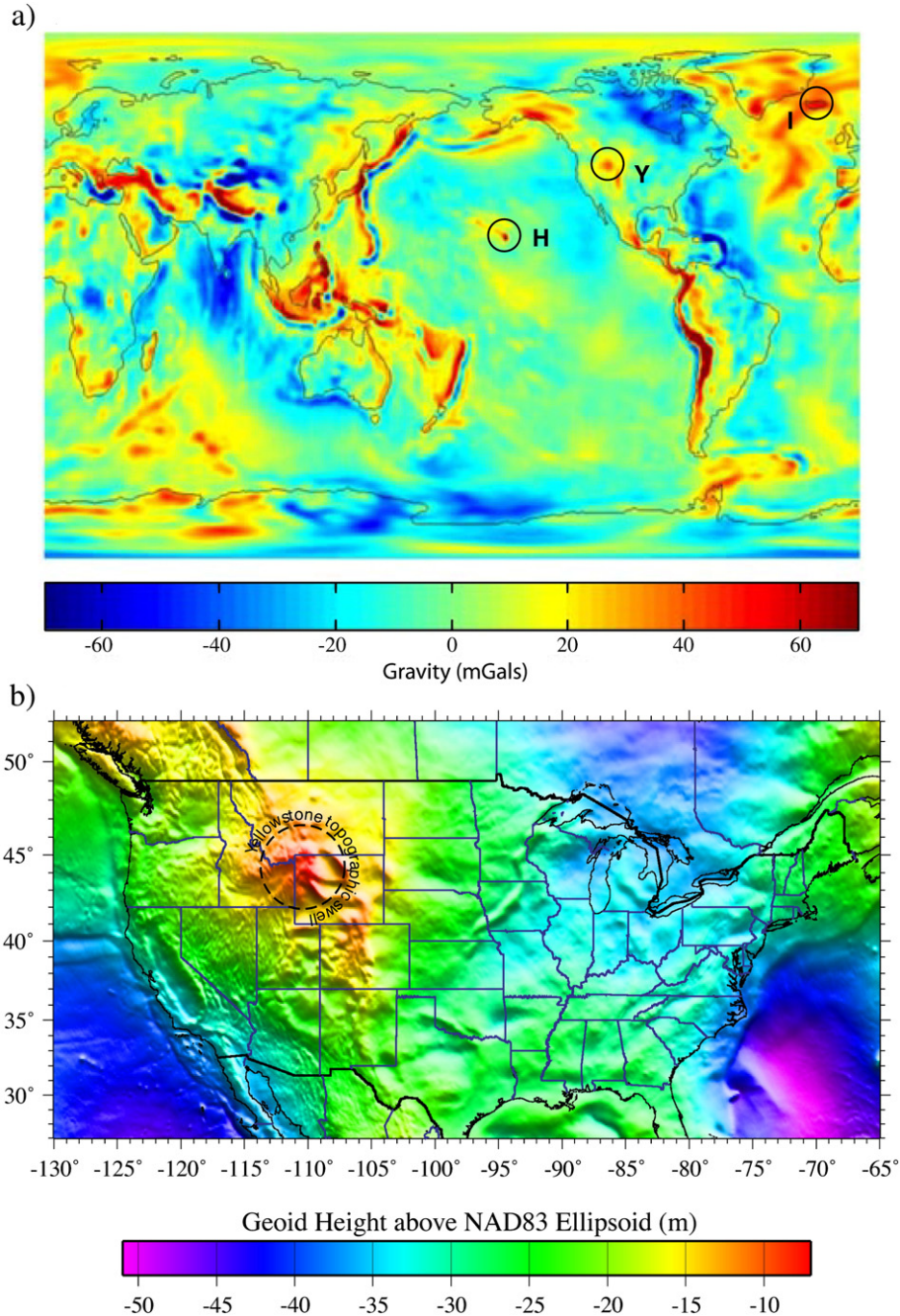


Fig. 1. Gravity signatures of global hotspots. (a) Global free-air gravity anomaly of some notable hotspots including Hawaii, Iceland, and Yellowstone in mGal (Tapley et al., 2005). These anomalies have wavelengths the order of 1000 km long and relative amplitudes of +20 to +40 mGal; and (b) North America geoid map (Roman et al., 2004) showing the Yellowstone geoid anomaly. Yellowstone has a ~500-km-wide topographic swell.

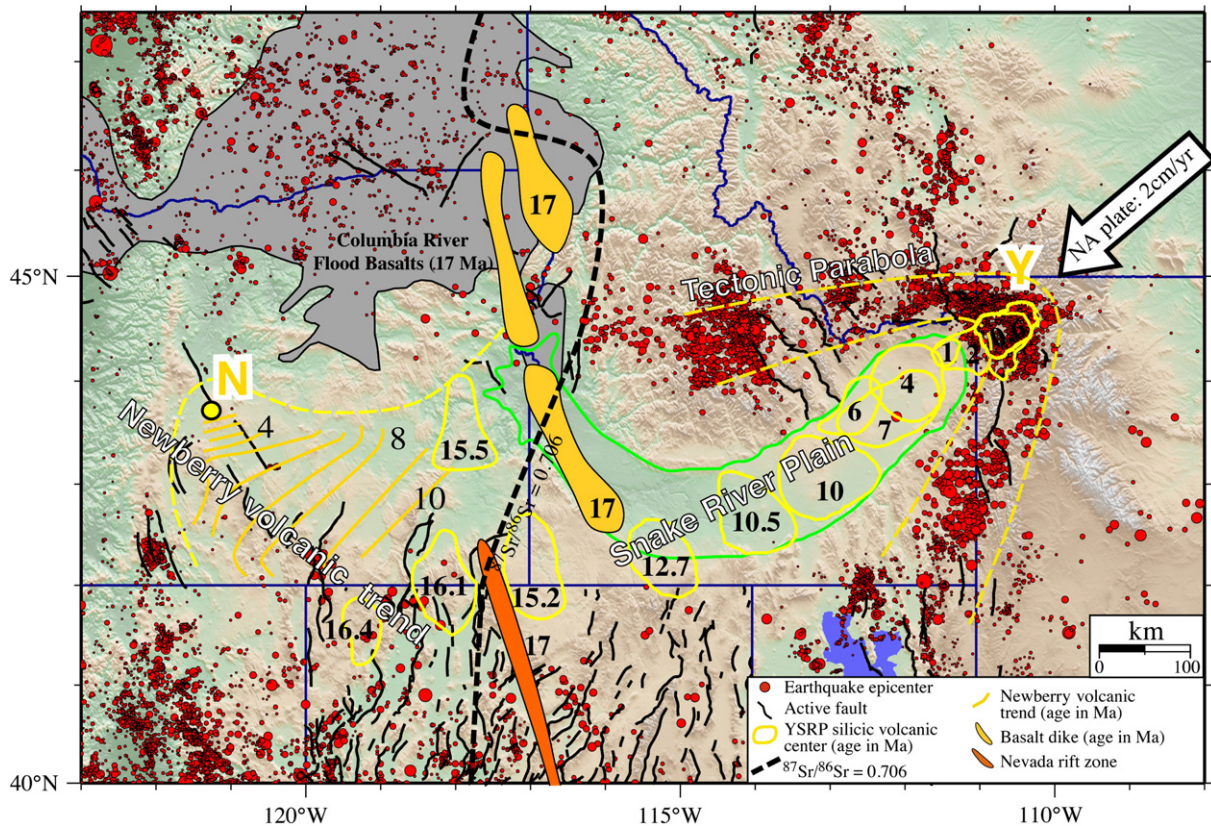


Fig. 2. Track of the Yellowstone hotspot (Y) (after Smith and Siegel, 2000) showing the relative motion of age-transgressive ESRP silicic volcanic centers (Armstrong et al., 1975; Smith and Braile, 1984; Pierce and Morgan, 1990, 1992; Kuntz et al., 1992; Smith and Braile, 1994; Perkins and Nash, 2002) opposite to the direction of North America plate motion (large arrow) (Smith and Sbar, 1974). The topographically low area occupied by the Snake River Plain is outlined in green. Centers of post-17 Ma silicic volcanism (in yellow) contain multiple caldera-forming eruptions (Christiansen, 1984, 2001). The area of Columbia River flood basalts is gray (Perkins and Nash, 2002). Red dots are historic earthquake epicenters taken from compilations of the University of Utah of M1.5 – 7.5 earthquakes. Black lines show late Quaternary faults; Cenozoic basaltic dikes (age in Ma) are shown in yellow and orange (Zoback and Thompson, 1978; Camp, 1995; Glen and Ponce, 2002). $^{87}\text{Sr}/^{86}\text{Sr}$ isotope boundary for the 0.706 values is shown as a black-dashed line and is interpreted to separate continental lithosphere to the east and oceanic lithosphere to the west (Armstrong et al., 1977; Farmer and DePaolo, 1983). The tectonic parabola is defined by the bow-shaped pattern of high topography and seismicity surrounding the YSRP (yellow dashed lines) (Smith et al., 1985; Smith and Arabasz, 1991; Anders and Sleep, 1992). The Newberry trend of silicic volcanism extends NW across southeast Oregon to the Newberry caldera (N) (MacLeod et al., 1976).

1991; Pierce and Morgan, 1992; Smith and Braile, 1994; Parsons et al., 1994; Christiansen, 2001). We then present new seismic images and a geodynamic model for an upper mantle plume that accounts for the dynamics of the YSRP. We discuss the intraplate kinematics of the YSRP from GPS measurements and use derived seismic velocity data to constrain mantle density structure by modeling the Yellowstone geoid anomaly. We then evaluate the large-scale properties of whole-mantle convection of the western hemisphere and examine how mantle flow has influenced the geometry and location of the Yellowstone hotspot as well as the dynamics of the modeled upper-mantle plume. Our discussion concludes by speculating on the 17-Ma history of the Yellowstone plume by extrapolating the North America plate backward in time and space over its upper mantle source to a location that coincides with a mantle magma source location common to the YSRP, the High Lava Plains, and the large igneous province (LIP) Columbia Plateau flood basalt field features.

A number of questions on the origin of the Yellowstone hotspot are discussed: (1) is the upper-mantle conduit-shaped low-velocity body beneath Yellowstone a plume? (2) How much of its physical properties result from upper mantle flow and plume-plate interaction processes? (3) How does mantle flow affect the geometry of the plume? (4) Does Basin-Range lithospheric extension amplify Yellowstone volcanism? We address these questions as basic objectives of this paper. We note that our study emphasizes that Yellowstone is a unique “window” into Earth’s processes providing a key view of lithospheric magmatism, plate construction and destruction, contemporary deformation, etc., leaving a well defined signature that can be

compared with hotspot-plate interactions around the globe (e.g., Crough, 1983; Davies, 1988; Richards et al., 1989; Anders and Sleep, 1992; Courtillot et al., 2003; Burrov and Guillou-Frottier, 2005).

It is important to note that the terms melt and hotspot anomalies have been employed by some authors (see Foulger et al., 2005 for a summary) for low-velocity mantle features that are not necessarily ascribed to a plume. In our paper, we accept the term plume for our imaged low-velocity upper-mantle body as a conduit of buoyantly ascending melt. This definition is in other mantle studies (Condie, 2001) and will be discussed in later sections.

1.1. Hotspots and plumes

Largely because of their presumed association with the Earth’s deep interior, plumes of ascending magma are commonly thought of as the sources of volcanic hotspots, i.e. areas of long-lived concentrated volcanism (Wilson, 1963; Dietz and Holden, 1970; Morgan, 1971; Crough, 1978). While most of Earth’s volcanism is associated with plate boundaries, including mid-ocean ridges and subduction zones, some hotspots such as Yellowstone occur within a continental plate (Fig. 1).

Yellowstone is an example of a continental hotspot that is located 1600 km east of the western North American plate boundary. Earliest quantitative models of the Yellowstone hotspot and its hypothesized interaction with the North American and Juan de Fuca plates were constructed by calculating the intraplate vector motions made by Smith and Sbar (1974). They determined an apparent rate of 2.8 cm/yr

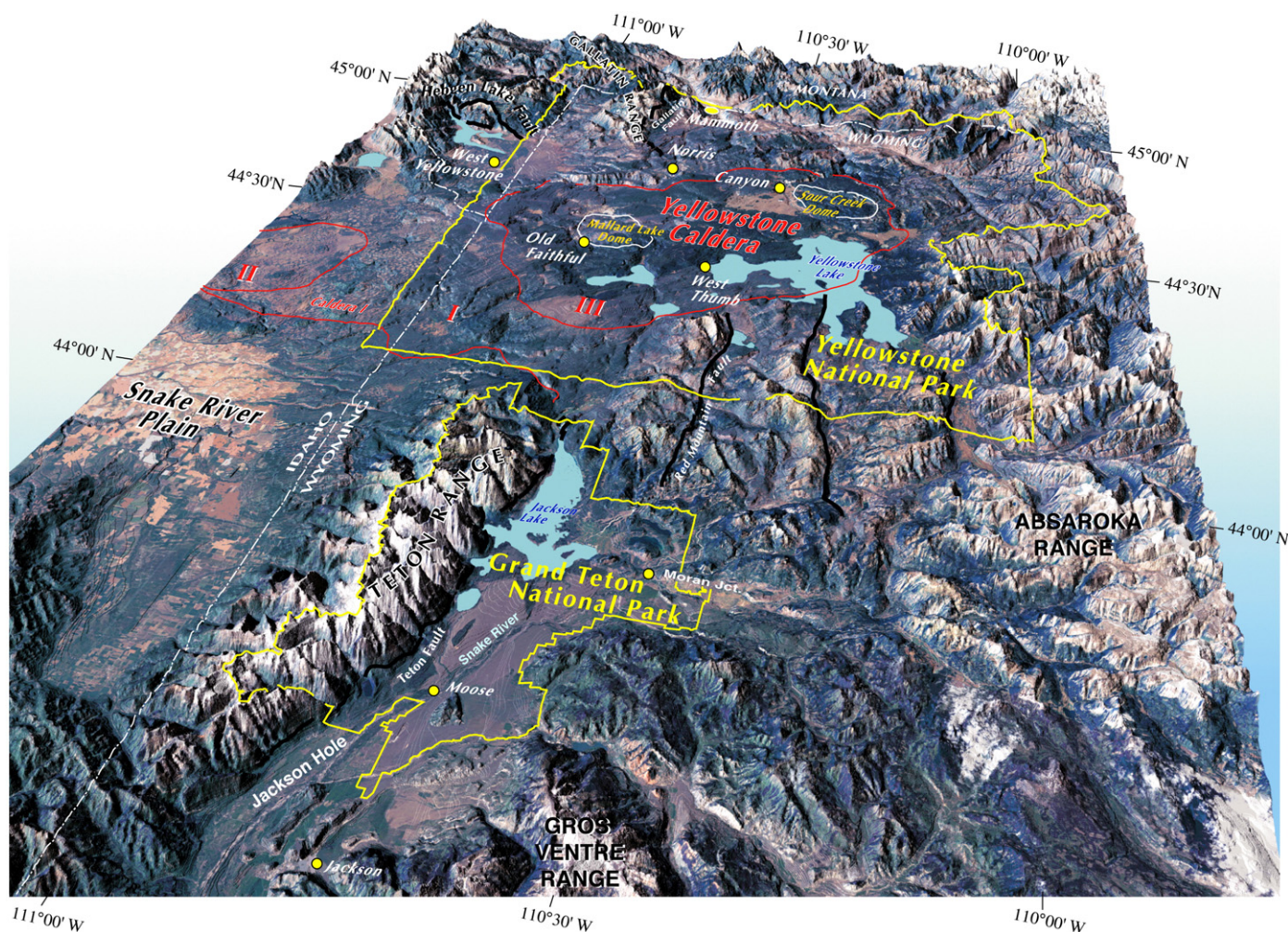


Fig. 3. Space view of Grand Teton and Yellowstone National Parks from LANDSAT satellite imagery overlain on digital elevation data. The caldera occupies a 60 km by 40 km-wide area of central Yellowstone National Park. Park boundaries are shown as yellow lines. Caldera boundaries are outlined in red and labeled I for the 2.05-Ma caldera, II for the 1.3-Ma Henrys Fork Caldera, and III for the 0.64-Ma Yellowstone Caldera. Resurgent domes are outlined in white. Local place names are marked with yellow circles. Modified image from Smith and Siegel (2000).

of plate motion at Yellowstone with an azimuth of $\sim 247^\circ$ using a pole of rotation for the North American plate given by Atwater (1970). This plate motion value was nearly identical to the direction determined by Armstrong et al. (1975, 1977) for the apparent motion of silicic age progression of the YSRP. Smith and Sbar (1974) also speculated on the process of plate-plume interaction, i.e. basal lithospheric shearing that accelerated the overriding plate in southwest direction and added a component of plate retardation to the northeast due to a small component shear traction in front of the plume.

In addition, Smith and Sbar (1974) and Smith (1977) showed that the contemporary stress field of the YSRP, determined by focal mechanisms of moderate to large western U.S. earthquakes and Late Quaternary fault orientations, was consistent with regional NW-SE extensional strain. Their model emphasized the importance of upper-mantle and plume-plate interactions for the Yellowstone hotspot and its effect over a large area of the western U.S.

Hotspots have distinct physical properties. The most notable features are linear, time-transgressive volcanic chains and broad topographic swells (Morgan, 1972; Crough, 1983; Davies, 1988; Sleep, 1990, 1992; Burov and Guillou-Frottier, 2005; Ito and van Keken, 2007). Topographic swells result from hot buoyant material at the base of the plate (Crough, 1978, 1983; Burov et al., 2007). Combined with the low-density plume, topographic swells result in a mass deficit at the hotspot that can produce notable gravity and geoid

anomalies such as those that characterize Yellowstone (Richards et al., 1988; Waschbusch and McNutt, 1994).

The significance of some important hotspots are also seen in the Earth's gravity field (Tapley et al., 2005), where notable long-wavelength positive anomalies, in excess of 800 km, are associated with the Hawaii, Iceland, and Yellowstone hotspots (Fig. 1). The amplitude of the long-wavelength Yellowstone gravity anomaly of ~ 35 mGal is thought to reflect reduced density of the lithosphere and asthenosphere across the ~ 800 -km width of the hotspot. Moreover, the Yellowstone hotspot is associated with a strong geoid anomaly of +15 m compared to the surrounding region over an 800-km width, similar to dimensions of oceanic hotspot swells (Fig. 1). An interpretation of the geoid anomaly is important because it represents an amalgam of isostatically uncompensated high topography and a broad zone of lithospheric-asthenospheric low-density material.

In traditional geologic thinking, plumes ascend vertically from the core-mantle boundary to the base of the lithosphere (Morgan, 1971, 1972). But new models (Steinberger et al., 2004) predict that plumes can rise upward along curved paths following the directions of convective mantle flow and may not necessarily have a core-mantle boundary source. Thus, hotspots are not necessarily fixed and horizontal mantle flow can tilt a plume, as we discuss in Section 4.6.

We note that the plume hypothesis has been conjectural, in part because plumes have not been reliably imaged by seismic tomography

or other direct methods. Practical limitations have been related to the lateral extent and density of seismic stations and the frequency content of seismic data required for tomographic inversion, which have prevented the resolution required to resolve anomalous low-wave-velocity bodies deeper than ~1000 km and less than ~100 km in diameter (see summary by [Nolet et al., 2007](#)). We will describe how the portable seismic array of the Yellowstone Geodynamic project was specifically designed to provide the necessary information to resolve the velocity structure of the upper mantle associated with the Yellowstone hotspot.

There are multiple ideas on the origin of plumes ([Courtilot et al., 2003](#)). One hypothesis argues that they form as upwellings associated with upper mantle convection, i.e. from the bottom of the transition zone at the 660-km discontinuity that separates the upper and lower mantle ([Malamud and Turcotte, 1999](#)). Another theory is that plumes originate in the lower mantle as a feature of whole-mantle convection ([Morgan, 1971, 1972; Olson et al., 1987; Courtilot et al., 2003](#)). And some authors ([Anderson, 2000; Foulger, 2002; Foulger et al., 2005](#)) argue that plumes do not exist at all, but are associated with volcanism related to shallow processes such as intraplate deformation resulting from the non-rigidity of plates, and to compositional variability in the upper mantle from de-homogenizing processes at ridges and subduction zones.

In particular [Christiansen et al. \(2002\)](#) argued against a plume origin for Yellowstone based on seismic data from a portable seismic array to image velocity variations at depths into the upper mantle. However their study provided limited seismic data over a sparse array with maximum width of ~600 km length and with short-period seismometers. Moreover this system could not fully respond to the longer-period P and S waves that are required for modern tomo-

graphic imaging and advanced imaging algorithms. See discussion in [Section 6](#).

We also note that the northwest time-progression of the Newberry silicic volcanic system and the Oregon High Lava Plains ([Jordan et al., 2004; Camp and Ross, 2004](#)) ([Fig. 2](#)) has been argued by some as a “mirror” image of the volcanic processes of the YSRP. However, we will not include a discussion of this volcanic system as it is beyond the scope of our study.

1.2. The Yellowstone Geodynamics Project

Because of Yellowstone’s accessibility, large-scale geophysical experiments have provided key data on the YSRP. The data acquisition component of the Yellowstone Geodynamics Project was implemented from 1999 to 2005 and included extensive seismic and GPS field surveys followed by processing, analysis, modeling, and integrated interpretation of the seismic and geodetic data. The field phase of the project deployed a temporary 80-station broadband and short-period array (50 temporary IRIS-PASSCAL stations and a special 30-station IRIS-PASSCAL telemetered array) over an area ~800 km in diameter centered on Yellowstone ([Fig. 4](#)) with station spacing of ~20 km to 35 km (see [Waite et al., 2005](#) for a detailed description of the seismic monitoring). The data sets were augmented with seismic data from five regional seismic networks in Montana, Wyoming, Idaho and Utah.

For assessing kinematics of the Yellowstone hotspot, 15 permanent GPS stations were installed in Yellowstone and the eastern Snake River Plain (ESRP) between 1996 and 2003, and 160 temporarily occupied GPS sites were observed between 1987 and 2003 ([Fig. 4](#)) (see [Puskas et al., 2007](#) for a detailed description of the geodetic

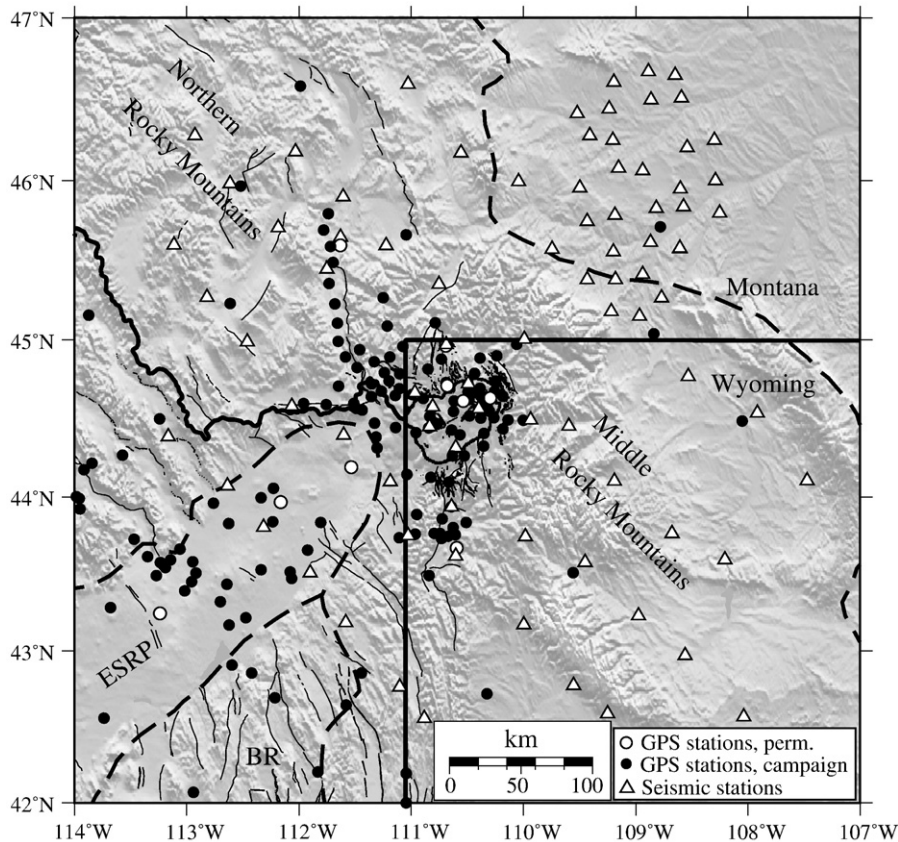


Fig. 4. Map of the seismic and GPS stations deployed for the 1999–2003 Yellowstone Hotspot Geodynamics project. The networks contain 166 seismic stations (broadband and short-period), 15 permanent GPS stations, and 150 campaign GPS stations ([Waite et al., 2006; Puskas et al., 2007](#)). Note the linear distribution of stations in 600-km long arrays with a NW azimuth designed to best record earthquakes at teleseismic distances (>1000 km) from the major seismic belts of the western Pacific and South America. Abbreviations are ESRP = eastern Snake River Plain; BR = Basin and Range.

monitoring). GPS data from the University of Utah and EarthScope PBO networks were also used.

1.3. Prior mantle plume studies

Most previous, large-scale tomographic studies have relied on permanent and temporary deployments of seismic stations that recorded teleseismic earthquakes, e.g., at Iceland, Hawaii, and the Eifel volcanic field, Europe (e.g., Ritter et al., 2001; Allen et al., 2002; Laske et al., 2006; Wolfe et al., 2008, respectively). Images from these studies reveal low P-wave velocity bodies beneath the associated areas of active volcanism but could not reliably resolve plume-like bodies at depths greater than ~400 km. The main limitation of these studies was the limited aperture width, seismometer bandwidth, and station density that did not have sufficient station-spacing to resolve seismic arrivals over the range of incidence angles required to sample deep-mantle velocity anomalies.

Early tomographic studies of the lithosphere and asthenosphere beneath the ESRP revealed a complex lithospheric velocity structure related to partial melting. The process of bimodal rhyolite-basaltic volcanism left a mid-crustal, high-density, high-velocity mafic sill (Sparlin et al., 1982; Annen et al., 2006; Shervais et al., 2006; Shervais and Hanan, 2008; Stachnik et al., 2008; DeNosaquo et al., 2009-this volume).

Saltzer and Humphreys (1997) used teleseismic data to infer mafic crustal underplating along the ESRP associated with past hotspot volcanism. The earliest tomographic studies of Yellowstone used sparse and relatively small seismic networks (Iyer et al., 1981; Kissling, 1988; Christiansen et al., 2002) that did not have sufficient aperture width or seismometer bandwidth to resolve images deeper than ~300 km. More recent work suggests that a narrow, conduit-shaped,

low-velocity feature interpreted as a plume extends from the upper mantle into the top of the mantle transition zone (Yuan and Dueker, 2005; Smith et al., 2005; Waite et al., 2006; Xue and Allen, 2007, 2009). The velocity anomaly is strongest at depths of 50 to 200 km with peak anomalies of -3% for V_p and -5.5% for V_s (Waite et al., 2006). The velocity reductions are interpreted to represent 1–2% partial melt at excess temperatures of 55–120 K, a relatively cool plume (Jordan, et al. 2004, 2005; Waite et al., 2005; Schutt and Dueker, 2008).

Anisotropy studies employing teleseismic shear-wave splitting measurements of the YSRP revealed an upper mantle that was not significantly perturbed by a mantle plume except for small anisotropy perturbations around Yellowstone. This led Waite et al. (2005) to conclude that a weak plume was responsible for the Yellowstone hotspot.

Geochemical models for Yellowstone suggest that the mantle transition zone, which separates the upper from the lower mantle, tends to be thinner when the hot rock of a plume intersects it, raising the 660-km discontinuity to shallower depths and depressing the 410-km discontinuity (Bina and Helffrich, 1994). Seismic receiver function analysis of the YSRP showed that the 410-km discontinuity deepens by 10-km near the intersection of the low-velocity anomaly identified by Yuan and Dueker (2005) and Waite et al. (2006) and that the 660-km discontinuity shallows by ~20 km beneath Yellowstone, a property that we used as a constraint for the tomography and dynamic modeling of the plume properties.

2. Volcano-tectonic setting of Yellowstone

Yellowstone hotspot volcanism is superimposed on the tectonics of the 30 Ma Basin and Range province, an 800-km-wide intraplate region of the western U.S. characterized by dominant normal to

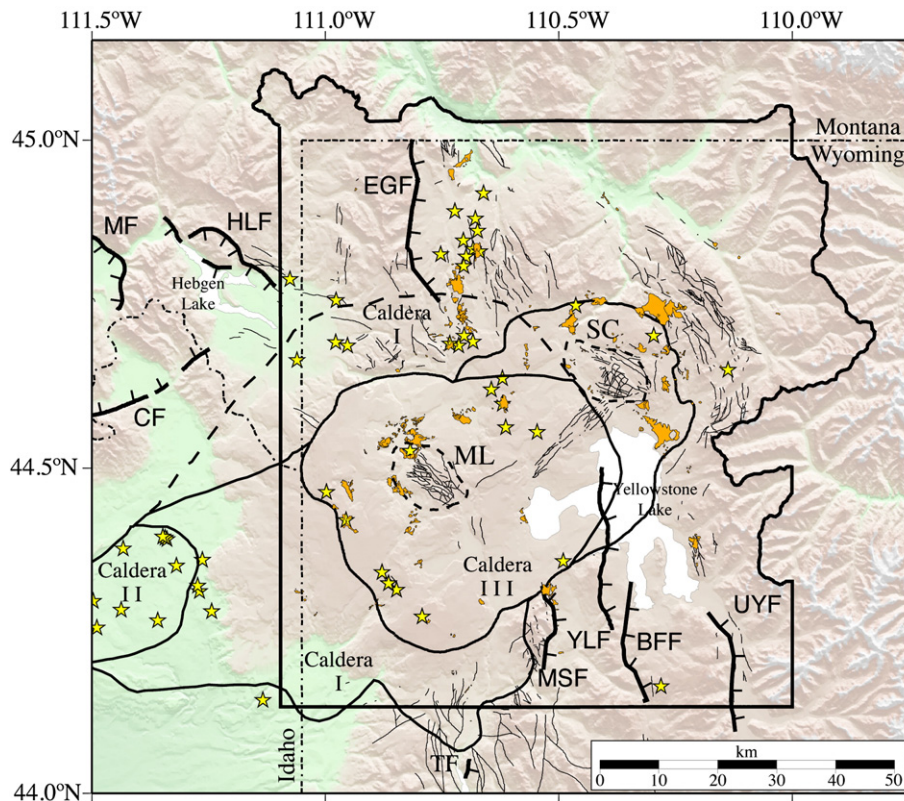


Fig. 5. Volcanic and tectonic features of Yellowstone and surrounding area. Yellowstone calderas I (2.05 Ma), II (1.3 Ma) and III (0.64 Ma) are shown as black lines and labeled. The two resurgent domes Mallard Lake (ML) and Sour Creek (SC) are shown with dashed black lines. Yellow stars mark post-caldera volcanic vents of 640,000 to 70,000 years in age (Christiansen, 2001). Late Quaternary faults are heavy black lines with ticks on downthrown side. Fault abbreviations are EGF = eastern Gallatin fault, HLF = Hebgen Lake fault, MF = Madison fault, CF = Centennial fault, TF = Teton fault, MSF = Mount Sheridan fault, YLF = Yellowstone Lake fault, BFF = Buffalo Fork fault, UYF = Upper Yellowstone Valley fault. Areas of hydrothermal features, including geysers, fumaroles, and hot springs, are shown in orange (Christiansen, 2001).

oblique-slip faulting and lithospheric extension. This extensional regime is considered to be driven by the gravitational collapse of a thickened lithosphere in response to cessation of subduction at the southwest plate margin and the development of the Pacific-North America transform boundary (Atwater and Stock, 1988; Jones et al., 1996; Sonder and Jones, 1999; Dickinson, 2004). The YSRP lithosphere is thus affected by a combination of regional tectonic extension and magmatic processes.

The Yellowstone hotspot has been the source of voluminous rhyolite tuffs and lavas with eruptions often having volumes of hundreds to thousands of cubic kilometers and representing some of the largest Quaternary eruptions on Earth (Christiansen, 1984, 2001; Mason et al., 2004; Morgan and McIntosh, 2005; Bonnicksen et al., 2008), with more than 140 giant silicic eruptions identified by the tephrochronology of ash-fall tuffs associated with the YSRP (Perkins and Nash, 2002). Three caldera-forming explosive eruptions at 2.05, 1.3, and 0.64 Ma formed the currently active Yellowstone Plateau volcanic field (Boyd, 1961; Christiansen, 2001; Christiansen et al., 2007) (Figs. 2, 5). More than 50 post-caldera rhyolite flows have since covered the Yellowstone Plateau, with the youngest at 70,000 ka in the southwest caldera (Christiansen, 2001; Christiansen et al., 2007).

The sub-crustal heat source fueling Yellowstone's extensive volcanism is also responsible for producing the high heat flow of the YSRP that stands out regionally amongst the thermal provinces of North America (Brott et al., 1981; Blackwell, 1989; Blackwell et al., 2006). The averaged regional heat flux of the Snake River Plain is

~150 mWm⁻², about 30% higher than the Basin-Range to the south and three times higher than the background flux of the Rocky Mountains to the east (Fig. 6). But the extraordinarily high heat flow of ~2,000 mWm⁻² of the Yellowstone Plateau is more than 30–40 times the average heat flow of continents (Fournier, 1989; Blackwell and Richards, 2004). About 25% of the total flux is thought to be due to conductive heat transfer from crustal magma sources (to be discussed later and in DeNosaquo et al., 2009–this volume) that in turn is fed by magmas from the Yellowstone mantle plume. Throughout Yellowstone, heat flow is variable because it is highly affected by shallow convective hydrothermal fluid flow and shallow magma migration (Fournier, 1989) (see DeNosaquo et al., 2009–this volume, for a discussion of densities and the influence of heat flow of the YSRP).

Compared to the Columbia River and contemporaneous Steens Basalts of Oregon, the Yellowstone-Snake River olivine tholeiitic basalts and high-alumina olivine tholeiitic basalts of the High Lava Plains have: (1) a major contribution from depleted (MORB-like) mantle (Hart and Carlson, 1987; Carlson and Hart, 1988); and (2) a sub-continental lithospheric mantle component (Leeman, 1982; Hart and Carlson, 1987). In addition, a primitive mantle component commonly associated with the lower mantle is evidenced by elevated ³He/⁴He values of hydrothermal waters and radiogenic isotope signatures of Yellowstone basalts (Craig et al., 1978; Doe et al., 1982; Leeman, 1982; Kennedy et al., 1985; Graham et al., 2009–this volume; Leeman et al., 2009–this volume). These petrologic and geochemical data thus suggest a sub-crustal magmatic origin with contributions

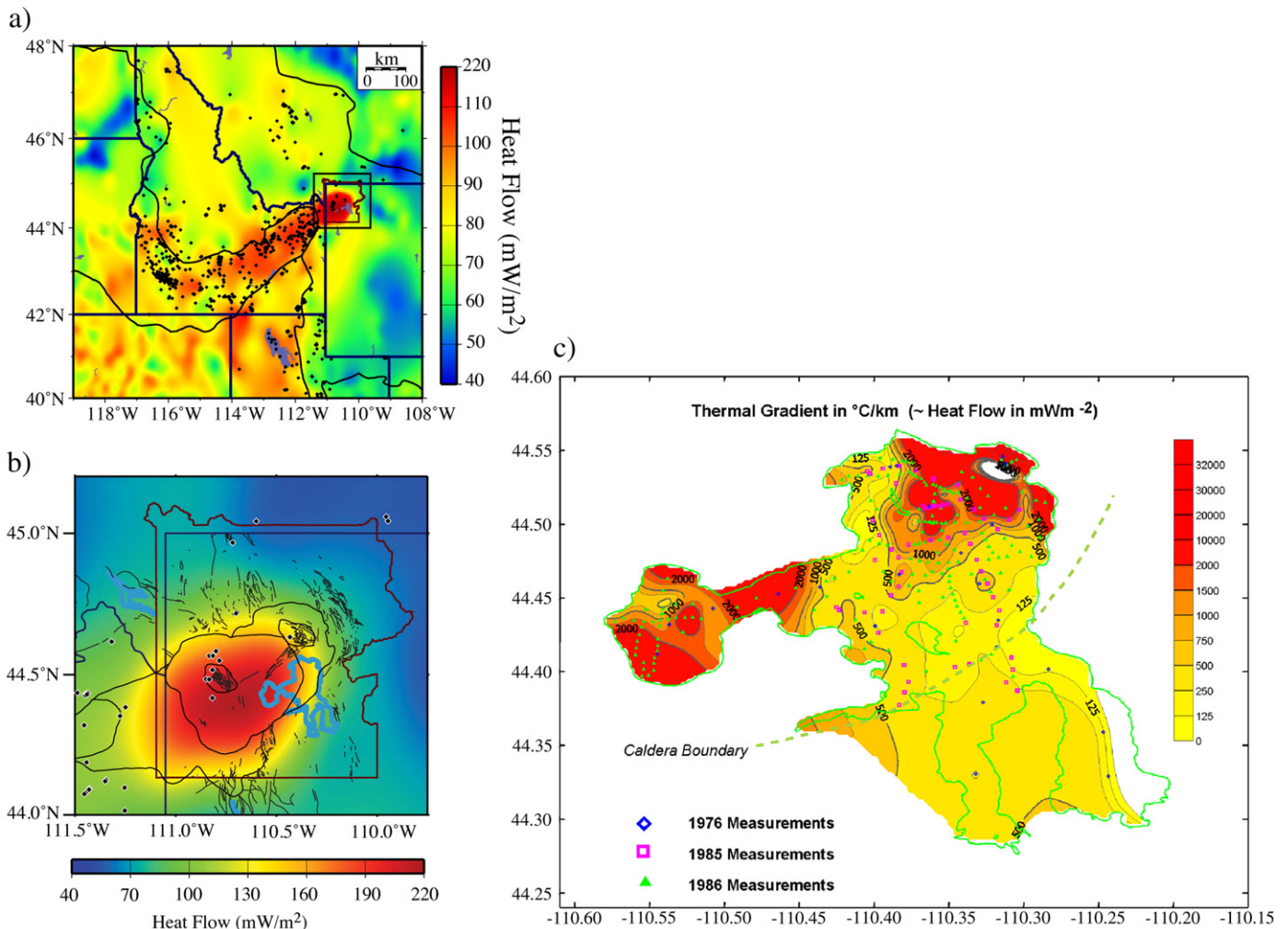


Fig. 6. (a) Heatflow of the Yellowstone and the Snake River Plain, with heatflow of the ESRP averaging ~150 mWm⁻²; (b) The scale show heat flow of ~200 mWm⁻²; and (c) very high heatflow of Yellowstone Lake ranges from ~100 mWm⁻² to extraordinarily high 30,000 mWm⁻² (after Blackwell and Richards, 2004).

from the mantle, a depleted asthenosphere, and old continental lithosphere, and importantly require unusually high-temperature melt.

The relationship of the Yellowstone hotspot volcanic rocks to the voluminous LIP (Large Igneous Province) Columbia River 17-Ma basalt volcanism is problematic. While flood basalts are commonly associated with the onset of hotspot activity, the Columbia River basalts are less voluminous than most flood basalt provinces. They are located north of the commonly projected trace of the Yellowstone hotspot, and are only the most active part of a long, narrow zone of nearly simultaneously active basaltic fissures that extend south into central Nevada (Fig. 2) (Zoback and Thompson, 1978; Armstrong, 1978; Pierce and Morgan, 1990, 1992; Camp, 1995; Glen and Ponce, 2002).

2.1. Yellowstone seismicity

The Yellowstone region is one of the most seismically active areas of the western U.S. It occupies the central part of the Intermountain Seismic Belt (ISB) (Smith and Sbar, 1974; Smith and Arabasz, 1991) that separates the active tectonism of the western U.S. from the stable part of the North America plate. Seismicity associated with the YSRP is associated with the parabola-shaped pattern of earthquakes surrounding the ESRP: a tectonic parabola that includes high topography and active faulting (Anders et al., 1989; Anders and Sleep, 1992; Smith and Braile, 1993, 1994). The ESRP is seismically quiescent at the M3+ level and lacks faulting but has notable Late Quaternary basaltic dikes of similar orientation to regional faults (Fig. 2) (Smith and Sbar, 1974; Rodgers et al., 1990; Kuntz et al., 1992; Smith et al., 1996; Parsons et al., 1998).

The Yellowstone seismic network from which we have obtained data for this study spans the entire Yellowstone Plateau (Fig. 7). It has recorded more than 30,000 earthquakes between 1973 and 2008

(Fig. 8), most of which had magnitudes less than 4 (Waite and Smith, 2004).

The largest historic earthquake in the western U.S. interior, the deadly August 1959 $M_{\text{s}}7.5$ Hebgen Lake, Montana, earthquake, occurred 25 km northwest of the Yellowstone caldera (Myers and Hamilton, 1964; Smith and Sbar, 1974; Doser, 1985) (Fig. 8). The Hebgen Lake earthquake broke along a pair of west-trending normal faults totaling 40 km in length with up to 5.7 m of slip and resulted in the deaths of 28 people. In contrast, the Yellowstone caldera is characterized by frequent but smaller earthquakes, most often occurring in swarms (Farrell et al., 2009-this volume). The $M_{\text{t}}6.1$ Norris Junction earthquake in 1975 (Pitt et al., 1979) was also the largest recorded event to occur within the Yellowstone caldera (Fig. 8).

The precisely relocated earthquakes for events between 1972 and 2007 (Husen and Smith, 2004; Farrell et al., 2009-this volume) and re-calculated magnitudes for events between 1984 and 2007 (Pechmann et al., 2007) permit a detailed evaluation of the historic seismicity. The most intense seismicity occurs between the Hebgen Lake fault and the northern rim of the Yellowstone caldera (Fig. 8). It is important to note that the cumulative seismic moment release in this region is an order of magnitude higher than inside the Yellowstone caldera (Puskas et al., 2007), implying the dominance of aseismic mechanisms for the caldera.

Epicenters in the northwestern part of Yellowstone form two bands: one extending in an E-W direction from Hebgen Lake to Norris Geyser Basin, the other extending in a general NW-SE direction from Hebgen Lake to the northern rim of the Yellowstone caldera (Fig. 8). The majority of earthquakes in this area occur between 5 and 10 km depth but focal depths >12 km are observed close to Hebgen Lake (Fig. 9).

Many of the earthquakes north of the caldera were associated with identified earthquake swarms (Waite, 1999; Farrell et al., 2009-this

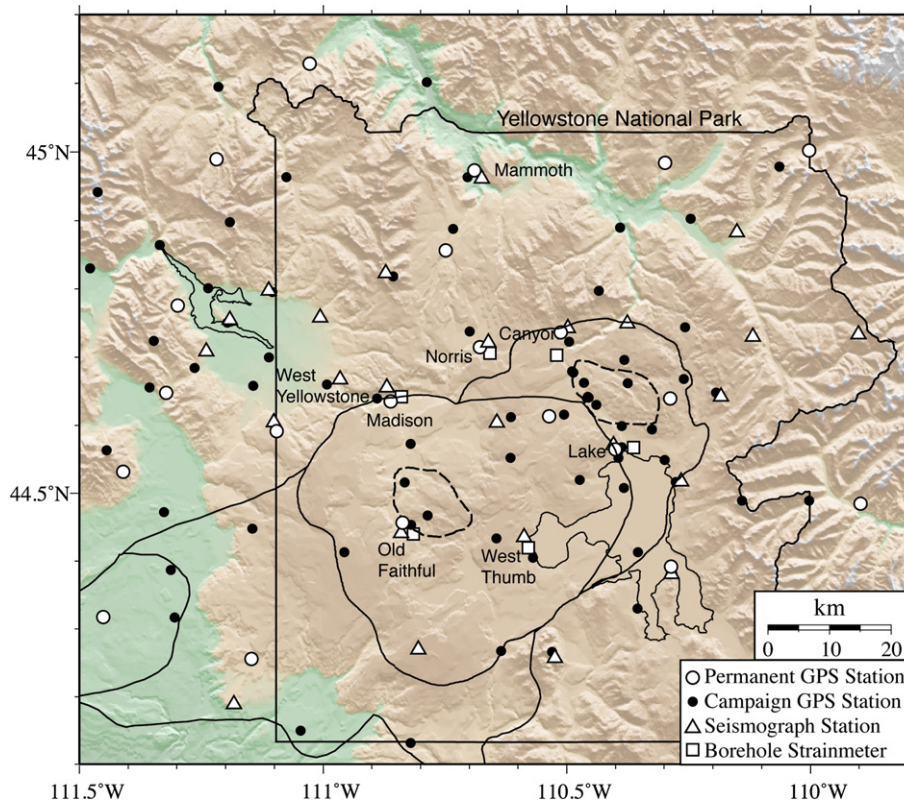


Fig. 7. Station map of Yellowstone National Park and surrounding area showing regional seismic, GPS, and borehole strainmeter networks. Seismic stations consist of broadband and short-period seismometers operated by the University of Utah and the Yellowstone Volcano Observatory. GPS sites include 26 permanent and 90 temporarily occupied (campaign) sites operated by the University of Utah and EarthScope PBO.

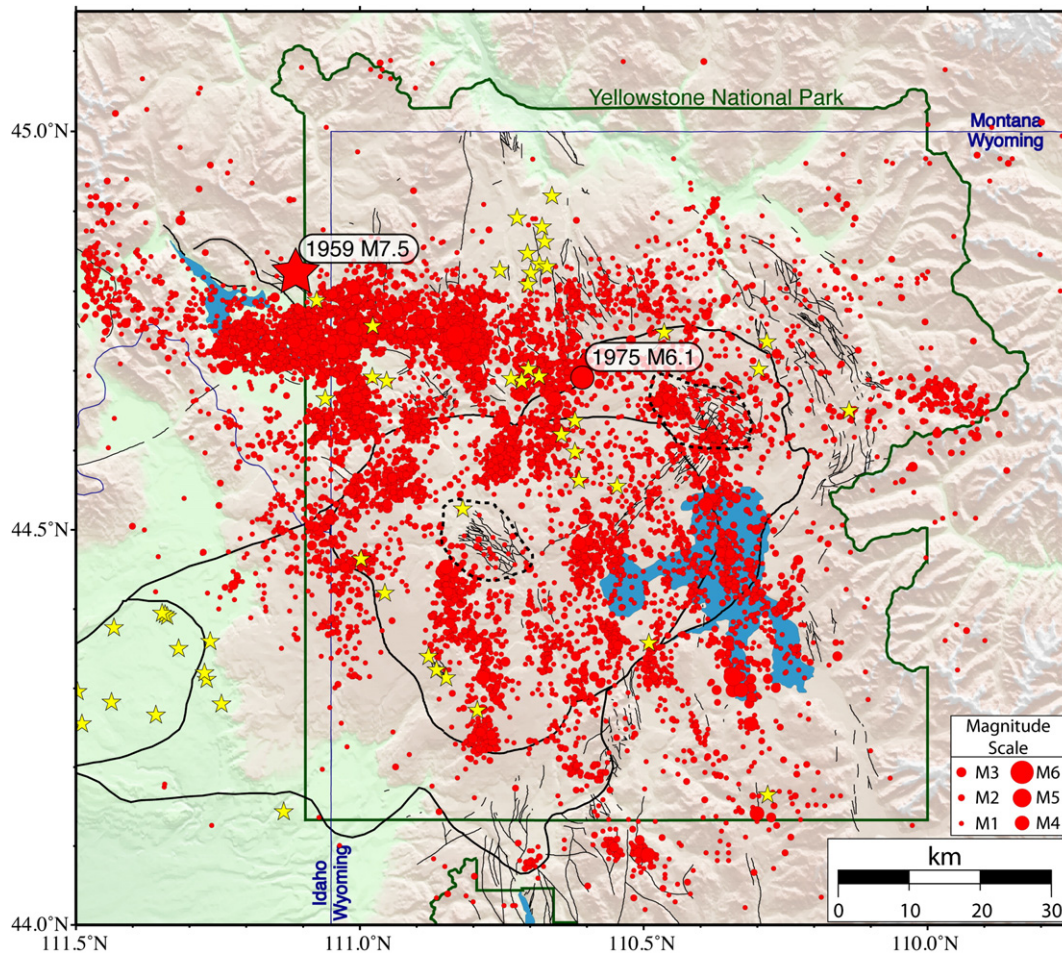


Fig. 8. Seismicity of the Yellowstone Plateau (1975–2007). Epicenters are located by employing a non-linear probabilistic earthquake location technique and a three-dimensional P-wave velocity model (Husen and Smith, 2004). Locations of the M7.5 1959 Hebgen Lake Mt and the 1975 M6.1 Norris Jct earthquakes are highlighted by a red star and large circle, respectively. Yellow stars denote the locations of post-caldera, <640,000-year-old -volcanic vents (Christiansen, 2001).

volume). The largest historic swarm in Yellowstone began in October 1985 in the area northwest of the Yellowstone caldera (Waite and Smith, 2002) (see discussion in section 3.4).

Earthquakes in the Yellowstone region generally correlate with the Late Quaternary faults such as the Hebgen, Madison, and Gallatin faults (Smith and Arabasz, 1991; Miller and Smith, 1999). Some of the faults have been mapped and dated (Figs. 5 and 8), but many seismogenic structures may have been buried by the post-caldera rhyolite flows yet still act as zones of weakness (Christiansen, 2001).

Seismicity of the Yellowstone caldera is characterized by shallow hypocenters with identified time-space clusters of earthquakes (Fig. 9) (Farrell et al., 2009-this volume). The central part of the caldera has relatively low seismicity, and no distinct seismic patterns are associated with the Mallard Lake or the Sour Creek resurgent domes. The majority of hypocenters in the caldera are less than 5 km deep, with notable northwest-southeast-trending zones that parallel the post-caldera volcanic vents (Fig. 5) (Husen and Smith, 2004). Some of the intra-caldera earthquakes are associated with hydrothermal areas such as Upper and Lower Geyser Basins, West Thumb Geyser Basin, the central part of the Yellowstone Lake, and the Mud Volcano area (Fig. 8).

2.2. Effects of high temperature on earthquake focal depths

Lateral variations of Yellowstone caldera focal depths reflect variations in the depth to the brittle-ductile transition (after Smith

and Bruhn, 1984). In Fig. 9, we show the 80th percentile maximum depth of earthquakes as the brittle-ductile isosurface of constant temperature. Assuming the brittle-ductile transition temperature of 400–500 °C for extensional tectonic regimes allows estimates of the conductive temperature gradient.

This distinctive shallowing of the seismogenic layer beneath the caldera is attributed to high temperatures that reduce the strength of the rock, transforming it from brittle to ductile behavior above a shallow high-temperature source, namely a crustal magma reservoir (Smith, 1978). Within the caldera, the crust appears to behave in a quasi-plastic manner at depths exceeding 4–5 km at temperatures greater than 350 °C to 450 °C as determined from petrological constraints (DeNosaquo et al., 2009). Such high-temperature rocks are incapable of sustaining shear stresses on faults (Smith and Bruhn, 1984). The maximum focal depths of ~15 km occur about 10 km from the west side of the caldera and correspond to a conductive thermal gradient of ~26 °C/km. Inside the caldera, the average 80th percentile depth is 4 to 6 km and corresponds to a gradient of 110 °C/km to 65 °C/km. These values are considered a proxy for the conductive component of heat flow and would correspond to heat flow values of ~250 mWm⁻², while a corresponding convective heat flow of ~1750 mWm⁻² would be required to produce the total observed heat flow of ~2000 mWm⁻².

The relative magnitude of thermal convective heat transport is specified by the Nusselt number, defined as the ratio of the convective to conductive heat flow. For Yellowstone, the Nusselt number of

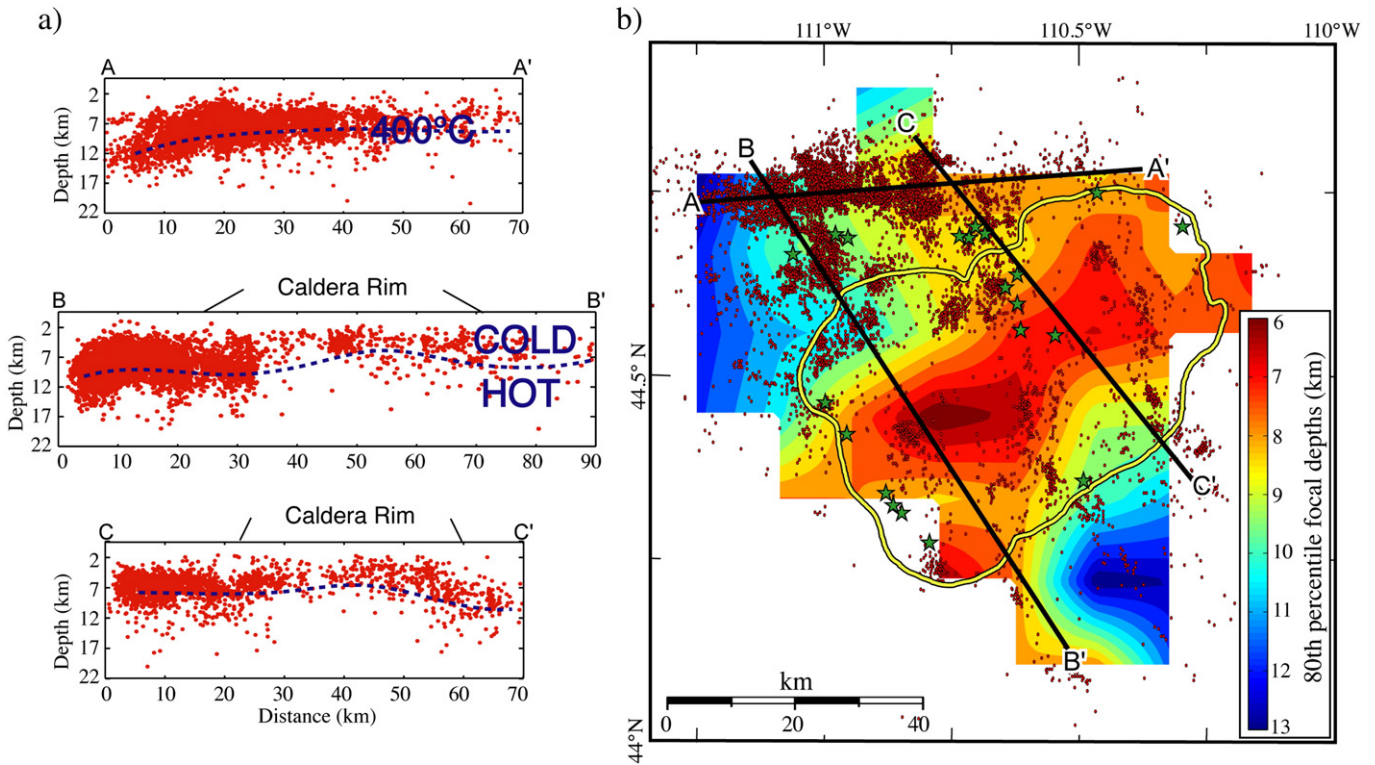


Fig. 9. Maximum focal depths of the Hebgen Lake–Yellowstone area serve as a proxy for temperature at the brittle–ductile transition: (a) well-located hypocenters (red dots) along 10-km-wide windows corresponding to profiles in map view (b). The 80th percentile maximum focal depth is marked by the dashed line. This depth is interpreted at ~400 °C. (b) Contoured map of the 80th percentile focal depths showing the very shallow focal depths in the caldera produced by high temperatures.

8 compares with the Nusselt number calculated for the Long Valley caldera, California, of 6 to 8 (Hill, 1992) and demonstrates the high thermal energy of this active hydrothermal system.

2.3. Crustal structure

The initial studies of Yellowstone crustal structure included earthquake and Curie depth determinations that revealed a shallow crustal heat source and focal mechanisms consistent with general crustal extension of the Yellowstone Plateau (Smith et al., 1974, 1977).

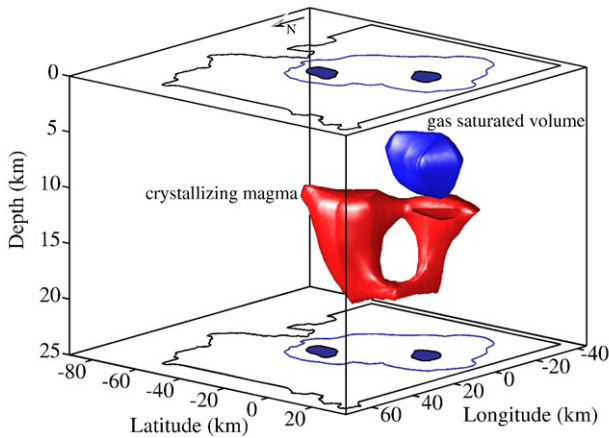


Fig. 10. Isosurfaces of anomalously low (-1.8%) P-wave velocity bodies are determined from local earthquake tomography of the Yellowstone caldera that reveals the Yellowstone magma reservoir. The shallow anomaly plotted in blue is interpreted to be a gas-saturated body. The red anomaly is interpreted to be 5% to 15% partial melt corresponding to a crystallizing magma body that feeds the surface silicic and basaltic magmatism of Yellowstone (from Husen and Smith, 2004). The outline of Yellowstone National Park (black), the Yellowstone caldera (blue), and resurgent domes (dark blue shaded regions) are projected at the top and bottom of the plot.

Controlled source seismic studies (Smith et al., 1982; Schilly et al., 1982; Lehman et al., 1982) revealed but could not discern the shape or depth of low velocity upper crustal source. These studies revealed a relatively homogenous lower crust to 40 km deep that was similar to that of the surrounding lithosphere not affected by lower crustal magmatism.

The three-dimensional (3D) P-wave velocity and P- to S-wave velocity ratio structure of Yellowstone has been determined using local-earthquake body-wave tomography from data of the Yellowstone seismic network by Miller and Smith (1999) and Husen et al. (2004) to confirm the existence of a low- V_p body at depths from ~8 km to the maximum depth of resolution of ~16 km (Fig. 10). The body is interpreted as hot, crystallizing magma beneath the Yellowstone caldera, i.e., Yellowstone’s main magma reservoir.

The low-velocity body, directly beneath the Yellowstone caldera, suggests that it is the source of Yellowstone’s volcanism. Its apparent upward U-shape, with the shallowest part of the velocity beneath the two resurgent domes, may be in part due to the lack of resolution between the shallowest bodies, or it may reflect shallow magma conduits that feed the resurgent domes. For a maximum V_p reduction of ~6%, the corresponding melt fraction is up to 15%.

This seismic image of the magma reservoir is consistent with a geochemical model by Lowenstern and Hurwitz (2008) that suggests magma rises closest to the surface (5–7 km depth) beneath the resurgent domes. Their model, based on CO₂ flux and heat flow, requires continued intrusion of plume-derived basalt to sustain the silicic, upper-crustal magmatic system responsible for Yellowstone’s youthful volcanism.

2.4. Contemporary stress field

The contemporary stress field that drives Yellowstone deformation is determined from geological and geophysical studies of the region (Zoback and Zoback, 1991; Nabelek and Xia, 1995; Smith et al., 1996; Haller et al., 2002; Waite, 2004; Puskas et al., 2007). Fig. 11

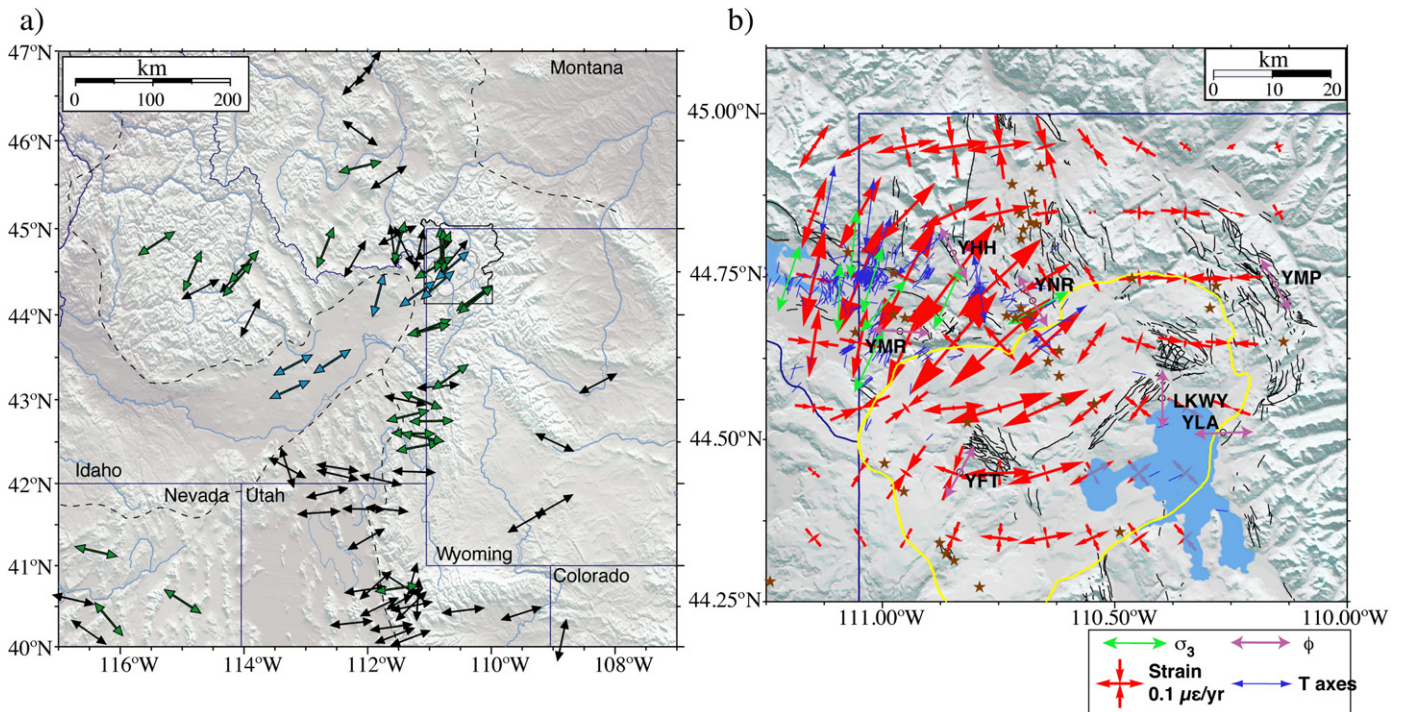


Fig. 11. Stress field of Yellowstone and the eastern Snake River Plain illustrating dominant lithospheric NE-SW extension (Waite and Smith, 2004): (a) arrows are directions of stress in the YSRP determined from focal mechanism T axes, maximum tensional stresses (σ_3), slip directions of normal faults (ϕ), post-caldera volcanic vent alignments, and GPS-derived strain tensors; and (b) similar stress direction axis direction of the Yellowstone Plateau.

shows a summary of horizontal extensional strain and tensional stress directions. For simplicity, we will assume that the minimum principal stress directions and focal mechanism T-axes are the directions of maximum lithospheric extension.

Crustal extension dominates the regional deformation pattern. Extension directions are generally NNE-SSW immediately south of Yellowstone (White et al., 2009–this volume) and E-W from the Teton Range south into southeastern Idaho. North and west of Yellowstone, extension is dominantly NE-SW except in the vicinity of the 1959 Hebgen Lake earthquake where it is N-S or NNE-SSW.

A clear rotation in extension direction across the Yellowstone Plateau is evident from the focal mechanism data. T-axes and minimum principal stress directions from focal mechanism inversion are generally N-S, west of Yellowstone, but rotate to NNE-SSW north of the Yellowstone caldera and then abruptly rotate to NE-SW at Norris (Waite and Smith, 2004).

We also note that NW-SE alignments of post-caldera volcanic vents within the caldera likely represent zones of weakness related to structures predating the 2.05 Ma Yellowstone volcanic system (Ruppel, 1972; Christiansen, 2001; Waite and Smith, 2004). The north to northwest vent alignments appear to link normal faults south of the caldera with normal faults to the north. For example, the Gallatin fault and the Red Mountain fault zone may be linked by the NW-SE trending alignment of vents that extend through the central caldera.

3. Crustal deformation of the Yellowstone Plateau

3.1. Geodetic measurements and intraplate kinematics

Earliest ground motion measurements in Yellowstone were from precise vertical leveling of benchmarks established in 1923 in conjunction with road construction. The benchmarks were re-surveyed in 1975–76–77 by Pelton and Smith (1982), who discovered the unprecedented uplift of the Yellowstone caldera by up to 75 cm (Pelton and Smith, 1982; Dzurisin and Yamashita, 1987). These

observations lead to the establishment of 15 permanent GPS stations that were installed in Yellowstone, the ESRP, and surrounding areas for the Yellowstone Geodynamics project beginning in 1996. In addition, GPS data from ~160 campaign stations (supported by UNAVCO) were acquired in seven surveys (1987, 1989, 1991, 1993, 1997, 2000, and 2003) (Fig. 12), (see Puskas et al., 2007, for details of these field projects).

GPS velocities were determined by calculating changes in station coordinates over time to determine station velocities. Velocities were constrained to a North America fixed reference frame (Bennett et al., 2001). In this reference frame, it is assumed that there is no deformation in the stable U.S. continental interior east of the Rocky Mountains. Our calculated velocities are with respect to the continental interior, also called stable North America.

The GPS derived velocity data were partitioned into multiple time windows to document temporal changes: 1987–1995, 1995–2000, 2000–2003, and 2004–2007. The ground velocities for the first three time periods revealed notable deformation changes in horizontal and vertical components (Fig. 12), with alternating subsidence and uplift of the Yellowstone caldera at up to 2 cm/yr, uplift northwest of the caldera, and regional extension of 2 to 4 mm/yr across the Hebgen Lake fault zone (Wicks et al., 1998; Puskas et al., 2007). During the observing periods, stations southwest of the caldera and outside the aforementioned regions moved southwest, indicating regional extension with respect to stable North America (Fig. 12). Beginning in mid-2004, GPS and InSAR (Interferometric Synthetic Aperture Radar) measurements recorded an unexpected episode of caldera ground uplift at very high rates of up to 7 cm/yr, i.e., three times greater than previously observed deformation episodes (Wicks et al., 2006; Chang et al., 2007) (Fig. 13, see also supplemental section).

On a regional scale, the eastern Snake River Plain adjacent to Yellowstone moved southwest at 2.4 ± 0.4 mm/yr from 1995 to 2000 (Puskas et al., 2007). The southwest motion of the ESRP contrasts with the westward extension of the eastern Basin and Range and is part of a larger pattern of clockwise rotation in the direction of deformation of the western U. S. (Puskas and Smith, 2009). Puskas and Smith (2009)

hypothesized that the southwest motion of the ESRP was driven by the gravitational potential gradient associated with the hotspot swell.

3.2. Magmatic sources of deformation

Volumetric strain modeling was employed to determine the configuration and depths of source bodies responsible for deformation of the Yellowstone caldera (see Vasco et al., 1988, 1990 for details of methodology). Surface motions, measured by leveling surveys

between 1987 and 1993 and InSAR between 1992 and 2002, were combined with the GPS data for 1987–2003 to constrain the source modeling.

For 1992–1995, the modeled volumetric decrease occurred along the caldera axis, between the two resurgent domes at 6 to 10 km depth (Vasco et al., 2007). The deflation rate during this interval was $8.7 \times 10^{-3} \text{ km}^3/\text{yr}$. For 1996–2000, caldera uplift was modeled by volume increase below the northwest caldera boundary at 6 to 10 km depth of $4.6 \times 10^{-3} \text{ km}^3/\text{yr}$. Additional models from 2000–2001 and

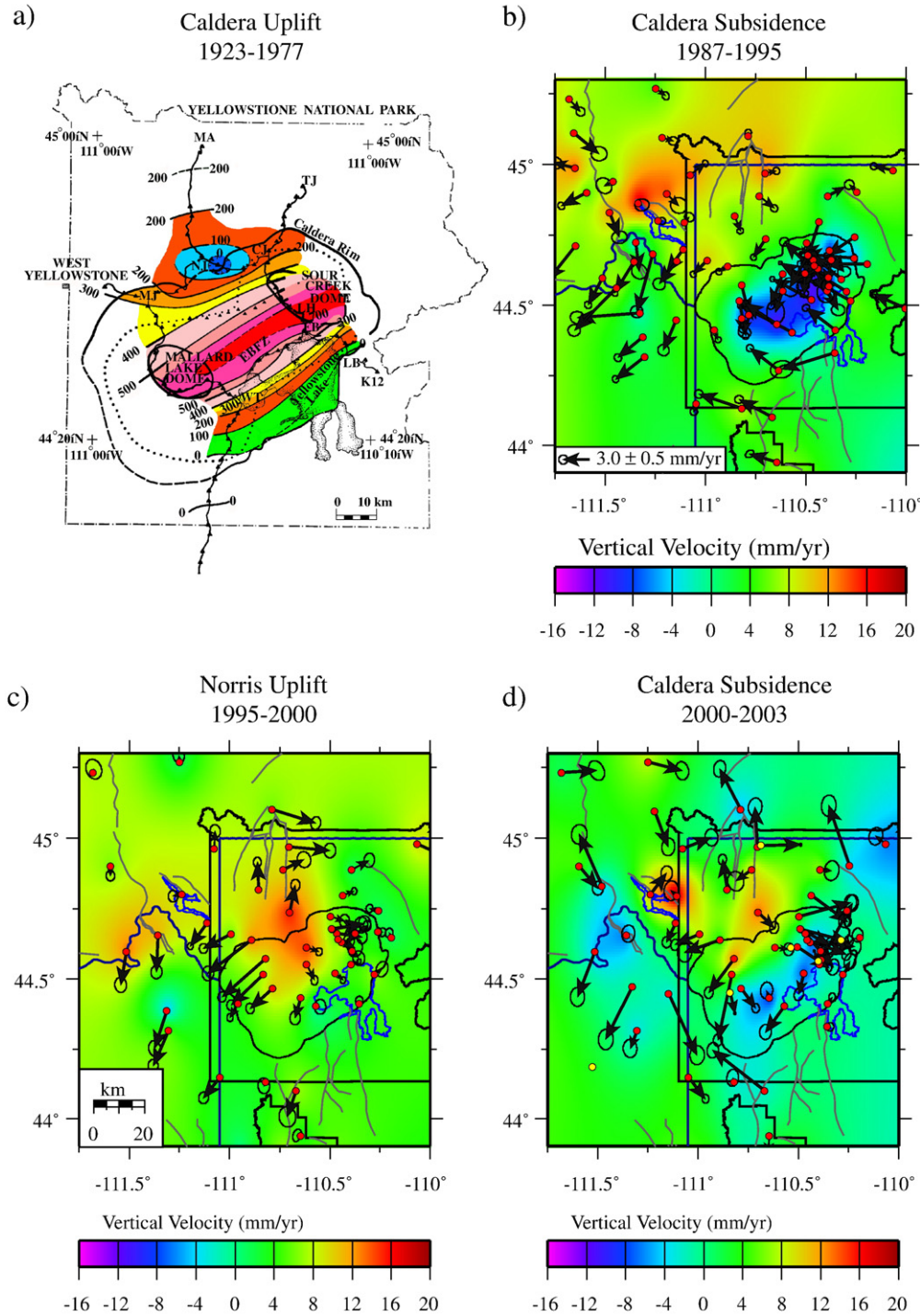


Fig. 12. Crustal deformation of the Yellowstone Plateau from precise leveling and GPS observations (after Pelton and Smith, 1982; Puskas et al., 2007; Vasco et al., 2007). Color backgrounds represent vertical motion (mm) measured from (a) leveling surveys between 1923 and 1987 (mm) and (b)–(d) GPS campaigns between 1987 and 2003. Red circles represent campaign GPS sites, yellow circles represent permanent GPS stations, and arrows are the direction of motion relative to stable North America. Time windows correspond to the distinct periods of caldera uplift and subsidence.

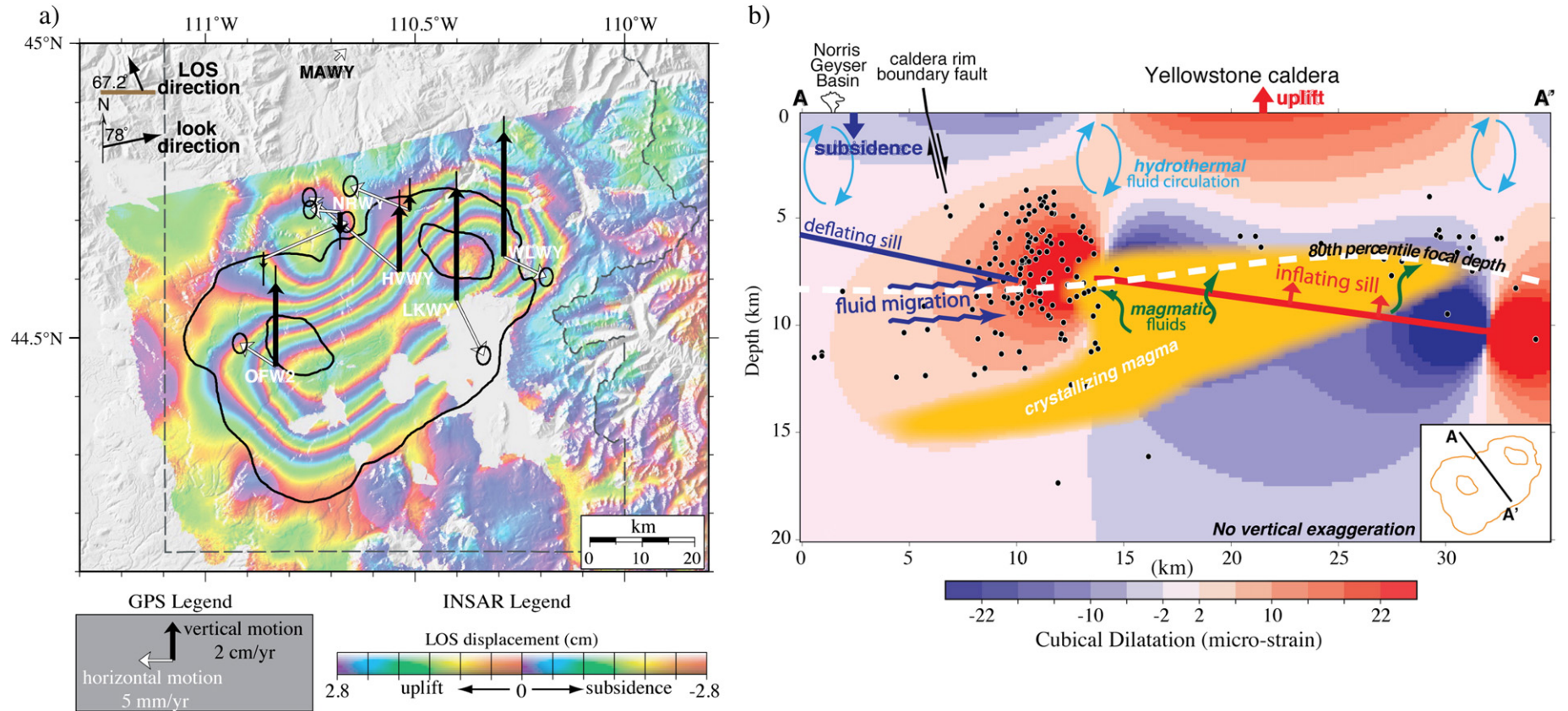


Fig. 13. Accelerated uplift of the Yellowstone caldera revealed by GPS and InSAR data (2004–2007) modified from Chang et al. (2007). (a) Map view of the uplift with GPS vertical and horizontal vectors and background showing line of sight (nearly vertical) deformation in 28 mm displacement bands. Note the maximum 7 cm/yr of uplift of the caldera compared to up to 1.5 cm/yr of subsidence of the Norris Geyser basin area. (b) Cross section of modeled 10° SE-dipping sill that is interpreted to be inflating at 0.1 km³ per year, consistent with the modeled rate of inflation from the heat flow and geochemical data. Color contours are Coulomb stress increase (red) or decrease (blue) caused by inflation of the sill. Hypocenters of earthquakes that occurred during the period of accelerated uplift are shown as black dots.

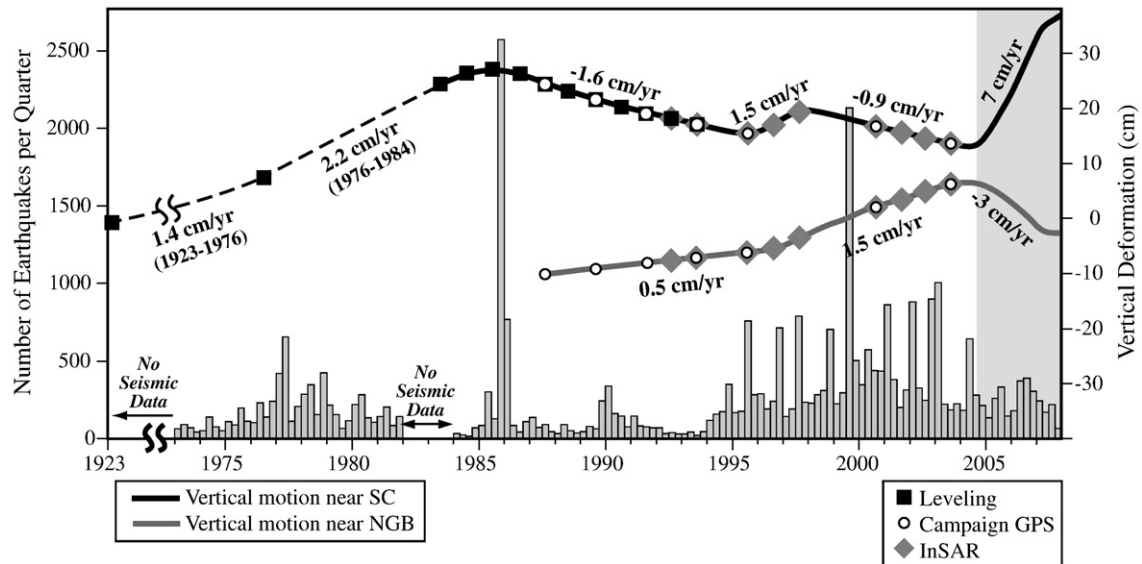


Fig. 14. Temporal history of deformation and earthquakes of Yellowstone. Earthquakes are sorted into three-month periods. Specific leveling and GPS surveys are shown as black squares and white circles, respectively (from Chang et al., 2007). Abbreviations are: SC = Sour Creek resurgent domes, and NGB = Norris Geyser Basin.

2001–2002 employed InSAR data to image a volumetric decrease along the Yellowstone caldera axis at depths of 6–8 km with uplift along the north caldera boundary at 4 to 6 km deep for 2000–2001 and 2–4 km deep for 2001–2002. Importantly, the deeper parts of the volumetric source volumes overlap with the top of the seismically imaged magma reservoir (Husen et al., 2004). This argues that the subsidence source originated within the upper part of the magma reservoir.

Similarly, source modeling of the 2004–2007 accelerated uplift (Chang et al., 2007) suggests a near-horizontal expanding magma body over an area $40 \times 60 \text{ km}^2$ at 9 km beneath the caldera, again (Fig. S1) located near the top of the seismically imaged crustal magma chamber (Fig. 13). The estimated rate of volumetric expansion of $\sim 0.1 \text{ km}^3/\text{yr}$ for this uplift episode is similar to the magma intrusion rate required to supply the very high heat flow of $\sim 2000 \text{ mW/m}^2$ of Yellowstone (Fournier, 1989). These are the first observations of caldera-wide magma recharge of the Yellowstone volcanic system.

3.3. Temporal correlation of earthquakes and deformation

The temporal correlation of Yellowstone earthquake occurrence with decadal episodes of uplift and subsidence from 1973 to 2006 is shown in Fig. 14. The change from uplift to subsidence in 1984–1985 notably coincided with Yellowstone's largest earthquake swarm in fall 1985 (Fig. 14), prompting an examination of the causative relationships between seismicity and deformation.

Waite and Smith (2002) first interpreted the seismicity migration rate and stress directions determined from nearly identical focal mechanisms to argue that the focused seismicity of the 1985 earthquake swarm was related to magmatic or hydrothermal fluid flow that originated from beneath the Mallard Lake resurgent dome. Fluid was transported to the northwest, inducing earthquakes once it reached the shallow brittle crust. The volume loss resulting as fluids escaped could be responsible for the change in caldera surface deformation from uplift to subsidence (Dzurisin et al., 1994). Conversely, uplift would be produced by fluids trapped beneath a barrier such as the brittle-ductile transition zone (e.g., Fournier and Pitt, 1985; Dzurisin et al., 1994; Waite and Smith, 2002) or a stratigraphic boundary, leading to increased pore pressure and volumetric increase.

Following the 1985 caldera reversal, subsidence continued for a decade until 1995, when the caldera motion began a 5-year period of

minor uplift followed by renewed subsidence until the sudden change to accelerated caldera uplift. At the inception of the 1995 uplift, seismicity began to increase until the onset of accelerated uplift in late 2004 (Fig. 14). However, no other documented swarms showed the kind of migration of activity that the 1985 swarm did (Waite and Smith, 2004; Farrell et al., 2009–this volume).

These dynamic crustal processes lead to the natural question of how mantle features relate to and drive the crustal seismicity and deformation. The mantle structure and related geodynamics are the subjects of the next sections.

4. Mantle tomography

In this part of our discussion, we evaluate the traveltime delay data from teleseismic distant earthquakes that are used to provide new tomographic images of the Yellowstone hotspot upper mantle structure. The new mantle velocity models are derived from data acquired in the Yellowstone Geodynamics experiment. This consisted of 50 temporary stations and a 30-station telemetered array operated in two IRIS-PASSCAL-supported deployments, with additional data from 45 stations of the Yellowstone, Montana, and Utah regional seismic networks, a total of nearly 200 seismic stations. The seismic array was deployed in a 500 km by 600 km area centered on Yellowstone for a year, a distribution that was planned to acquire data that could resolve the velocity structure of the upper mantle (Figs. 4 and 7). Seismograph spacing for our experiment was from $\sim 15 \text{ km}$ to 35 km but was increased toward the edge of the array to $\sim 35 \text{ km}$.

Initial tomographic models from the 1999–2002 data revealed a 60° west-dipping low P-wave low-velocity body of conduit shape that was interpreted as a shallow upper mantle plume to depths of $\sim 450 \text{ km}$ (Waite, 2004; Waite et al., 2006; Yuan and Dueker, 2005). We also note that the analysis of surface wave data revealed anomalously low shear-wave velocities of the shallow YSRP structure at the top of the plume at depths of 200 km (Schutt et al., 2008).

In this paper we apply a new optimized tomographic inversion scheme (Jordan, 2003; Wüßner et al., 2006; Barth et al., 2007) to the same data to image the upper mantle beneath Yellowstone to depths of $\sim 700 \text{ km}$. The advantage of the new methodology is that the teleseismic P-wave delays are constrained by independent data such as the seismic structure of the mantle discontinuity (Fee and Dueker, 2004), the crustal structure of the Intermountain region (Lynch et al., 1997), the detailed

crustal structure of Yellowstone (Husen et al., 2004), and the 2003 GEOID data anomaly. The seismic tomography method and model parameterization is described in the supplemental section 1 and Fig. S6.

The teleseismic delay time data were taken from the earlier analysis of Waite et al. (2006) and included recordings of 152 earthquakes from the 84-station Yellowstone hotspot network. The seismic data were analyzed by direct interpretation and traveltimes picking (Waite et al., 2006), including assignment of uncertainties using the cross-correlation method of Van Decar and Crosson (1990). The delay time data were sorted into three resolution and quality classes (± 0.01 s, ± 0.03 s and ± 0.05 s). The level of uncertainties for these data was determined from the cross-correlation-analyzed traveltimes data with a sampling rate of 40 Hz. However, as the inversion method relies on the relative weighting of the data and not on the absolute values of the data errors, it is possible to utilize these uncertainties as weights. The knowledge of absolute values of the data errors was thus not necessary.

Problematic data were eliminated, resulting in a total of 4890 P-wave traveltimes residuals from the phases P, PKIKP, and PKiKP. P-wave traveltimes residuals were calculated by subtracting the theoretical traveltimes for each station location for the global one-dimensional P-wave velocity model, IASP91 (Kennett and Engdahl, 1991) from the observed traveltimes. We did not employ the S-wave data in our new calculations, but used the S-wave results of Waite et al. (2006).

A key objective in this study was data consistency, since the optimized parameterization can deal with the uneven ray distribution. To remove the effect of source mislocation and source structure, we corrected for the mean residual traveltimes from all stations for each event. This results in relative traveltimes residual data that show late arrivals of PKIKP and PKiKP phases associated with underlying low seismic velocities in three main regions: Yellowstone National Park, the ESRP, and the area NW of Yellowstone.

For the inverse modeling we employed the JI-3D optimized inversion scheme (Jordan, 2003), designed to provide stable and highly resolved models both in the mathematical and spatial sense. The inversion method is based on a Bayesian approach (Tarantola and Valette, 1982; Zeyen and Achauer, 1997) that allows including *a priori* information, e.g., crustal structure and 1st-order discontinuities, in the inversion via an *a priori* covariance matrix. This is especially important since these features can have a significant effect on the observed delay-time data but usually cannot be resolved by teleseismic tomography.

The forward calculations of ray paths, traveltimes, and Frechet derivatives are based on standard ray theory. The full three-dimensional ray tracing is performed iteratively using a simplex algorithm adapted from Steck and Prothero (1991). The chosen step length was 100 m and the cut-off for the simplex search 2×10^{-7} s. We use 15 harmonics with initial amplitudes of 1 km. These settings are clearly optimized to yield maximum accuracy at the expense of computation time. Though there is an ongoing debate about the validity of standard ray compared to “banana-doughnut” ray theory in tomographic problems, our reconstruction test modeling as well as other studies that employed the JI-3D method (e.g., Keyser et al., 2002; Jordan, 2003; van der Hilst and de Hoop, 2005; Barth et al., 2007) show that the use of standard ray tracing provides adequate and realistic results. To reduce non-uniqueness and to improve stability of the inversion problem we implemented a variable optimized parameterization scheme (Jordan, 2003) (see supplemental section 2 for details).

4.1. Upper mantle tomographic inversion and resolution

Due to the nonlinear nature of the problem, we performed an iterative inversion of the P-wave delay time data with up to four iterations. The *a priori* model variances and the damping parameters were determined by trial and error. We defined the optimum solution as a simple model that provides a large reduction of the data misfit.

Because of the stability of the method, a moderate change of the optimum damping merely changes the amplitudes but not the features of the model. Since the resolution depends on the ray distribution, which can change during the iterative inversion, we reexamined the resolution matrix to ensure that the model still provides optimum stability conditions, which implies that the diagonal elements of the resolution matrix still are “constant”. Further details on the inversion scheme and image resolution and reconstruction tests are in the supplemental section 3 and Figs. S2–S5.

Reconstruction tests consist of forward calculations of a model data set employing a synthesized earth structure model and utilizing the same source and receiver distribution as in the Yellowstone seismic experiment (Waite et al., 2006) (see supplemental section 3). Gaussian errors were added to the synthetic data with realistic standard deviations and the data are inverted in the same way as the real data. The inversion result shows how an anomaly at the position of the synthetic input structure can be recovered in terms of location and amplitude and also shows possible smearing along main ray directions. Details and results of the reconstruction tests are discussed in Section 4.3 and in the supplemental section 3.

4.2. Seismic images of the Yellowstone hotspot mantle

Our new P-wave tomographic images (Figs. 15–17) reveal a prominent upper-mantle, low-velocity body beneath Yellowstone and high-velocity features in the surrounding regions. The amplitudes of the velocity anomalies are obtained from the difference between the maximum velocity perturbation of an anomaly and the background level in the respective layer. A key feature of our calculations was the ability to resolve velocity structure to ~ 800 km.

We imaged a strong low-velocity body from ~ 30 to 250 km directly beneath the Yellowstone caldera and from 30 to 100 km beneath the eastern Snake River Plain with P-wave velocity reductions of 1.8%. A similar feature is described by Waite et al. (2006), who also found a -2.3% anomaly in their P-wave model and a -5.5% anomaly in their S-wave model.

A weaker and smaller-volume anomaly with more of a conduit shape and a P-wave velocity perturbation of $\sim -0.75\%$ is imaged from about 250 km depth beneath the caldera to 650 km depth at a position ~ 100 km WNW of the caldera and dipping 60° . This anomaly corresponds to -1% P-wave, and -2.5% S-wave anomalies (Waite et al., 2006). The combined low-velocity anomaly is interpreted as a plume of partial melt that extends upward from the bottom of the mantle transition zone at ~ 650 km and promotes small-scale convection in the uppermost 200 km of the mantle. We specifically note that there was no vertical velocity anomaly directly beneath Yellowstone deeper than 250 km.

In addition to the low-velocity plume structure described above, the inversion results show two additional blob-like low-velocity bodies along the conduit with P-wave velocity perturbations of $\sim -0.5\%$ in the transition zone in the layers labeled 428 km, 501 km, and 571 km in Fig. 15. These depths correspond to the respective nodal layers. These structures are also recognizable in the last two model layers, below the transition zone.

The reconstruction tests (supplemental section 3) confirm that the anomalies shown in the tomographic model can be resolved reliably both in the upper mantle and the mantle transition zone. There is no indication that the imaged plume is significantly affected by vertical smearing along the predominant ray direction. According to the reconstruction tests, the resolved amplitudes are relatively low. Combining the results from the reconstruction tests in the upper mantle, we estimate a minimum -3% P-wave velocity perturbation between 30 and 200 km depth and a minimum -1% P-wave velocity perturbation between 200 and 650 km depth. However, we recognize that the P-wave velocity perturbation within the layer at 30 km depth is probably larger in a small area

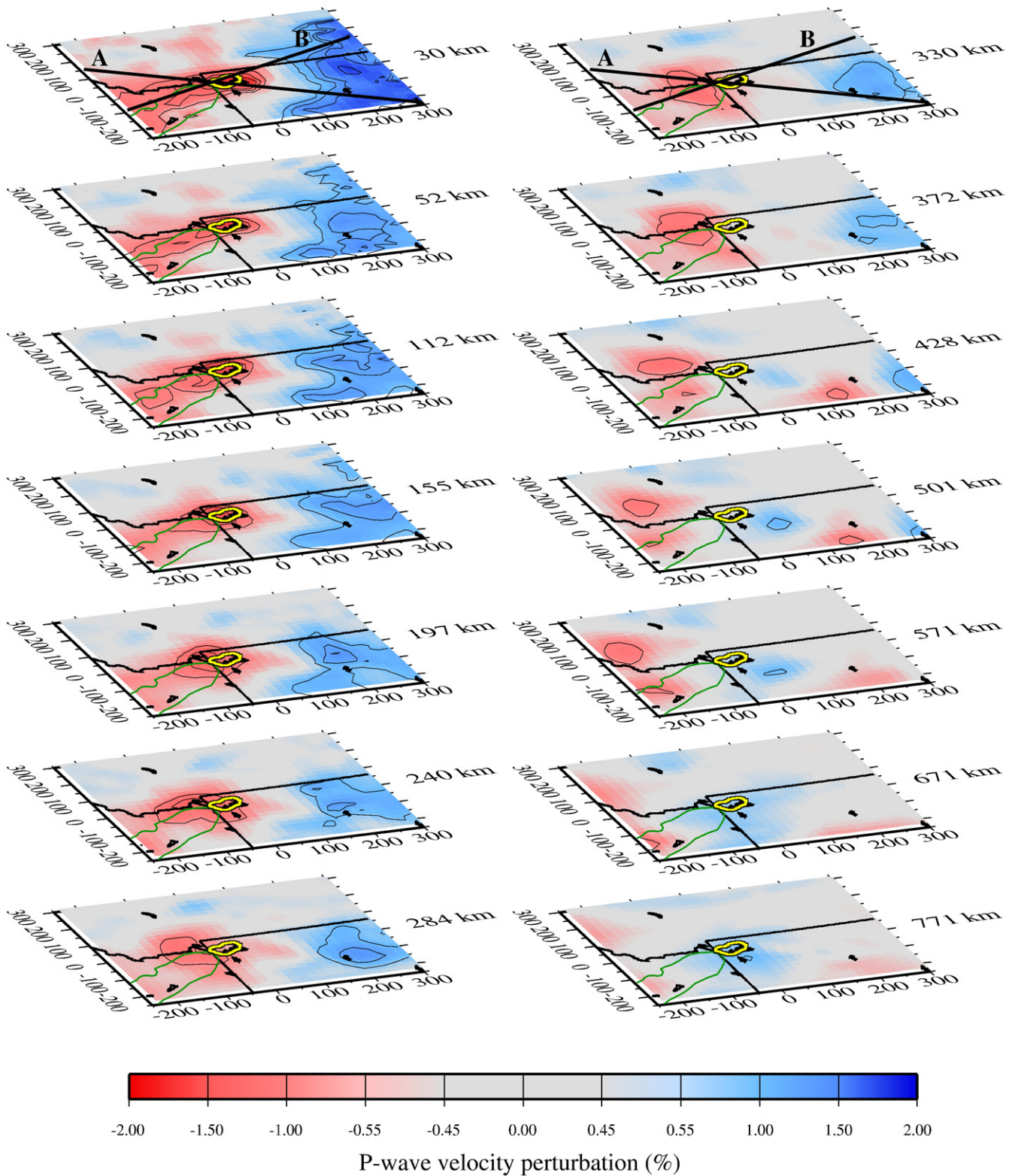


Fig. 15. P-wave velocity perturbation slices (% change from homogeneous background model) from tomographic inversion of teleseismic data for the Yellowstone hotspot (after Jordan et al., 2005; Waite et al., 2006). Data consisted of P-wave arrivals of 115 earthquakes recorded at 85 stations with 4890 P, PKiKP and PKiKP arrivals. Maps are horizontal slices of P-wave velocity in % at selected depths with corresponding relative decrease (red) and increase (blue) velocities. Contours indicate the $\pm 0.5\%$, $\pm 1.0\%$ and $\pm 1.5\%$ perturbations. Note the low-velocity anomaly beneath Yellowstone is displaced to the west as depth increases. A high-velocity zone is located to the east of Yellowstone. Profile lines for Fig. 16 are shown in the 30 km and 330 km depth slices.

beneath the Yellowstone caldera. These values are included in the schematic representation of the geodynamic plume model in Fig. 18.

Based on these reconstruction tests, the -0.5% isosurface in Figs. 17 and 18 can be considered to represent the $\sim -1.0\%$ P-wave perturbation level. We estimate the deviations of localized maximum

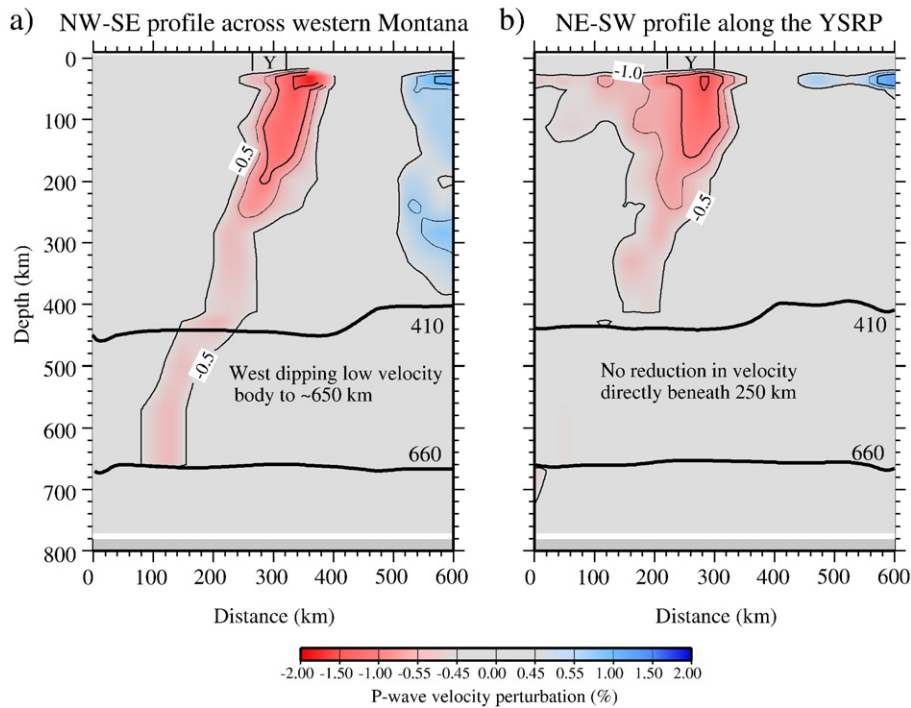


Fig. 16. Two-dimensional cross sections of the Yellowstone P-wave low-velocity anomalies corresponding to Fig. 15 (Jordan et al., 2005). (a) NW-SE cross-section across western Montana and western Wyoming, and (b) NE-SW profile along the YSRP. Significantly these profiles reveal a 60° west-dipping low-velocity anomaly of up to -2.5%. The anomaly extends to at least 660 km in the NW-SE profile, but does not extend deeper than 200 km beneath Yellowstone in the NE-SW profile. Isolines are the -0.5%, -0.75%, -1.0% and -1.5% P-wave velocity anomaly levels. The location of the Yellowstone Plateau is marked with a “Y”.

amplitudes of the real plume structure from the minimum model as smaller than 1%.

The reconstruction analyses also show that we are able to resolve anomalies below the transition zone with amplitudes of -1% if they are in a well-sampled area. This implies that there is likely no vertical continuation of the low-velocity body of greater than 1% below

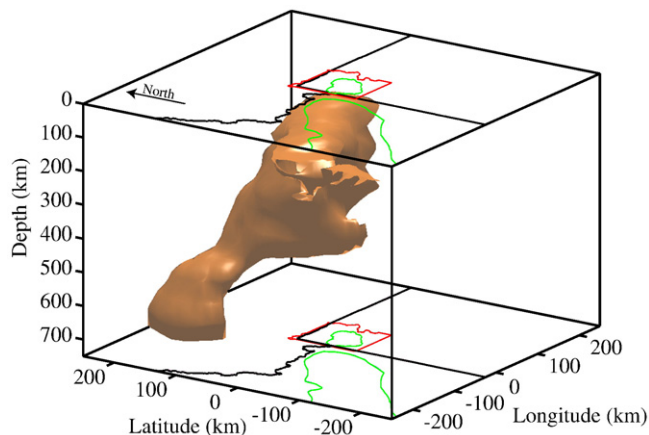


Fig. 17. Isosurface of P-wave seismic image of the Yellowstone plume as a 60° (from horizontal) west-dipping, rising column of molten rock of up to -1.5% melt originating in the mantle transition zone (after Waite et al., 2006). The plume is represented by a three-dimensional P-wave velocity isosurface encompassing the ~-0.5% values. This amplitude is considered the true amplitude, derived from the reconstruction tests. The top of this upper mantle plume only underlies Yellowstone vertically to depths of ~250 km, but the deeper part to the northwest is at a depth of ~650 km, at the bottom of the mantle transition zone. (Also see 3D animation of the University of Utah Yellowstone hotspot project results in the Electronic Supplement). At the top and bottom of the imaged section, state boundaries are represented as heavy black lines, Yellowstone National Park is represented by a red line, and the Yellowstone caldera and eastern Snake River Plain are outlined in green.

the transition zone. This deduction is supported by the absence of local uplift of the 660-km discontinuity boundary, and no obvious continuation of the plume-like structure into the lower mantle in global tomography models (Montelli et al., 2004; van der Hilst and de Hoop, 2005). However, a regional temperature increase below the transition zone, extending beyond the range of our model, would raise the 660-km discontinuity relatively evenly around Yellowstone. This would not be detectable using the relative traveltimes residuals from our data set.

We also note a prominent high-velocity anomaly, +1.2% V_P and +1.9% V_S , located at ~50 to 200 km depth southeast of Yellowstone and beneath the thicker lithosphere of the stable interior. This area is above a region of prominent Laramide contractional folds and thrusts and part of the Precambrian core of North America. Yuan and Dueker (2005) and Waite et al. (2006) described this structure as potentially the down-welling arm of mantle convection, but the large-scale mantle-convection models (Section 6) indicate near-horizontal return flow in an easterly direction, so this anomaly may reflect a remnant structure of the tectosphere.

Mantle structure on a broad scale is revealed by whole-mantle tomographic images. The P-wave models of Montelli et al. (2004) and van der Hilst and de Hoop (2005) that pass through Yellowstone clearly illustrate the location of Yellowstone with a west-dipping low-velocity (-1%) body extending to depths of <1000 km. New mantle images emerging from the EarthScope USArray data (Xue and Allen, 2007; Burdick et al., 2008; Sigloch et al., 2008; Xue and Allen, 2009) also reveal a west-dipping low-velocity body to depths of ~500 km. Xue and Allen (2009) noted discontinuous low velocity bodies that make up the plume image.

Our data reveal distinct “blobs” of rising melt of ~150 km in length. Importantly, the Xue and Allen (2009), Burdick et al. (2008), and Sigloch et al. (2008) USArray-derived seismic images reveal a discontinuous 0.5% to 1.2% low-velocity mid-mantle body to depths of up to 1000 km underlying most of the western U.S. including the Yellowstone plume. This pillow of low-velocity material may reflect

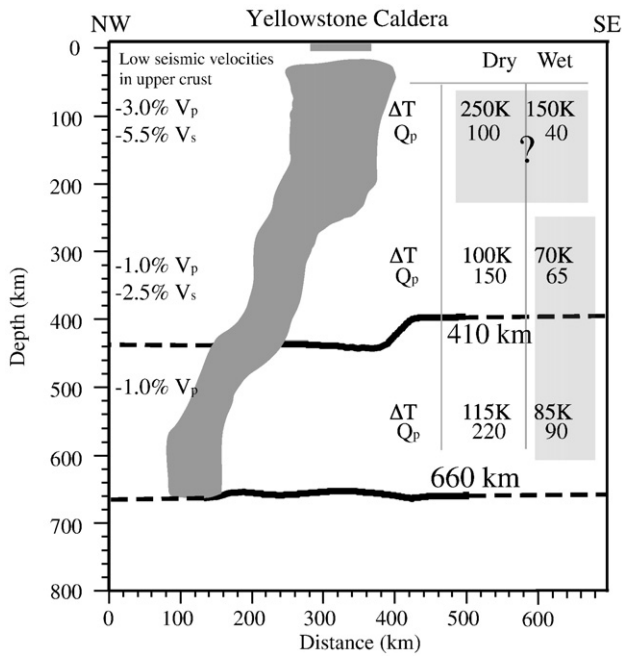


Fig. 18. Geodynamic model of the Yellowstone plume. Model of excess temperature (K) is constrained by seismic P-wave velocity and relative attenuation of P-waves (Q_p) in Q^{-1} , for wet and dry models of Cammarano et al. (2003) and Cammarano and Romanowicz (2007). Q_p is the relative attenuation of seismic waves for P- and S-waves modified for Yellowstone by Clawson et al. (1989) and converted to Q_s by standard methods.

the deep underpinnings of the lithospheric thermal upwelling and extension of the Basin and Range province or a magmatic link to the lower mantle that our data could not resolve.

These tomographically imaged blobs in the mid-mantle may be the source of the upper-mantle Yellowstone plume. Permanent weak, but large-scale, heating below the 660-km discontinuity could lead to localized thermal instabilities in the transition zone that appear as blobs of lower velocity (see supplemental section 3). One or more of those blobs could have coalesced into the Yellowstone plume. The recent western U.S tomographic image of Burdick et al. (2008) reveals a -1% low-velocity body from 660 to ~800 km beneath Yellowstone that is wider than our array could detect. This suggests that a thermal instability from this deeper body could leak blobs of melt into the transition zone.

4.3. Mantle and crustal magma systems

An important, but poorly understood aspect of the Yellowstone hotspot problem is the connection between the Yellowstone crustal magma body and the mantle plume source. The seismic structure of the lower crust and upper-most mantle is poorly constrained as a result of: (1) the lack of lower-crust seismic head-waves; (2) the lack of sufficient regional earthquakes recorded from 200 km to 1000 km distances required in these studies; (3) the lack of local to near regional earthquake sources deeper than the mid-crust, ~16 km maximum depth; (4) the lack of resolution for teleseismic crossing rays; and (5) the lack of resolution of surface waves due to their inherent longer periods and hence longer wavelength resolving kernels.

However, some information bearing on this problem comes from a study using controlled source seismic refraction profiles. Lehman et al. (1982) recognized that the lower crust of Yellowstone was similar to that of the lower crust of the surrounding region, which has been primarily affected by compressional tectonism of the Laramide orogeny at 60–80 Ma. They evaluated the wide-angle reflector from the Moho boundary and found that the travel-times for equivalent ray paths inside and outside the Yellowstone caldera are essentially the

same. This suggested that: (1) the lower crust was homogenous between the active area of Yellowstone volcanism and the surrounding Archean Rocky Mountain crust; and (2) magmas that propagated through the Yellowstone lower crust did not alter the velocity structure and thus the lower crust did not contain large bodies of remnant melt such as the well-resolved low-velocity body in the middle crust (Husen et al., 2004).

A mid-crustal high-velocity sill in the ESRP was identified by seismic refraction, seismic tomography, and receiver function studies (Sparlin et al., 1982; Braile et al., 1982; Lynch et al. 1997; Peng and Humphreys, 1998; Schutt and Humphreys, 2004; Schutt et al., 2008) and interpreted to be a series of gabbroic lenses inter-fingering with the granitic upper crust (see details of the ESRP mid-crustal sill gravity and seismic modeling by DeNosaquo et al., 2009, this volume). This geometry and modeling of the velocity-density relationships yields a bulk composition comparable to diorite and a density of 2900 kg/m³. The high-density mid-crustal sill varies from 4 to 11 km in thickness, resulting in a series of SE-NW-trending gravity highs observed along the axis of the ESRP. The sill extends up to 20 km southeast of the ESRP, producing a corresponding asymmetry of the gravity field (DeNosaquo et al., 2009-this volume). This suggests that basaltic mantle magma ascends buoyantly to mid-crustal depths, where it attains neutral buoyancy and spreads out as a province-wide sill.

On the basis of these generalized data, we hypothesize that magmas rise buoyantly from the plume source at ~70 km depth through a vertically oriented plexus of basaltic dikes in the upper 30 km of the mantle. These dikes possibly pond magma at the Moho to produce underplating, but then continue ascending through the lower crust. As the mafic magma passes through the lower crust, it promotes melting of the surrounding silicic and granulitic host rock, which also ascends. The magma then differentiates into a mid-crustal magma body (Fig. 10) composed of basalt and rhyolitic melts.

Whether the lower crust flows laterally to accommodate the mantle magmas or whether there is a balance between the eruptive volumes and intruded volumes is problematical given the lack of quantitative relationships between the parental and erupted magma volumes, especially those of rhyolitic-basaltic mixes. For connections between the crust and mantle plume between 40 and 70-km depths, the seismic velocity data reveal a different velocity structure than the surrounding region.

Recent studies of the S-wave structure of the YSRP employed surface dispersion analysis (Waite and Smith, 2002; Stachnik et al., 2008; Schutt et al., 2008) to produce a shear velocity model of the Yellowstone hotspot track crust and uppermost mantle. These studies corroborated the high-velocity mid-crustal layer, high-velocity lower crust beneath the Yellowstone caldera, and low-velocity upper crustal body beneath the Yellowstone caldera. These results are similar to the findings of others (Husen et al., 2004; Yuan and Dueker, 2005; Waite et al., 2006). As in the Lehman et al. (1982) study, the lower crust was similar in thickness to areas outside the YSRP. All these studies suggest that the ESRP lower crust may have flowed laterally up to 50–80 km from the YSRP and the seismically quiescent region inboard of the tectonic parabola. They also noted that the ESRP mantle lithosphere has been thinned to about 28 km thickness by the plume's transport of heat and magma ascent.

5. Geodynamic plume modeling

Our tomographic image provides key information for parameterized dynamic modeling of the Yellowstone plume. Geodynamic models were analyzed for the effects of temperature, seismic attenuation, anisotropy, composition and the presence of water or melt on seismic velocity and density (Figs. 18 and S7). Following the work of Karato (1993), temperature is the main source of seismic velocity perturbations in the upper mantle if no heterogeneities in chemical composition are present.

While anisotropy can have a significant effect on seismic traveltimes, it is neglected in this study because the olivine fast axis orientation is approximately unidirectional (Waite et al., 2005). In this case, all compressional P-wave traveltimes from any one event are equally affected. Therefore we concentrate on temperature and composition in terms of the presence of water and melt.

To assess the dynamic properties of the imaged plume, we employed the thermodynamic models of Cammarano et al. (2003) and Cammarano and Romanowicz (2007) with the constraints of our velocity and seismic attenuation models. We realize that our geodynamic plume model is for a one-dimensional case, while we have parameterized data from a three-dimensional structure, but this model should have little effect on the overall dynamic processes given the steep dip of the imaged plume.

Following Cammarano et al. (2003), we first derived models for attenuation for P-waves (Q_p) and S-waves (Q_s) and temperatures in a two-step procedure for dry regimes (Fig. S7). An anelastic model was employed in terms of depth-dependent Q_s -values from the melting curves and temperatures along the geotherm. These Q_s -values then were transformed into Q_p -values (Anderson and Given, 1982) based on the comparison of compressional and shear wave velocity contrasts by Waite et al. (2006). In the next step we calculated the partial velocity derivatives (Fig. S7), following the work of Karato (1993) on olivine polycrystals at upper mantle temperatures and pressures. These values were used to estimate the changes in velocity with temperature for a given attenuation or quality factor, respectively, so that the velocity changes can be modeled and excess temperatures derived as in Fig. 18 (see supplemental section 4).

For a hypothesized water-saturated rock regime, we employed Karato and Jung's (1998) formulation of the effect of water on the seismic velocities by enhancing anelastic relaxation and by lowering the melting point for 2–3% water in the transition zone (Karato and Jung, 1998). We examined the excess temperatures and attenuation properties that can produce the observed reduction in P-wave speed.

Considering the imaged low-velocity zone as a plume conduit consisting of an upwelling of hotter mantle originating in the transition zone, the plume will carry water up into the upper mantle. The effects are decreased viscosity, lowered melting point, and, when the solidus is reached, partial melting. This process will remove water from the solid minerals and therefore increase shear modulus and seismic velocity (Karato and Jung, 1998). Dehydration will reduce the negative effect of increased temperature on the seismic velocities.

Since seismic wave propagation is more affected for S-waves than for P-waves, the dehydration may compensate for the temperature effect on S-wave velocities. Waite et al. (2006) observe such a “hole” in their low-velocity zone at about 200 km depth in their S-wave model but not their P-wave model. This is consistent with findings from Kawamoto and Holloway (1997).

Thus partial melting and dehydration may be responsible for the rapid increase in size of the Yellowstone plume above 200–250 km depth. We estimate the attenuation in terms of Q-values (Q is the seismic attenuation constant) for this case following Karato and Jung (1998) who find $Q_{wet} = 2.5 \cdot Q_{dry}$, based on the enhanced creep rate and frequency dependence. This is consistent with empirical models from Jackson et al. (1992) for dunite composition.

We also calculated the corresponding partial derivatives of velocity with temperature (supplementary data, Fig. S7) and estimated excess temperatures. Ignoring the effect of the partial melting process, we find excess temperatures of 145–168 K in the uppermost mantle, 60–72 K in the lower upper mantle, and 78–85 K in the transition zone, i.e., a relatively cool thermal regime (see Fig. 18). However, partial melting can lower the compressional wave speed between 1.8% (Faul et al., 1994) and 3.6% (Hammond and Humphreys, 2000) per 1% partial melt. Consequently, the amount of partial melt in

the uppermost mantle has to be far less than 1%. Assuming 0.5% melt and the relation of Hammond and Humphreys (2000), this will account for 1.8% velocity reduction leaving -1.2% as a temperature effect.

Our observations and models agree well with the “spout” plumes derived by Farnetani and Samuel (2005), who predicted widespread magma ponding beneath the transition zone and only a narrow tail with 120–180 km diameter and 100–150 K excess temperatures. Moreover, this model also matches the global tomography model by Montelli et al. (2004) and explains our observations of “blobs” of melt in the transition zone. However, our estimated excess temperatures, dry and wet state, are lower than the -200 K determined by Fee and Dueker (2004) from lateral variations of the 410 km discontinuity and for similar calculations by Waite et al. (2006) and Schutt and Dueker (2008) and attest to a cool mantle plume.

6. Deflection of the Yellowstone plume in large-scale mantle flow

Guided by the tomographic images of the tilted Yellowstone upper mantle body and mantle properties derived from the geodynamic model, we evaluated the effect of mantle flow on the orientation of the hypothesized plume. Here we contrast the predicted plume conduit shapes for various modeling assumptions with our upper mantle Yellowstone tomographic plume model. We also compare the predicted hotspot track with geometry and age progression of volcanism along the Snake River Plain, the presumed track of the Yellowstone hotspot (e.g., Smith, 1977; Pierce and Morgan, 1990, 1992; Smith and Braile, 1993, 1994; Pierce et al., 2002).

The general features of plume models have been explained by Steinberger and O'Connell (1998). Regarding specific parameters and characteristics, we follow the work of Steinberger and Antretter (2006), which has been extended to 44 hotspots around the world (including Yellowstone) by Boschi et al. (2007). While the full model description is given in these papers, we are here mostly interested in the plume conduit in the upper mantle, and thus give a simplified description.

If we disregard time dependence, lateral variations, and the vertical components of large-scale flow, we expect that the conduit becomes tilted if the horizontal mantle flow velocity at depth z , $v(z)$, differs from flow $v(z_0)$ at source depth z_0 . More specifically, if conduit ascent speed at depth z is $v_r(z)$, the conduit takes a time $dt = dz/v_r(z)$ to rise through a layer of thickness dz . During this time, it will get displaced relative to the source by an amount $dx = (v(z) - v(z_0))dt = (v(z) - v(z_0))/v_r(z)dz$. Integrating from depth z_0 to depth z thus yields a total displacement

$$x(z) = \int_{z_0}^z (v(z) - v(z_0)) / v_r(z) dz \quad (1)$$

For a source depth at the upper-lower mantle boundary, this implies that conduit tilt should be in the direction of upper mantle flow, relative to flow at source depth, and that the tangent of conduit tilt should be the same order of magnitude as the ratio of horizontal upper mantle flow, relative to flow at source depth, to buoyant rising speed. Under these simplifying assumptions, the shape of the conduit remains constant, but the conduit moves with the flow at source depth. The predicted azimuth and age progression along the hotspot track thus depends on the difference vector between plate motion and flow at source depth.

However, if we initiate the computation with a vertical conduit, the effect of the conduit being progressively tilted by mantle flow introduces a further component of hotspot motion in the direction of upper mantle flow until steady state is reached. If a deeper source depth such as the core-mantle boundary is assumed, then steady-

state is not reached and the conduit will experience tilting in both the lower and upper mantle, with different directions and magnitudes of tilt at depth depending on differences in mantle flow, thus contributing an additional component to hotspot motion.

There are various parameters influencing flow in the mantle, but the largest uncertainties arise from variations in the mantle density models derived from seismic tomographic velocity models, subduction history, and viscosity structure. We use different models to obtain a realistic range of flow and plume conduit shape predictions, and consider several models of plate motion for hotspot track predictions.

Computation of large-scale mantle flow is done with the method of Hager and O’Connell (1979, 1981), employing prescribed plate motions as surface boundary conditions and internal density heterogeneities, both expanded in spherical harmonics, to compute flow. Density variations are inferred from global S-wave tomography models “Smean” (Becker and Boschi, 2002), SAW24B16 (Megnin and Romanowicz, 2000) and TX2007 (Simmons et al., 2006) following

Steinberger and Calderwood (2006) or from subduction history (Steinberger, 2000b).

An example of a flow model is shown in Fig. 19. Computed upper mantle flow in the vicinity of Yellowstone is eastward. This eastward flow is part of a large-scale convection cell with upwelling beneath the Pacific Ocean and downwelling beneath the central and eastern U.S. (Fig. 19) (Bunge and Grand, 2000). The viscosity model primarily used in our models (VM1) was derived by Steinberger and Calderwood (2006) and was based on fitting the geoid and other observational constraints and is consistent with mineral physics. VM2 is a simpler model (Becker et al., 2006) also used in our mantle flow computations. Specifics and parameters of the flow model follow Steinberger and Antretter (2006). This eastward flow in the upper mantle provides a first indication that we should expect an eastward-tilted Yellowstone plume conduit (i.e., coming up from the west).

Fig. 20 shows that this eastward flow component is strongest in the upper mantle and transition zone but decreases with depth until

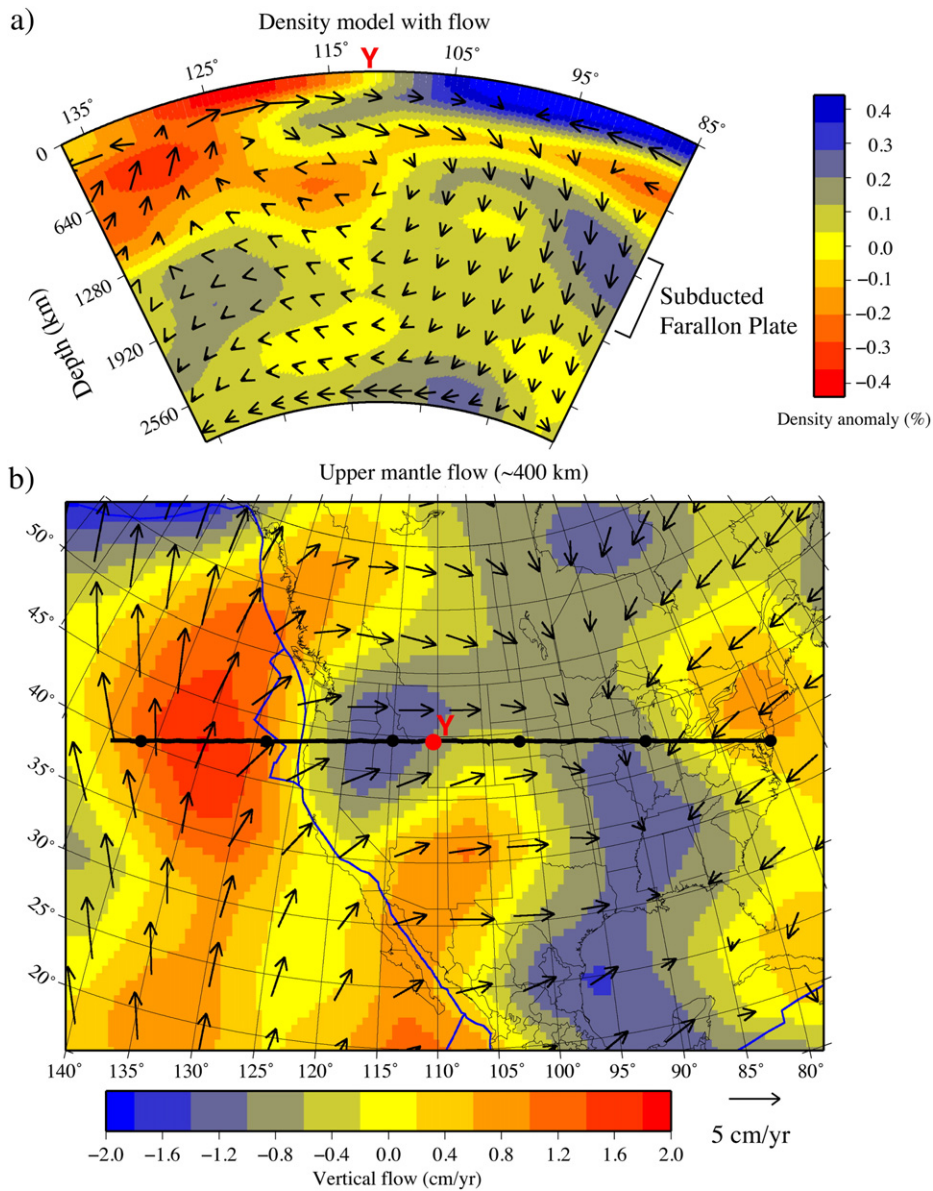


Fig. 19. Computed regional mantle density structure and flow beneath North America and the northeastern Pacific for tomography model S-mean (Becker and Boschi, 2002) with viscosity structure VM1 from Fig. 20. (a) Mantle cross-section showing density structure along the line shown in the bottom panel. The relatively dense subducted Farallon plate is located beneath the eastern U.S. at depths of 1000 to 1900 km. (b) Map view of upper mantle flow at 359 km depth. Vectors represent horizontal components of flow and color background represents vertical flow. Location of Yellowstone at the surface is marked by a red “Y”.

the bottom of the transition zone at 660 km. The flow direction and depth dependence are general features common to a large number of models. However there are variations among the models, with flow direction ranging between southeastward and northeastward, and variable flow speeds.

For the preferred model of Steinberger and Antretter (2006), plume conduit radius in the upper mantle and transition zone is about 100 km, and buoyant rising speed increases from about 2 cm/yr at a depth of 660 km to 10 cm/yr at 400 km and remains approximately constant through the upper mantle. Total rise time from a depth of 660 km is about 12 Ma, about 75% of the ~16 Ma year history of the YSRP. Given typical upper mantle horizontal flow speeds (relative to flow at 660 km) of a few cm/yr (see Fig. 20), we expect a conduit tilted by a few hundred kilometers, and that the surface plume position is displaced relative to the position at a depth of 660 km approximately towards the east, between southeast and northeast.

Our computations confirm this expectation. Fig. 21a shows results for the case of plumes originating from a 660 km depth with no assumptions about the initial conduit made, i.e., all conduit elements originate at depth 660 km and the plume conduit is already tilted when the plume first reaches the surface. Tilts are in directions similar to upper mantle flow, and amounts of tilt vary between less than 100 and ~250 km. Differences between predicted hotspot tracks and the corresponding fixed-hotspot track, shown in Fig. 20, approximately correspond to the amount of plume source displacement due to the

horizontal flow component at a depth of 660 km. Differences between this case and the simplified model above are due to time dependence and the vertical component of the flow field.

Computed tilts are somewhat greater (~150 to 400 km), but generally in the same direction in the case shown in Fig. 21b where plumes rise from the lowermost mantle with an initially vertical conduit (at 15 Ma). This larger tilt can be attributed to the cumulative effect of tilting in the lower mantle added to tilting in the upper mantle. For the plume model based on tomography model SAW24B16, both direction and amount of predicted tilt approximately agrees with the tomographic observations reported here (Figs. 15 and 16). Computed hotspot tracks for the case of a whole-mantle plume tend to be longer (i.e. with the predicted 16 Ma location further from Yellowstone) than in Fig. 21a. This is due to the effect of the initially vertical conduit becoming tilted in the upper and lower mantle.

For models with an initially vertical conduit and plume initiation ages older than 16 Ma, the predicted age progressions become more similar to that shown in Fig. 21a as the “blowing over” effect of upper mantle flow causes the conduit shape to converge with the initially tilted plume models. In the case of plumes rising from the lowermost mantle, the predicted conduit tilt becomes stronger with greater age, as flow in the lower mantle contributes to the total tilt.

In the case of a plume rising from a depth of 660 km but with initially vertical conduit (not shown), predicted tracks are very similar

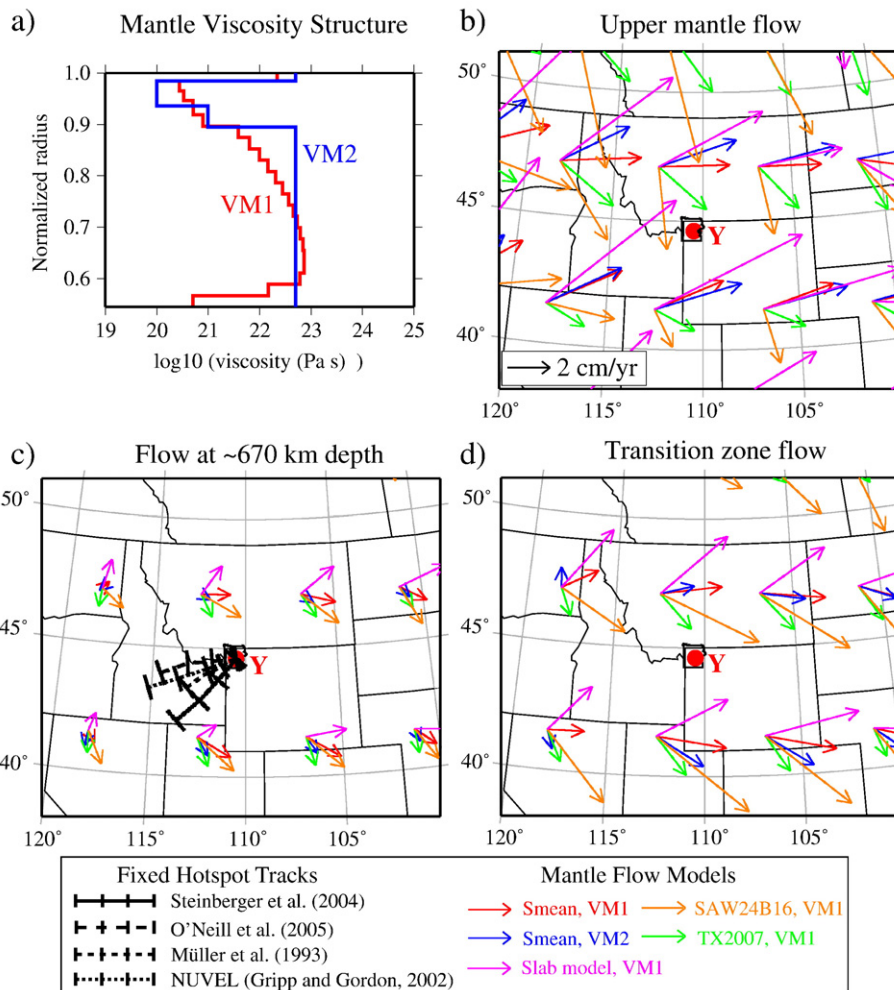
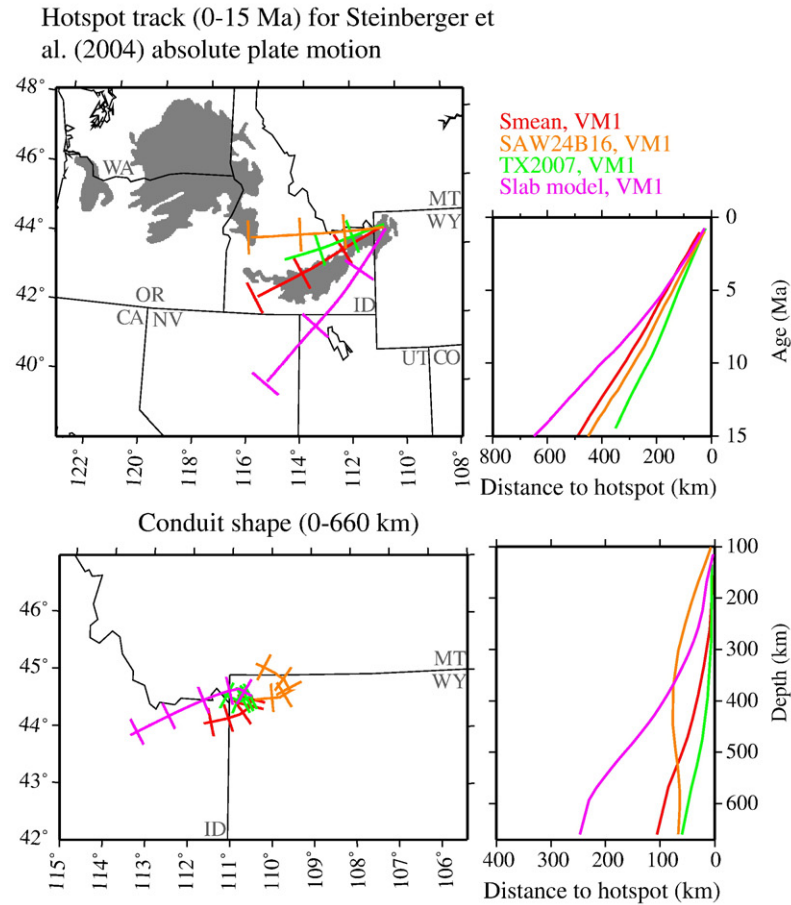


Fig. 20. Computed horizontal upper mantle flow and viscosity structure in the vicinity of the Yellowstone hotspot at various depths. (a) viscosity structure, (b) upper mantle flow, (c) flow at 670 km depth, and (d) in the mantle transition zone. Viscosity models VM1 and VM2, used as the basis of the mantle flow models, are shown in the upper left panel. Model VM1 is derived using the tomography model of Fig. 19. Bottom left panel also includes fixed-hotspot tracks (0–15 Ma) for four different models of North American “absolute” plate motion (Müller et al., 1993; Gripp and Gordon, 2002; Steinberger et al., 2004; O’Neill et al., 2005). Location of Yellowstone at the surface is marked by a red “Y”.

a) Plume from 660 km depth



b) Initially vertical plume from lowermost mantle

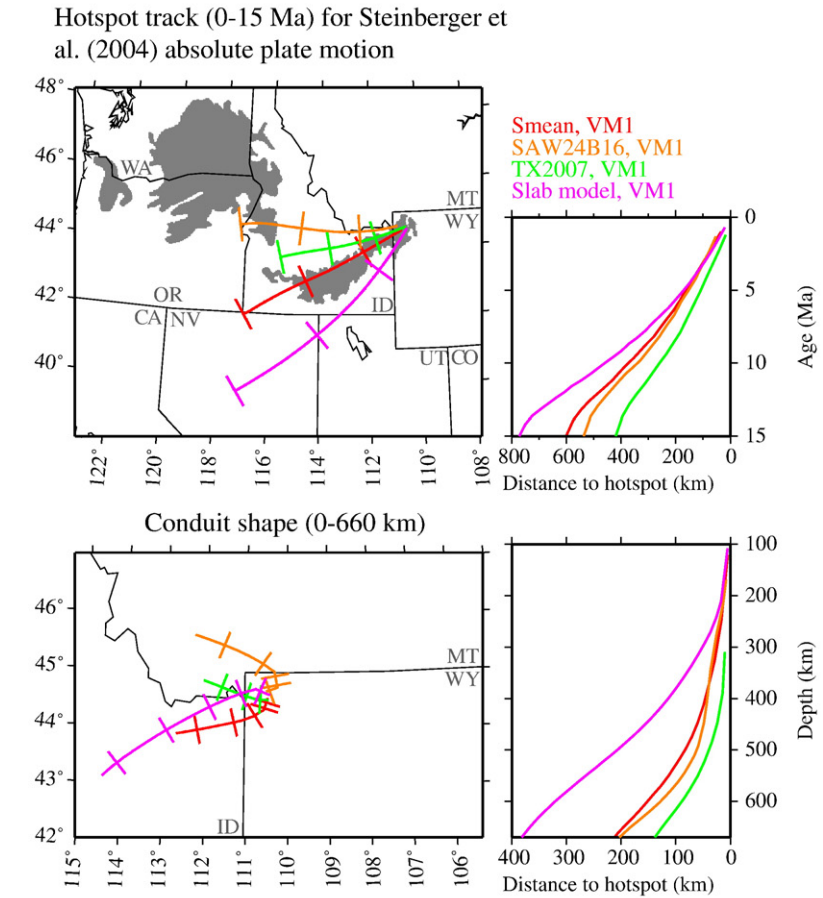


Fig. 21. Models of hotspot plume conduits for (a) plumes ascending from the mantle transition zone (660 km), and (b) initially vertical plumes ascending from the core-mantle boundary. The upper panels in (a) and (b) show the surface hotspot tracks and the progression of surface volcanism over time (0-15 Ma) for plate motion from Steinberger et al. (2004). Gray shaded areas represent provinces of Quaternary volcanism in the Columbia Plateau and eastern Snake River Plain (Suppe et al., 1975). The lower panels show the projection of the plume conduits into map view and plume displacement with depth. Colored lines correspond to mantle flow models from Fig. 20.

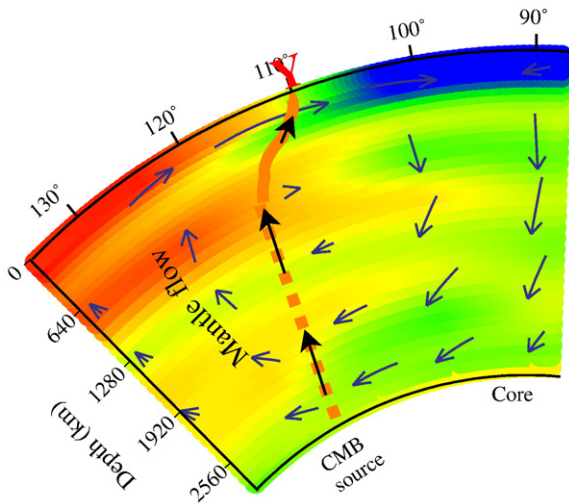


Fig. 22. Cross-section of western North America mantle S-wave velocity structure (cool colors are relatively fast and warm color are higher velocities) from mantle tomography (Su et al., 1994). Mantle flow directions and velocity represented by vectors. Yellowstone mantle plume is superimposed as thick orange line, with hypothesized lower mantle extension shown as a dashed line. The red “Y” marks the surface location of the plume.

to Fig. 21b, because in both cases the effect of the initially vertical conduit becomes “blown over” by the horizontal upper mantle “wind” is important.

We find the best agreement between predicted and observed azimuth and age progression of the hotspot track can be achieved with eastward flow in the upper mantle. The agreement between predicted and observed conduit shape can best be achieved with southeast flow. Moreover the amount of observed tilt can be better matched with our models by having the plume originate in the lower mantle. However, a larger tilt can also result from a slower buoyant rising speed and smaller conduit diameter.

Increasing temperature dependence of viscosity could decrease the conduit rising speed and diameter. Such a stronger temperature dependence would for example result if a linear stress-strain relationship (diffusion creep) was assumed in the upper mantle rather than

dislocation creep with a non-linear stress-strain relationship with stress exponent $n = 3.5$ (as done by Steinberger and Antretter, 2006, whose model we adopt here). Values for conduit diameter (about 100 km; Fig. 16), buoyancy flux (250 kg/s, Section 8), and excess temperature (~120 K) inferred in this paper are all smaller than those adopted in the modeling (~200 km, 2000 kg/s, 200–250 K) following Steinberger and Antretter (2006) and Boschi et al. (2007). Changing to the parameters inferred in this paper would lead to a substantially smaller conduit rising speed and thus larger tilt in the same direction according to Eq. (1).

To emphasize the effect of the mantle flow on plume conduit tilt, we plot in Fig. 22 the flow and conduit for a lowermost mantle plume source from an earlier model superimposed on a background of S-wave velocity structure (Steinberger, 2000a). For this model the plume origin would be at longitude 120°W, beneath Oregon and displaced 800 km west of Yellowstone. The modeled plume location at ~660 km depth is at ~115°W, beneath the Oregon High Lava Plains and the Columbia Plateau flood basalt field. The modeled plume position at the base of the transition zone implies that the plume would have had to initially rise nearly vertically through the upper mantle to produce the Columbia River flood basalts at 17 Ma.

7. Yellowstone geoid anomaly

The Earth's topographic field responds to lithospheric density loads but, along with the long-wavelength gravity field, also reflects deeper mantle sources. To analyze the contribution of mantle sources, we examine the Earth's geoid field. Most of the local geoid features are due to topographic variation, but deep density variations form an important source of the Yellowstone anomaly. The large-scale isostatic properties of the YSRP can be seen in the GEOID03 model for the U.S. (Fig. 23). The model was constructed from a combination of gravity data and orthometric heights determined by geodetic surveys with the resulting equipotential surface reflecting an amalgam of topographic relief and density variation within the Earth (Milbert, 1991).

We parameterized the geometry and density of the Yellowstone geoid model by converting the velocity perturbation structure of the

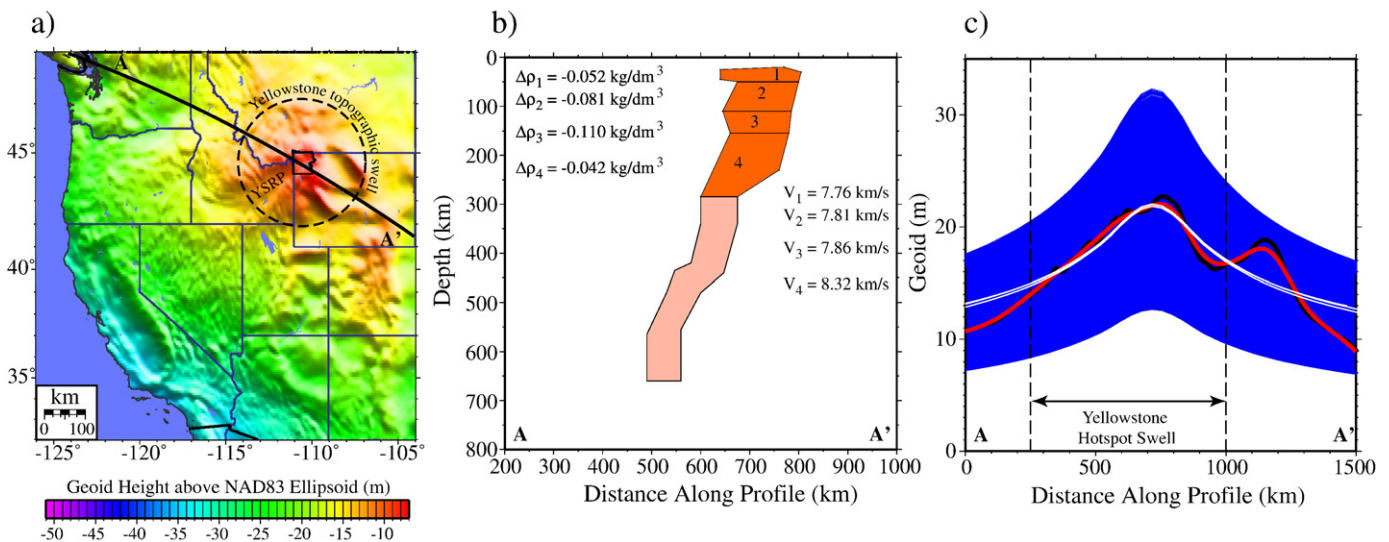


Fig. 23. (a) Geoid map of Western U.S. from GEOID2003 model (Roman et al., 2004) with profile line A-A', (b) parameterized Yellowstone plume model, and (c) 80,000 forward models of the geoid based on plume parameterizations (blue lines) compared to the filtered geoid (red line) in the area of the Yellowstone hotspot swell. Geoid data were shifted relative to background geoid values so that modeled heights ranged from +7 to +30 m. The black line represents the unfiltered geoid and the white lines are selected models discussed in Section 7. The plume in panel (b) was initially parameterized into nine sections, but only the uppermost four segments contributed to the solution. Density perturbations and P-wave velocities for the best-fit model are included in the plot.

Table 1

Table of the B-values and density variations based on the geoid modeling and the results of the optimized tomographic inversion. The B-values and density deviations are given for the optimum result (No.1), and further examples of plausible results at calculation numbers 500 and 1000.

Body #	depth min (km)	depth max (km)	B Model 1	$\Delta\rho$ [kg/dm ³] Model 1	B Model 500	$\Delta\rho$ [kg/dm ³] model 500	B Model 1000	$\Delta\rho$ [kg/dm ³] Model 1000
1	25	50	4.6	-0.052	4.0	-0.060	3.4	-0.071
2	50	110	3.0	-0.081	3.2	-0.076	3.8	-0.064
3	110	155	2.2	-0.110	2.6	-0.093	3.0	-0.081
4	155	285	2.0	-0.042	2.2	-0.038	3.2	-0.026

Yellowstone plume to density variations as a starting model. While the separate derivation of density structure from either velocity perturbations or geoid data is highly non-unique, the combination of both leads to a more constrained solution. Details of the geoid modeling are given in the supplemental section 4.

Forward modelling of the density variation was done on a two-dimensional profile A-A' crossing the Yellowstone hotspot from NW to SE (Fig. 23a). The density model was initially divided into nine bodies extending from 14 km to 660 km in depth, but only the top four layers were found to contribute significantly to the model (Fig. 23b) (Table 1). Each body had a specified velocity perturbation based on the results of the reconstruction tests from the tomographic inversion. Since the true background velocities of the tomographic model are not known, the absolute velocity perturbations are based on the whole-Earth velocity IASP91 P-wave velocity model. 80 000 forward models were run with varying B-value combinations.

We interpret the B-values (the ratio of velocity to density contrast perturbations) to thus reflect density decreases of 1.3% to 3.6% in the upper part of the plume relative to the commonly assumed density of 3400 kg/m³ of the upper mantle (Table 1). The largest density anomaly is in the upper mantle at depths of 150 km to 170 km, the same depth range as the velocity anomaly.

As the temperature reaches the melting point, the seismic velocities decrease rapidly, while the densities decrease slowly, resulting in increased B-values (Schmitz et al., 1997). We interpret the models to indicate that partial melt is present in bodies 1 and 2, but this interpretation is less justified for bodies 3 and 4. Since the absolute velocities and densities are not known we do not determine the absolute percentage of partial melt here. However, modelling of relatively high B-values in bodies 1 and 2 (14 km to 110 km depth) and consistently lower B-values in bodies 3 and 4 (110 km to 285 km depth) indicate significant differences between those two regions within the plume (Table 1). This correlates well with our interpretation of a plume in a wet state, where partial melt is present in the uppermost part of the plume. Below 110 km, the plume was dehydrated by the melting process, reducing the negative effect on the amplitudes of seismic velocity perturbations but only slightly changing the density variations, i.e., reducing the B-values.

Our B-value calculations thus predict a relative low-temperature excess of the Yellowstone plume of 70 K to 250 K, averaging 150 K depending on the relative hydrous content (Fig. 18). These values compare to excess temperatures averaging ~250 K for the Hawaii and Iceland plumes and lead to the important conclusion that the Yellowstone plume is weak and correspondingly cool.

8. Effects of mantle on the overriding lithosphere

On a global scale, we compare our hypothesized Yellowstone plume with other hotspots by computing the buoyancy flux using properties derived from tomographic models after the method of Ritter (2005) (Fig. 24). The buoyancy flux is estimated from the width and elevation of the hotspot topographic or bathymetric anomalies, velocity of the overriding plate, and excess plume temperature (e.g., Davies, 1988; Sleep, 1990, 2006). Given the small (< 150 K) excess temperatures predicted for a dry mantle with low Q (estimated jointly

from the V_p and V_s models), the Yellowstone buoyancy flux is at least one order of magnitude lower than previous estimates (Sleep, 1990; Smith and Braile, 1993, 1994; Lowry et al., 2000; Nolet et al., 2006; Stachnik et al., 2008; Schutt et al., 2008). Likewise the Yellowstone buoyancy flux is estimated to be an order of magnitude lower than its oceanic counterparts below Iceland and Hawaii, which have flux values of 1.4 Mg/s and 8.7 Mg/s, respectively (Sleep, 1990). At 0.25 Mg/s, Yellowstone is comparable to the other continental hotspots with weak flux, calculated by Ritter (2005) to be 0.09 Mg/s at Eifel and 0.7 Mg/s at the Massif Central. A main consequence of such a weak flux is that the low volume of ascending magma and reduced excess temperature together produce less melting. The results are a lower plume buoyancy and reduced impact on lithosphere uplift and magmatic volume (Waite, 2004).

An alternate interpretation of a volcanic source for Yellowstone that cannot be ruled out is that the upper mantle velocity anomaly may be caused by magma rising in a weak or thinned lithosphere. If the lithosphere has been eroded along a preexisting structural weakness, then the upwelling could follow the path of least resistance to the surface. This idea has been invoked by some researchers to explain the dynamics of the Yellowstone system without a plume (e.g., Smith and Sbar, 1974; Smith, 1977; Favela and Anderson, 2000; Dueker et al., 2001; Christiansen et al., 2002). The nature of the structural weakness varied: (1) Smith and Sbar (1974) proposed a transition from the Northern Rocky Mountains to Basin and Range lithospheric microplates, which had differential motion; (2) Smith (1977, 1978) proposed a continental triple junction in northern Nevada, with the YSRP corresponding to a propagating rift arm; and (3) Christiansen and McKee (1978) proposed a right-lateral transform

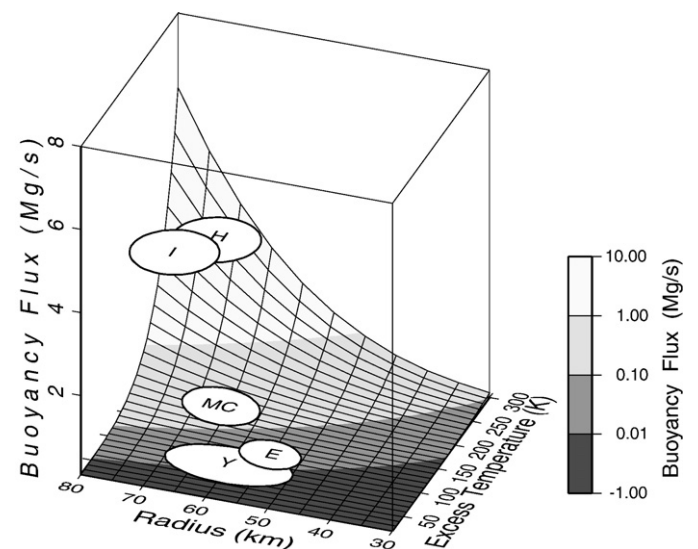


Fig. 24. Comparison of buoyancy flux, plume radii and excess temperature estimates for oceanic and continental plumes. White circles approximate the uncertainty. Radius and excess temperature estimates of Eifel (E), Massif Central (MC), and Yellowstone (Y) from tomographic images are used to estimate the buoyancy flux using the method of Ritter (2005). The buoyancy fluxes for Iceland (I) and Hawaii (H) are taken from Sleep (1990). Calculations are for a mantle temperature of 1300 °C.

1975; Pierce and Morgan, 1990, 1992; Hughes and McCurry, 2002; Perkins and Nash, 2002). The configuration of subducting slab and thin oceanic lithosphere and thick continental lithosphere in the Pacific Northwest has important implications for the evolution of Yellowstone hotspot volcanism.

In Figs. 25 and 26 we illustrate the conceptual idea of time-spatial evolution of the YSRP in terms of the plume-plate interaction model. The plot is for a fixed mantle source under the southwestward moving North America plate. The original voluminous plume head rose vertically from the deep mantle and became entrained in westward return flow driven by the eastward subduction of the Juan de Fuca plate. The relatively weaker and thinner oceanic lithosphere allowed the plume head to spread out and protected the plume from the eastward currents that dominated upper mantle convective return flow below the thicker continental lithosphere to the east. As the North America plate progressed southwest it encountered the much thicker continental lithosphere and lost the protection of the back-arc geometry from large-scale mantle flow. Several authors (Pierce and Morgan, 1990, 1992; Camp, 1995; Perkins et al., 1998; Pierce et al., 2000; Hughes and McCurry, 2002; Nash et al., 2006) have suggested that the transition from accreted to cratonic lithosphere and a shift from westward to eastward mantle flow occurred at the Oregon-Idaho border. Here a plume with a conduit

diameter of ~70 km as derived from our seismic tomography (compare Fig. 16) (see also Nash et al., 2006) became caught in the mantle return flow, tilting it and smearing out the magma against the overriding lithosphere. This process was responsible for the YSRP hotspot track.

A further consequence of this model would be the southward offset of volcanism over time relative to the initial upper-mantle plume head source. The original Yellowstone-related studies by Pierce and Morgan (1990, 1992, 2009-this volume), Nash et al. (2006), and Camp and Ross (2004) argue for a widely distributed area of initial silicic volcanism over southeastern Oregon with the possibility of plume origin for the Columbia River basalt group (Armstrong, 1978; Brandon and Goles, 1988; Hooper and Hawkesworth, 1993; Geist and Richards, 1993; Camp, 1995; Takahashi et al., 1998; Pierce et al., 2000; Camp and Hanan, 2008). That is, later Yellowstone volcanism was offset to the south of initial volcanism in eastern Oregon. However, if we assume a linear track for the North America plate over the base of the plume at 660-km depth as well as at the top of the plume, then the trace of the mantle source follows a southwest trend beneath the northern Rockies and the Idaho Batholith, ending below the western Snake River Plain, notably ~150 km north of the originally defined beginning of the YSRP, at the McDermitt volcanic field in Nevada (Glen and Ponce, 2002) (Fig. 26).

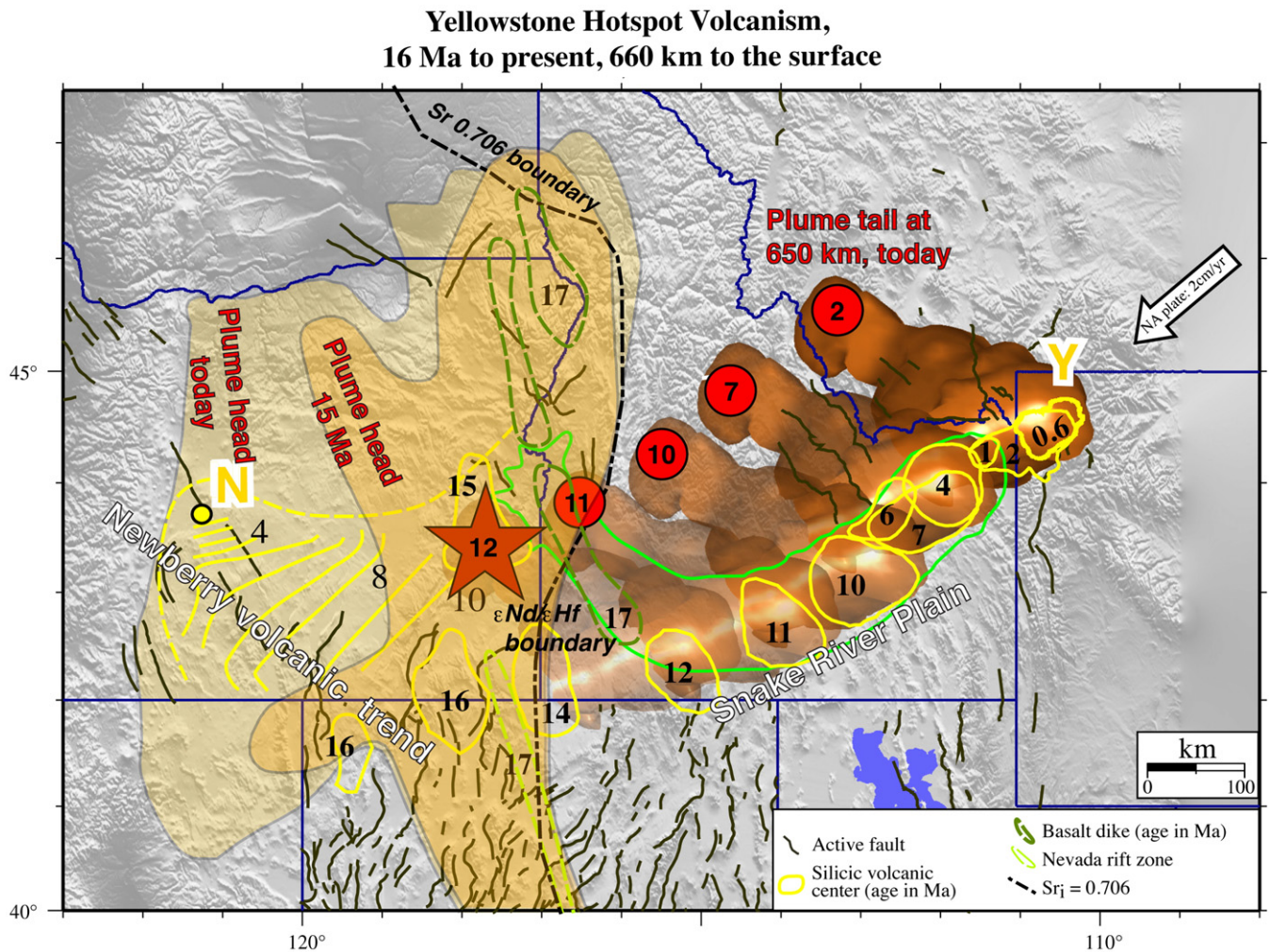


Fig. 26. Hypothesized track of the Yellowstone plume tail, at ~660-km depth originating 150 km west of Yellowstone, to its origin as a tilted structure at 14 Ma ~400 km southwest. The plume image from Fig. 17 is superimposed on a topographic background. From 17 Ma to 12 Ma the plume had a vertical ascending path beneath the Columbia Plateau west of the $^{87}\text{Sr}/^{86}\text{Sr}=0.706$ boundary (dashed black line), i.e., to the original area of plume-plate interaction that spread out beneath the oceanic lithosphere as proposed by plume by Camp and Ross (2004). The plume was then tilted 60° to the NW by return mantle flow, so that the plume base (red circles) were offset from surface silicic volcanic centers (yellow circles). Also shown are basaltic dikes as dashed green lines.

Our resulting image of the Yellowstone plume is consistent with the eastern Oregon-Washington state area hypothesized to be affected by the plume head (Duncan, 1982; Pierce and Morgan, 1990, 1992; Camp, 1995; Pierce et al., 2000; Glen and Ponce, 2002; Camp and Ross, 2004; Shervais and Hanan, 2008). This area encompasses much of the silicic volcanic area of the Oregon High Lava Plains and the southern part of the Columbia Plateau flood basalt field. This suggests that Columbia Plateau basalt deposition that began at ~17 Ma may have had a common mantle source with the YSRP, i.e., both fueled by the Yellowstone plume. This concept is also corroborated by the geochemical analysis of Hanan et al. (2008) who noted that the Steens basalt eruptive center might have been an early eruptive phase of the Columbia River basalts and is also located near our modeled location of the Yellowstone plume head at 17 Ma.

9. Concluding remarks

The Yellowstone hotspot results from interaction of an upper mantle plume with the overriding North America plate. Sub-lithosphere ponding of hot, low-density material results in a large topographic swell over the continental part of the hotspot track. Kinematically, the plume magma is sheared to the southwest against the southwest moving North America plate (Lowry et al., 2000), producing an elongate plume head beneath the ESRP and Yellowstone. Regionally, lithospheric extension driven by the high gravitational potential (GPE) related to the high elevation of the Yellowstone plateau results in SW motion of the YSRP (Puskas and Smith, 2009) that becomes part of a larger kinematic pattern of clockwise rotation of the western U.S.

Our results confirm that the Yellowstone Plateau volcanic field is the locus of the highest level of seismicity in the Rocky Mountains. It has experienced the largest historic, and deadly, earthquake, the 1959 M7.5 event, of the Intermountain region. Local earthquake tomography images of Yellowstone confirm a low- V_p magma body beneath the 0.64 Ma Yellowstone caldera at 8–16-km depth, with 8–15% melts, i.e. the Yellowstone magma reservoir. Heat flow of 2000 mWm⁻² and Yellowstone's Quaternary silicic volcanism from this crustal magma system drives hydrothermal activity across the Yellowstone Plateau.

Contemporary deformation of the Yellowstone caldera determined from geodetic measurements reveals an energetic system dominated by Basin-Range lithospheric extension of up to 4 mm/yr with superimposed volcanic uplift and subsidence with average rates of ~2 cm/yr. The caldera has experienced an unexpected episode of accelerated uplift from 2004 to 2009 at up to 7 cm/yr that is attributed to magmatic recharge of the crustal magma system.

Teleseismic tomography employing V_p inversion imaged a P-wave low-velocity body from 80 to 250-km depth vertically beneath Yellowstone, but continuing at a tilt of 60° from the vertical to the bottom of the transition zone at 660 km, 150 km northwest of Yellowstone. We interpret this conduit of melt to be the Yellowstone plume. Dynamic models of the plume reveal excess temperature of 85–120 K and up to 2.5% melt with a buoyancy flux of ~0.25 Mg/s, several times smaller than oceanic plumes. This implies the Yellowstone plume is weak and cool.

Employing the inclined plume-geometry and plate motion history, we extrapolate the hotspot track southwestward over the upper mantle-source to an initial position at 16 to 17 Ma. This position is beneath eastern Oregon and the southern part of the Columbia Plateau flood basalt field, suggesting a common source for the entire YSRP system (Fig. 26). Our model is consistent with the original plume head rising vertically behind the subducting Juan de Fuca plate, but at ~12 million years it encountered cooler continental lithosphere and horizontal mantle flow, imparting the observed westward tilt.

Although this paper addresses new research findings to produce an integrated analysis of the Yellowstone plume and volcanic history of the Yellowstone hotspot, several issues remain to be addressed. The

dynamics and plumbing of magma generation in the upper mantle and its subsequent transport from the tilted plume through the lithosphere into the upper crust has not been resolved. The mantle plume contributes to the Yellowstone topographic swell and geoid anomaly, but the processes through which the plume contributes to regional extension at the surface and enhances magma emplacement requires further study.

The widespread Yellowstone hydrothermal activity is driven by heat from a shallow crustal magma reservoir, but the processes of heat and fluid transport are poorly understood. More work needs to be undertaken to evaluate the spatial distribution of Yellowstone thermal features, temporal changes in thermal activity, and the thermal and mechanical connections between surface features and crustal magma. Understanding the processes of changes of Yellowstone caldera magmatic transport (i.e., magma intrusion, dike injection, escape of volatiles, etc.) and how they contribute to local deformation requires further quantitative analysis. Moreover stress interactions between faults and the volcanic system at short and long time scales and their effects on earthquake and volcano hazards remain poorly understood but are a key research goal. These topics provide opportunities for investigation and quantitative modeling of the interaction between geochemical and geophysical characteristics of the Yellowstone hotspot.

In conclusion, it is clear that the Yellowstone plume has had a profound effect on much of the western U.S. interior with hotspot-driven Cenozoic volcanism affecting lithospheric structure, stress state, deformation, and topography. Hotspot volcanism has produced the geology and environment that was used as the basis for designating the world's first national park of Yellowstone National Park, highlighting its world-renowned hot springs and geysers. These thermal phenomena are driven by extraordinarily high heat flow that in turn is caused by its active crustal magma and upper mantle sources (A 3D animated image of our Yellowstone plume body from our data can be downloaded from our supplemental electronic section 1).

Our results demonstrate the kinematics and dynamic properties of the Yellowstone hotspot leads to the recognition of its "a living, breathing, shaking" caldera and the overall volcanic and tectonic processes of Yellowstone hotspot emphasize that view that it is truly "A Window into the Earth's Interior".

Acknowledgements

Collaborators in the Yellowstone Geodynamic Project included Richard Allen, Ulrich Achauer, David Blackwell, Larry Braile, Robert Christiansen, Ken Dueker, Robert Fournier, Ronald Harris, Paul Hearnlund, David Hill, Eugene Humphreys, Rick Hutchinson, Eduard Kissling, Lee Siegel and Paul Tackley. Our research materially benefited with discussions and support from David Drobeck, Charles Meertens, Henry Heasler, David Lageson, Dan Dzurisin, Anthony Lowry, Harley Benz, Barbara Nash, Michael Perkins, John Shervais, Jake Lowenstern, Lisa Morgan, Kenneth Pierce, Suzette Payne, and David Rodgers. Suzette Payne, Ronald Harris and Rob Reilinger assisted with GPS developments. We appreciate the support with data acquisition of our Yellowstone projects from the National Science Foundation, the U.S. Geological Survey, Yellowstone and Grand Teton National Parks, the Idaho National Laboratory (INL), the Yellowstone Volcano Observatory, and the Plate Boundary Observatory. The University of Utah provided computational support and technical assistance and the University of Utah Seismograph Stations provided engineering support for seismic and GPS monitoring. The IRIS-PASSCAL project provided portable seismographs and UNAVCO provided GPS instruments. We appreciate the critical reviews of Joachim Ritter, an anonymous reviewer, and the JVGR editors that greatly improved our paper. Herman Engelen at Elsevier Inc. helped us greatly in the final editing of this paper. Our long-term Yellowstone hotspot research was primarily supported by the National Science Foundation Continental Dynamics program grants #EAR 9725431, 0314298, 9725431, and 9316289. Funding for our basic

Yellowstone research has also been provided by William and Sue Carrico Family and by The Brinson Foundation.

Appendix A. Supplementary data

Supplementary data associated with this article can be found, in the online version, at doi:10.1016/j.jvolgeores.2009.08.020.

References

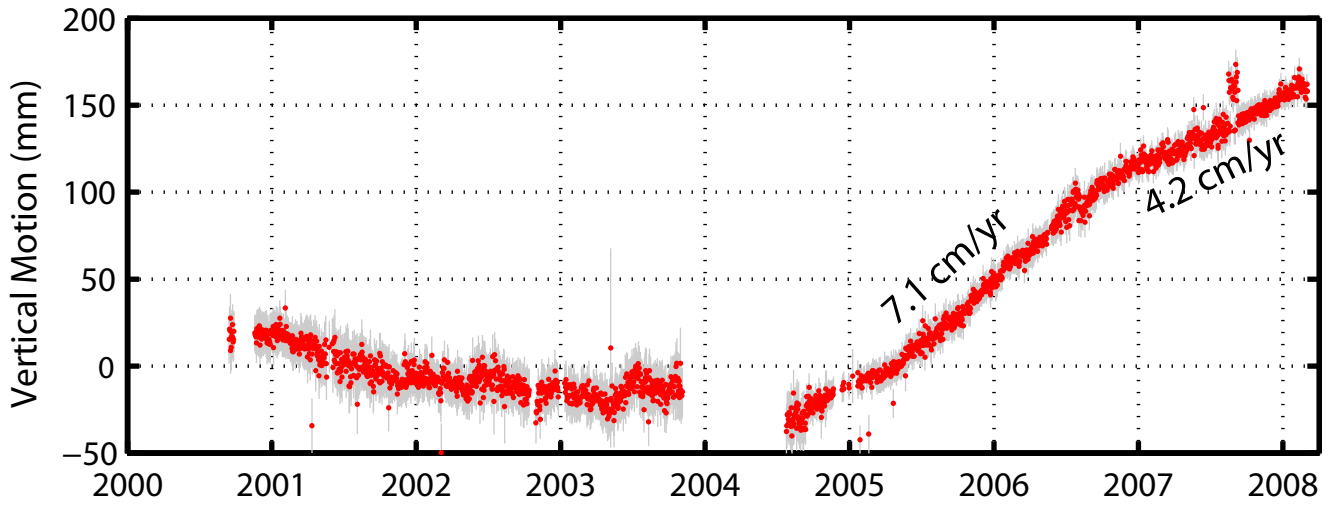
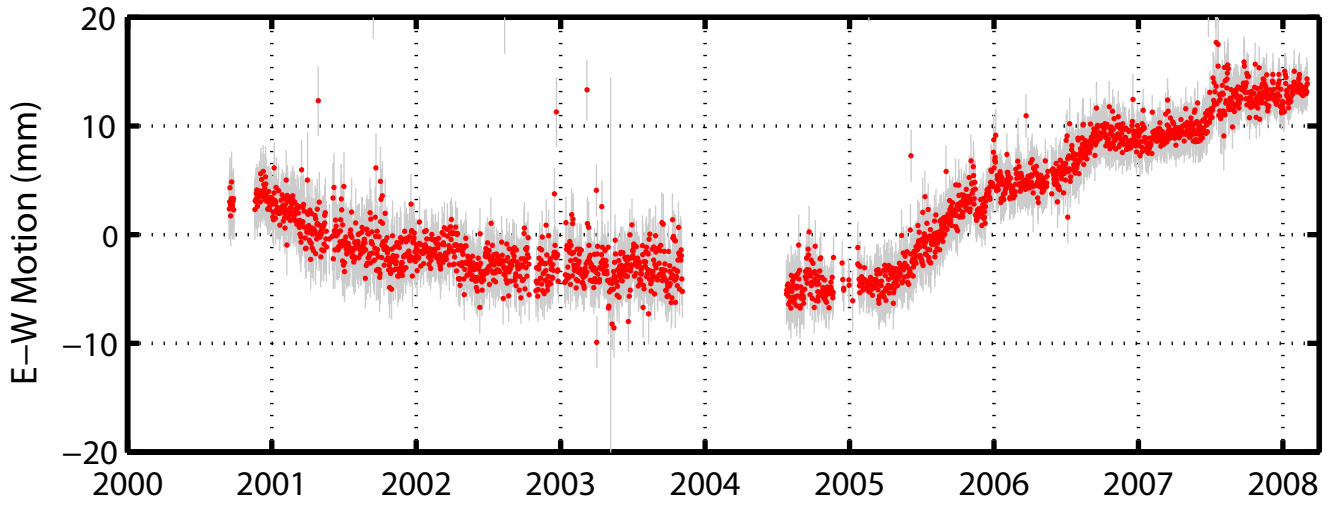
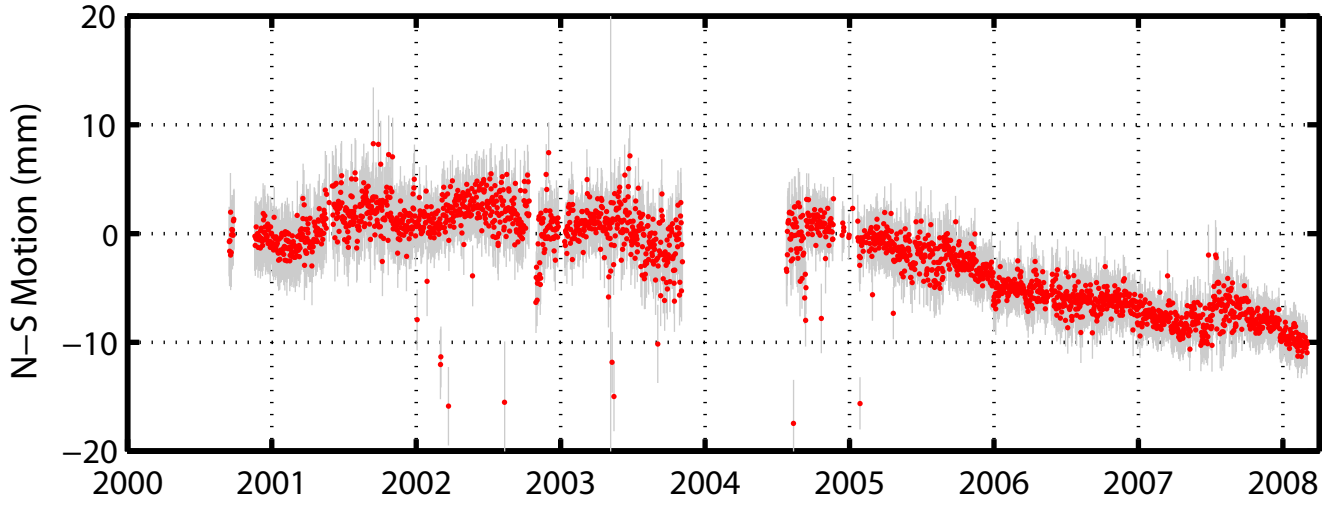
- Allen, R.M., Nolet, G., Morgan, W.J., Vogt, K., Bergsson, B.H., Erlendsson, P., Foulger, G.R., Jakobsdottir, S., Julian, B.R., Pritchard, M., Ragnarsson, S., Stefansson, R., 2002. Imaging the mantle beneath Iceland using integrated seismological techniques. *J. Geophys. Res.* 107. doi:10.1029/2001JB000595.
- Anders, M.H., Geissman, J.W., Piety, L.A., Sullivan, J.T., 1989. Parabolic distribution of circum-eastern Snake River Plain seismicity and Late Quaternary faulting: migratory pattern and association with the Yellowstone hotspot. *J. Geophys. Res.* 94, 1589–1621.
- Anders, M.H., Sleep, N.H., 1992. Magmatism and extension: The thermal and mechanical effects of the Yellowstone hotspot. *J. Geophys. Res.* 97, 15,379–15,393.
- Anderson, D.L., 2000. The thermal state of the upper mantle: no role for mantle plumes. *Geophys. Res. Lett.* 27, 3623–3626.
- Anderson, D.L., Given, J.L., 1982. Absorption band Q model for the earth. *J. Geophys. Res.* 87, 3893–3904.
- Annen, C., Blundy, J.D., Sparks, R.S., 2006. The genesis of intermediate and silica magmas in deep crustal hot zones. *J. Pet.* 47, 505–539.
- Armstrong, R.L., 1978. Cenozoic igneous history of the U.S. Cordillera from lat 42° to 49° N. In: Smith, R.B., Eaton, G.P. (Eds.), *Cenozoic Tectonics and Regional Geophysics of the Western Cordillera: Geological Society of America Memoir 152*. GSA, Boulder, CO, pp. 265–282.
- Armstrong, R.L., Leeman, W.P., Malde, H.E., 1975. K–Ar dating, Quaternary and Neogene volcanic rocks of the Snake River Plain Idaho. *Am. J. Sci.* 275, 225–251.
- Armstrong, R.L., Taubeneck, W.P., Hales, P.O., 1977. Rb–Sr and K–Ar geochronometry of Mesozoic granitic rocks and their Sr isotopic composition, Oregon, Washington, and Idaho. *Geol. Soc. Am. Bull.* 88, 397–411.
- Atwater, T., 1970. Implications for plate tectonics for the Cenozoic tectonic evolution of western North America. *Geol. Soc. Am. Bull.* 81, 3513–3536.
- Atwater, T., Stock, J., 1988. Pacific–North America plate tectonics of the Neogene Southwestern United States – an update. *Int. Geol. Rev.* 40, 375–402.
- Barth, A., Jordan, M., Ritter, J., 2007. Crustal and upper mantle structure of the French Massif Central plume. In: Ritter, J.R., Christensen, U.R. (Eds.), *Mantle Plumes – A Multidisciplinary Approach*. Springer Verlag, Heidelberg, pp. 159–184.
- Becker, T.W., Boschi, L., 2002. A comparison of tomographic and geodynamic mantle models. *Geochem. Geophys. Geosys.* 3 (1), 1003. doi:10.1029/2001GC000168.
- Becker, T.W., Chevrot, S., Schulte-Pelkum, V., D.K. Blackman, D.K., 2006. Statistical properties of seismic anisotropy predicted by upper mantle geodynamic models. *J. Geophys. Res.* 111, B08309. doi:10.1029/2005JB004095.
- Bennett, R.A., Davis, J.L., Normandeau, J.E., Wernicke, B.P., 2001. Space geodetic measurements of plate boundary deformation in the western U.S. Cordillera. In: Stein, S., Freymueller, J. (Eds.), *Plate Boundary Zones*. AGU, Washington, D.C., pp. 27–55.
- Bina, C.R., Helffrich, G., 1994. Phase transition Clapeyron slopes and transition zone seismic discontinuity topography. *J. Geophys. Res.* 99, 15,853–15,860.
- Blackwell, D.D., 1989. Regional implications of heat flow of the Snake River Plain, northwestern United States. *Tectonophysics* 164, 323–343.
- Blackwell, D. D., Richards, M. C., 2004. Geothermal Map of North America. American Association of Petroleum Geologists, 1 sheet, scale 1:6,500,000.
- Blackwell, D.D., Negraru, P.T., Richards, M.C., 2006. Assessment of the enhanced geothermal system resource base of the United States. *Nat. Resources Res.* 15 (4), 283–308. doi:10.1007/s11053-007-9028-7.
- Bonnichsen, B., 1982. Rhyolite Lava Flows in the Bruneau-Jarbridge Eruptive Center, Southwestern Idaho. In: Bonnichsen, B., Breckenridge, R.M. (Eds.), *Cenozoic Geology of Idaho: Idaho Bureau of Mines and Geology Bulletin*, vol. 26, pp. 283–320. Moscow, ID.
- Bonnichsen, B., Leeman, W.P., Honjo, N., McIntosh, W.C., Godchaux, M.M., 2008. Miocene silicic volcanism in southwestern Idaho: geochronology, geochemistry, and evolution in the central Snake River Plain. *Bull. Volcanol.* 70 (3), 315–342. doi:10.1007/s00445-007-0141-6.
- Boschi, L., Becker, T.W., Steinberger, B., 2007. Mantle plumes: Dynamic models and seismic images. *Geochem. Geophys. Geosys.* 8, Q10006. doi:10.1029/2007GC001733.
- Boyd, F.R., 1961. Welded tuffs and flows in the rhyolite plateau of Yellowstone National Park. *Geol. Soc. Am. Bull.* 72, 387–426.
- Brandon, A.D., Goles, G.C., 1988. A Miocene subcontinental plume in the Pacific Northwest: geochemical evidence. *Earth Planet. Sci. Lett.* 88 (304), 273–283.
- Braille, L.W., Smith, R.B., Ansorge, J., Baker, M.R., Sparlin, M.A., Prodehl, C.M., Schilly, M.M., Healy, J.H., Mueller, S., Olsen, K.H., 1982. The Yellowstone Snake River Plain seismic profiling experiment: Crustal structure of the eastern Snake River Plain. *J. Geophys. Res.* 84, 2597–2610.
- Brott, C.A., Blackwell, D.D., Ziegler, J.P., 1981. Thermal and tectonic implications of heat flow in the eastern Snake River Plain, Idaho. *J. Geophys. Res.* 86, 11,709–11,734.
- Bunge, H.-P., Grand, S.P., 2000. Mesozoic plate-motion history below the northeast Pacific Ocean from seismic images of the subducted Farallon slab. *Nature* 405, 337–340.
- Burchfiel, B.C., Cowan, D.S., Davis, G.A., 1992. Tectonic overview of the Cordilleran orogen in the western United States. In: Burchfiel, B.C., Lipman, P.W., Zoback, M.L. (Eds.), *The Cordilleran Orogen: Conterminous U.S. : The Geology of North America*, Volume G-3. GSA, Boulder, CO, pp. 407–480.
- Burdick, S., Li, C., Martynov, V., Cox, T., Eakins, J., Mulder, T., Astiz, L., Vernon, F.L., Pavlis, G.L., van der Hilst, R., 2008. Upper mantle heterogeneity beneath North America from travel time tomography with global and USArray Transportable array data. *Seismol. Res. Lett.* 79 (3), 384–392.
- Burov, E., Guillou-Frottier, L., 2005. The plume head–continental lithosphere interaction using a tectonically realistic formulation for the lithosphere. *Geophys. J. Int.* 161 (2), 469–490.
- Burov, E., Guillou-Frottier, L., d’Acremont, E., Le Pourhiet, L., Cloetingh, S., 2007. The plume head lithosphere interactions near intra-continental plate boundaries. *Tectonophysics* 434, 15–38.
- Cammarano, F., Goes, S., Vacher, P., Giardini, D., 2003. Inferring upper mantle temperatures from seismic velocities. *Phys. Earth Planet. Int.* 138, 197–222.
- Cammarano, F., Romanowicz, B., 2007. Insights into the nature of the transition zone from physically constrained inversion of long-period seismic data. *Proc. Nat. Acad. Sci. U.S.A.* 104 (22), 9139–9144.
- Camp, V.E., 1995. Mid-Miocene propagation of the Yellowstone mantle plume head beneath the Columbia River basalt source region. *Geology* 23 (5), 435–438.
- Camp, V.E., Ross, M.E., 2004. Mantle dynamics and genesis of mafic magmatism in the intermontane Pacific Northwest. *J. Geophys. Res.* 109, B08204. doi:10.1029/2003JB002838.
- Camp, V.E., Hanan, B.B., 2008. A Plume-triggered delamination origin for the Columbia River Basalt Group. *Geosphere* 4 (3), 480–495.
- Carlson, R.W., Hart, W.K., 1988. Flood basalt volcanism in the northwestern United States. In: Maccougall, J.D. (Ed.), *Continental Flood Basalts*. Kluwer Academic Publishers, Dordrecht, The Netherlands, pp. 35–61.
- Chang, W., Smith, R.B., Wicks, C., Puskas, C., Farrell, J., 2007. Accelerated uplift and source models of the Yellowstone caldera, 2004–2006, from GPS and InSAR observations. *Science* 318 (5852), 952–956. doi:10.1126/science.1146842.
- Christiansen, R.L., 1972. Cenozoic volcanism and plate-tectonic evolution of the Western United States: Part 2, Late Cenozoic. *R. Soc. Lond. Phil. Trans.* 271 (A), 249–284.
- Christiansen, R.L., 1984. Yellowstone magmatic evolution: Its bearing on understanding large-volume explosive volcanism. In: National Research Council Studies in Geophysics (Editors), *Explosive Volcanism: Inception, Evolution, and Hazards*. National Academy of Sciences, Washington, D. C., pp. 84–95.
- Christiansen, R.L., 2001. The Quaternary and Pliocene Yellowstone Plateau volcanic field of Wyoming, Idaho, and Montana. *U. S. Geol. Surv. Prof. Pap.* 729-G. U. S. Geol. Surv., Denver, CO, 120 pp.
- Christiansen, R.L., McKee, E.H., 1978. Late Cenozoic volcanic and tectonic evolution of the Great Basin and Columbia intermontane regions. In: Smith, R.B., Eaton, G.P. (Eds.), *Cenozoic Tectonics and Regional Geophysics of the Western Cordillera: Geological Society of America Memoir 152*. GSA, Boulder, CO, pp. 283–311.
- Christiansen, R.L., Foulger, G.R., Evans, J.R., 2002. Upper-mantle origin of the Yellowstone hotspot. *Geol. Soc. Am. Bull.* 114, 1245–1256.
- Christiansen, R.L., Lowenstern, J.L., Smith, R.B., Heasler, H., Morgan, L.A., Nathenson, M., Mastin, L.G., Muffler, L.J.P., Robinson, J.E., 2007. Preliminary Assessment of Volcanic and Hydrothermal Hazards in Yellowstone National Park and Vicinity. *U. S. Geol. Surv. Open File Rpt.* 2007-1071 94 pp.
- Clawson, S.R., Smith, R.B., Benz, H.M., 1989. P-wave attenuation of the Yellowstone caldera from three-dimensional inversion of spectral decay using explosion source seismic data. *J. Geophys. Res.* 94, 7205–7222.
- Condie, K.C., 2001. Mantle plumes and their record in Earth history. Cambridge Univ. Press. ISBN-13: 9780521014724, 320 pp.
- Coney, P.J., 1978. Mesozoic–Cenozoic Cordilleran plate tectonics. In: Smith, R.B., Eaton, G.P. (Eds.), *Cenozoic Tectonics and Regional Geophysics of the Western Cordillera: Geological Society of America Memoir 152*. GSA, Boulder, CO, pp. 33–50.
- Courtilot, V., Davaille, A., Besse, J., Stock, J., 2003. Three distinct types of hotspots in the Earth’s mantle. *Earth Planet. Sci. Res. Lett.* 205, 295–308.
- Craig, H., Lupton, J.E., Welhan, J.A., Poreda, R., 1978. Helium isotope ratios in Yellowstone and Lassen Park volcanic gases. *Geophys. Res. Lett.* 5 (11), 897–900.
- Crough, S.T., 1978. Thermal origin of mid-plate hot-spot swells. *Geophys. J. R. Astron. Soc.* 55, 451–469.
- Crough, S.T., 1983. Hotspot swells. *Annu. Rev. Earth Planet. Sci.* 11, 165–193.
- Davies, G.F., 1988. Ocean bathymetry and mantle convection, 1, Large-scale flow and hotspots. *J. Geophys. Res.* 93, 10,467–10,480.
- DeNosaquo, K., Smith, R.B., Lowry, A.R., 2009. Density and lithospheric strength models of the Yellowstone–Snake River Plain volcanic system from gravity and heat flow data. *J. Volcanol. Geotherm. Res.* 188, 108–127.
- Dickinson, W.R., 2004. Evolution of the North America Cordillera. *Annu. Rev. Earth Planet. Sci.* 32, 13–45.
- Dietz, R.S., Holden, J.C., 1970. Reconstruction of Pangaea: Breakup and dispersion of continents, Permian to present. *J. Geophys. Res.* 75, 4939–4956.
- Doe, B.R., Leeman, W.P., Christiansen, R.L., Hedge, C.E., 1982. Lead and strontium isotopes and related trace elements as genetic tracers in the upper Cenozoic rhyolite–basalt association of the Yellowstone plateau volcanic field. *J. Geophys. Res.* 87 (B6), 4785–4806.
- Doser, D.I., 1985. Source parameters and faulting processes of the 1959 Hebgen Lake, Montana, earthquake sequence. *J. Geophys. Res.* 90, 4537–4555.
- Draper, D.S., 1991. Late Cenozoic bimodal magmatism in the northern Basin and Range Province of Southeastern Oregon. *J. Volcanol. Geotherm.* 47, 299–328.
- Dueker, K., Yuan, H., Zurek, B., 2001. Thick-structured Proterozoic lithosphere of the Rocky Mountain region. *GSA Today* 11, 4–9.

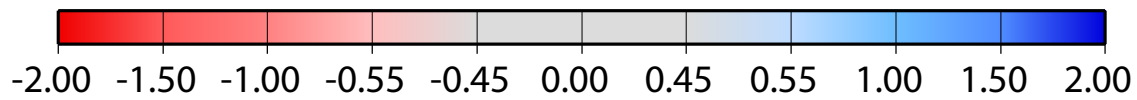
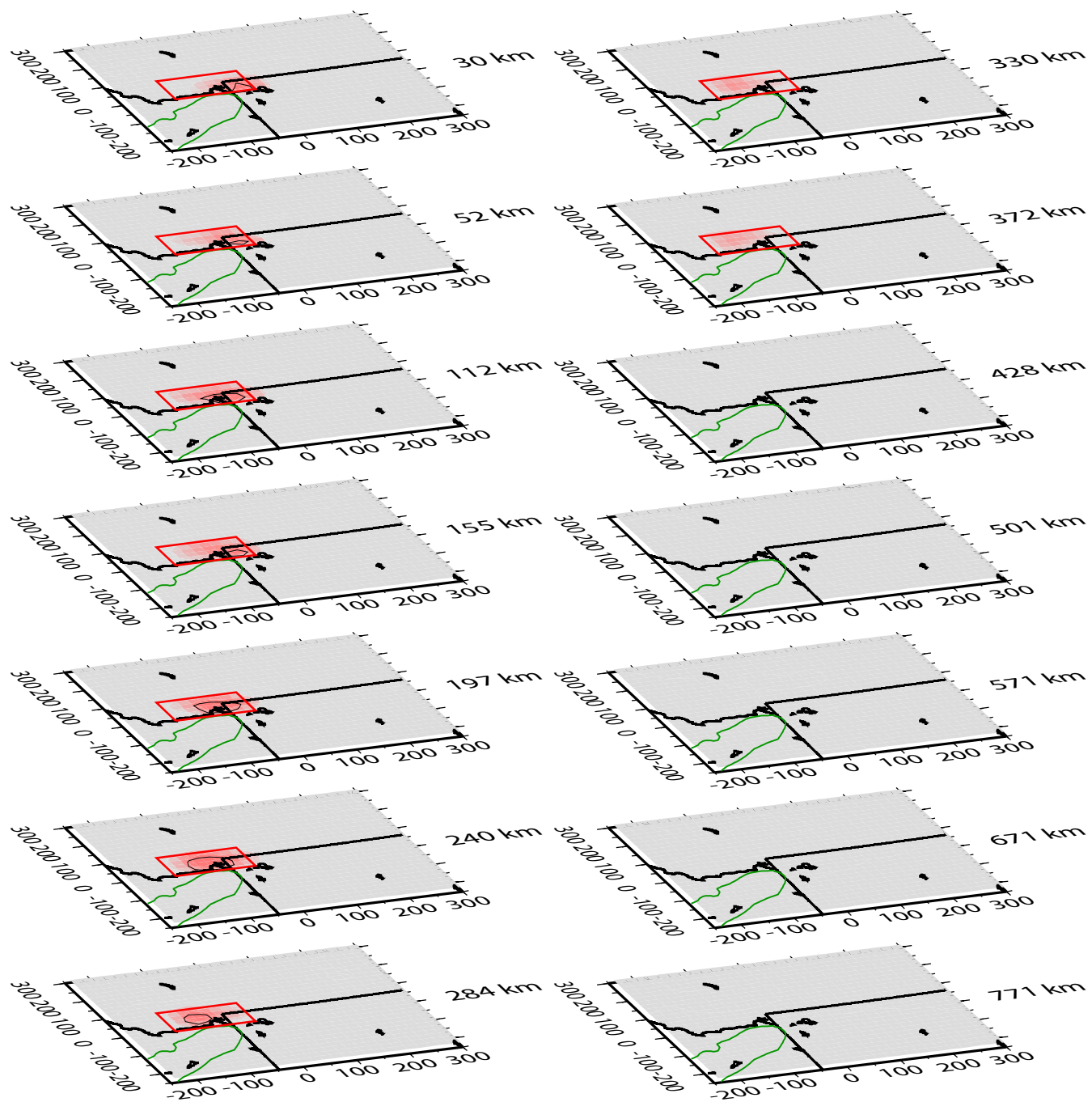
- Duncan, R.A., 1982. A captured island chain in the Coast Range of Oregon and Washington. *J. Geophys. Res.* 87, 10,827–10,837.
- Dzurisin, D., Yamashita, K.M., 1987. Vertical surface displacements at Yellowstone caldera, Wyoming, 1976–1986. *J. Geophys. Res.* 92, 13,753–13,766.
- Dzurisin, D., Yamashita, K.M., Kleinman, J.W., 1994. Mechanisms of crustal uplift and subsidence at the Yellowstone caldera Wyoming. *Bull. Volcanol.* 56, 261–270.
- Eaton, G.P., Christiansen, R.L., Iyer, H.M., Pitt, A.M., Mabey, D.R., Blank, H.R., Zietz, L., Gettings, M.E., 1975. Magma beneath Yellowstone National Park. *Science* 188, 787–796.
- Farmer, G., DePaolo, D., 1983. Origin of Mesozoic and Tertiary Granite in the Western United States and Implications for Pre-Mesozoic Crustal Structure 1. Nd and Sr Isotopic Studies in the Geocline of the Northern Great Basin. *J. Geophys. Res.* 88 (B4), 3379–3401.
- Farnetani, C.G., Samuel, H., 2005. Beyond the thermal plume paradigm. *Geophys. Res. Lett.* 32, L07311. doi:10.1029/2005GL022360.
- Farrell, S., Husen, R.B., Smith, 2009. Earthquake swarm and b-value characterization of the Yellowstone volcano-tectonic system. *J. Volcanol. Geotherm. Res.* 188, 260–276.
- Favela, J., Anderson, D.L., 2000. Extensional tectonics and global volcanism. In: Boschi, E., Ekstrom, G., Morelli, A. (Eds.), *Problems in geophysics for the new millennium*. Editrice Compositori, Bologna, pp. 463–498.
- Fee, D., Dueker, K., 2004. Mantle transition zone topography and structure beneath the Yellowstone hotspot. *Geophys. Res. Lett.* 31, L18603. doi:10.1029/2004GL020636.
- Faul, U.H., Toomey, D.R., Waft, H.S., 1994. Late granular basaltic melt is distributed in thin, elongated inclusions. *Geophys. Res. Lett.* 21, 29–32.
- Foulger, G.R., 2002. Plumes, or plate tectonic processes? *Astron. Geophys.* 43, 6.19–6.23.
- Foulger, G.R., Natland, J.H., Presnall, D.C., Anderson, D.L. (Eds.), 2005. *Plates, Plumes, and Paradigms*: Geol. Soc. Am. Spec., Vol. 388. Geol. Soc. Am. Boulder, CO. 881 pp.
- Fournier, R.O., 1989. Geochemistry and dynamics of the Yellowstone National Park hydrothermal system. *Annu. Rev. Earth Planet. Sci.* 17, 13–53.
- Fournier, R.O., Pitt, A.M., 1985. The Yellowstone magmatic-hydrothermal system, U.S.A. In: Stone, C. (Ed.), 1985 International Symposium on Geothermal Energy. CA, Geothermal Resource Center, Davis, pp. 319–327.
- Geist, D., Richards, M., 1993. Origin of the Columbia Plateau and Snake River Plain: Deflection of the Yellowstone plume. *Geology* 21, 789–792.
- Glen, J.M.G., Ponce, D.A., 2002. Large-scale fractures related to the inception of the Yellowstone hotspot. *Geology* 30 (7), 647–650.
- Graham, D.W., Reid, M.R., Jordan, B.T., Grunder, A.L., Leeman, W.P., Lupton, J.E., 1993. Mantle source provinces beneath the northwestern USA delimited by helium isotopes in young basalts. *J. Volcanol. Geotherm. Res.* 188, 128–140.
- Gripp, A.E., Gordon, R.G., 2002. Young tracks of hotspots and current plate velocities. *Geophys. J. Int.* 150, 321–361.
- Hager, B.H., O'Connell, R.J., 1979. Kinematic models of large-scale flow in the earth's mantle. *J. Geophys. Res.* 84 (B3), 1031–1048.
- Hager, B. H., O'Connell, R. J., 1981. A simple global model of plate dynamics and Hammond, W. C., Humphreys, E. D., 2000. Upper mantle seismic wave velocity: Effects of realistic partial melt geometries. *J. Geophys. Res.* 105, 10,975–10,986.
- Haller, K.M., Wheeler, R.L., Rukstales, K.S., 2002. Documentation of changes in fault parameters for the 2002 National Seismic Hazard Maps–Conterminous United States except California. U. S. Geol. Surv. Open-File Rep. 02-467. U. S. Geol. Surv. Denver, CO. 34 pp.
- Hammond, W.C., Humphreys, E.D., 2000. Upper mantle seismic wave velocity: Effects of realistic partial melt geometries. *J. Geophys. Res.* 105 (B5), 10,957–10,986.
- Hanan, B.B., Shervais, J.W., Vetter, S.K., 2008. Yellowstone plume-continental lithosphere interaction beneath the Snake River Plain. *Geology* 36, 51–54.
- Hart, W.K., Carlson, R.W., 1987. Tectonic controls on magma genesis and evolution in the northwestern United States. *J. Volcanol. Geotherm. Res.* 32, 119–135.
- Hernlund, J.W., Tackley, P.J., Stevenson, D.J., 2008. Buoyant melting instabilities beneath extending lithosphere: 1 Numerical models. *J. Geophys. Res.* 113, B04405. doi:10.1029/2006JB004862.
- Herzberg, C., Zhang, J., 1996. Melting experiments on anhydrous peridotite KLB-1: Compositions of magmas in the upper mantle and transition zone. *J. Geophys. Res.* 101 (B4), 8271–8295.
- Hill, D.P., 1992. Temperatures at the base of the seismogenic crust beneath the Long Valley caldera, California, and the Phlegrean Fields caldera, Italy. In: Gasparini, P. (Ed.), *Proceedings in Volcanology: Volcanic Seismology*, Vol. 3. Springer-Verlag, Berlin, pp. 432–460.
- Hooper, P.R., Hawkesworth, C.J., 1993. Isotopic and geochemical constraints on the origin and evolution of the Columbia River basalt. *J. Pet.* 34 (6), 1203–1246.
- Hughes, S.S., McCurry, M., 2002. Bulk major and trace element evidence for a time-space evolution of Snake River Plain rhyolites Idaho. *Idaho Geol. Surv. Bull.* 30, 161–176.
- Husen, S., Smith, R.B., 2004. Probabilistic earthquake relocation in three-dimensional velocity models for the Yellowstone National Park Region Wyoming. *Bull. Seismol. Soc. Am.* 94 (3), 880–896.
- Husen, S., Smith, R.B., Waite, G.P., 2004. Evidence for gas and magmatic sources beneath the Yellowstone volcanic field from seismic tomographic imaging. *J. Volcanol. Geotherm. Res.* 131, 397–410. doi:10.1016/S0377-0273(03)00416-5.
- Ito, G., van Keken, P.E., 2007. Hotspots and melting anomalies. In: Bercovici, D. (Ed.), *Mantle Dynamics, Treatise on Geophysics*, vol. 7. Elsevier Press, Amsterdam, The Netherlands.
- Iyer, H.M., Evans, J.R., Zandt, G., Stewart, R.M., Coakley, J.M., Roloff, J.N., 1981. A deep low-velocity body under the Yellowstone caldera Wyoming: Delineation using teleseismic P-wave residuals and tectonic interpretation: Summary. *Geol. Soc. Am. Bull.* 92 (11), 792–798.
- Jackson, I., Paterson, M.S., Fitzgerald, J.D., 1992. Seismic wave dispersion and attenuation in Aheim dunite: an experimental study. *Geophys. J. Int.* 108, 517–534.
- Jones, C.H., Unruh, J.R., Sonder, L.J., 1996. The role of gravitational potential energy in active deformation in the southwestern United States. *Nature* 381, 37–41.
- Jordan, M., 2003. JI-3D A new approach to high resolution regional seismic tomography: theory and applications. PhD thesis, University of Göttingen, Göttingen, Germany.
- Jordan, M., Smith, R. B., Waite, G. P., 2004. Tomographic Images of the Yellowstone Hotspot Structure. *Eos Tran. AGU* 85(47), Fall Meet. Suppl., Abstract V51B-0556.
- Jordan, M., Smith, R. B., Puskas, C., Farrell, J., Waite, G., 2005. The Yellowstone hotspot and related plume: volcano-tectonics, tomography, kinematics and mantle flow. *Eos Trans. AGU*, 86(52), Fall Meet. Suppl., Abstract T51D-1388.
- Karato, S., 1993. Importance of anelasticity in the interpretation of seismic tomography. *Geophys. Res. Lett.* 20, 1623–1626.
- Karato, S., Jung, H., 1998. Water, partial melting and the origin of the seismic low velocity and high attenuation zone in the upper mantle. *Earth Planet. Sci. Lett.* 157, 193–207.
- Kawamoto, T., Holloway, J., 1997. Melting temperature and partial melt chemistry of H₂O-saturated mantle peridotite to 11 gigapascals. *Science* 276, 240–243.
- Kennedy, B.M., Lynch, M.A., Reynolds, J.H., Smith, S.P., 1985. Intensive sampling of noble gases in fluids at Yellowstone: I Early overview of the data; regional patterns. *Geochim. Cosmochim. Acta* 49, 1251–1261.
- Kennett, B.L.N., Engdahl, E.R., 1991. Traveltimes for global earthquake location and phase identification. *Geophys. J. Int.* 105 (2), 429–465. doi:10.1111/j.1365-246X.1991.tb06724.x.
- Keyser, M., Ritter, J.R.R., Jordan, M., 2002. 3D shear-wave velocity structure of the Eifel plume. Germany. *Earth Planet. Sci. Lett.* 203 (1), 59–82.
- Kissling, E., 1988. Geotomography with local earthquake data. *Rev. Geophys.* 26, 659–698.
- Kuntz, M.A., Covington, H.R., Schorr, L.J., 1992. An overview of basaltic volcanism of the eastern Snake River Plain. In: Link, P.K., Kuntz, M.A., Platt, L.B. (Eds.), *Regional Geology of Eastern Idaho and Western Wyoming*: Geo. Soc. Amer., Memoir, vol. 179. Geological Society of America, Boulder, CO, pp. 227–267.
- Laske, G., Collins, J.A., Wolfe, C.J., Weeraratne, D.S., Solomon, S., Detrick, R.S., Orcutt, J.A., Bercovici, D.A., Hauri, E.H., 2006. The Hawaiian PLUME project successfully completes its first deployment. *Eos Trans., AGU, Fall Supplement* 87, 13B06=567.
- Leeman, W.P., 1982. Development of the Snake River Plain-Yellowstone Plateau province, Idaho and Wyoming: An overview and petrologic model. In: Bonnichsen, B., Breckenridge, R.M. (Eds.), *Cenozoic Geology of Idaho: Idaho Bureau of Mines and Geology Bulletin*, vol. 26. Idaho Bureau of Mines and Geology, Moscow, ID, pp. 155–178.
- Leeman, W.P., Schutt, D.L., Hughes, S.S., 2009. Crustal structure of the Yellowstone caldera from delay-time analyses and correlation with gravity data. *J. Volcanol. Geotherm. Res.* 188, 57–67.
- Lehman, J.A., Smith, R.B., Schilly, M.M., Braile, L.W., 1982. Crustal structure of the Yellowstone caldera from delay-time analyses and correlation with gravity data. *J. Geophys. Res.* 84, 2713–2730.
- Lowenstern, J.B., Hurwitz, S., 2008. Monitoring a supervolcano in repose: Heat and volatile flux at the Yellowstone caldera. *Elements*. doi:10.2113/GSELEMENTS.4.1.35.
- Lowry, A.R., Ribe, N.M., Smith, R.B., 2000. Dynamic elevation of the Cordillera, western United States. *J. Geophys. Res.* 105 (B10), 23,371–23,390.
- Lynch, D., Smith, R.B., Benz, H.M., 1997. Three-dimensional tomographic inversion of crust and upper mantle structure of the eastern Basin Range-Rocky Mountain transition from earthquake and regional refraction data. Abstracts from the 9th Annual IRIS Workshop, IRIS Consortium, Breckenridge, CO.
- MacLeod, N.S., Walker, G.W., McKee, E.H., 1976. Geothermal significance of eastward increase in age of upper Cenozoic rhyolitic domes in southeastern Oregon. Proceedings of the Second United Nations Symposium on the Development and Use of Geothermal Resources 1. U.S. Government Printing Office, Washington, D.C., pp. 456–474.
- Malamud, B.D., Turcotte, D.L., 1999. How many plumes are there? *Earth Planet. Sci. Lett.* 174, 113–124.
- Mason, B.G., Pyle, D.M., Oppenheimer, C., 2004. The size and frequency of the largest explosive eruptions on Earth. *Bull. Volcanol.* 66 (8), 735–748. doi:10.1007/s00445-004-0355-9.
- Matthews, V., Anderson, C.E., 1973. Yellowstone convection plume and the break-up of the western United States. *Nature* 243, 158–159.
- Megnin, C., Romanowicz, B., 2000. The three-dimensional shear velocity structure of the mantle from the inversion of body, surface and higher-mode waveforms. *Geophys. J. Int.* 143 (3), 709–728. doi:10.1046/j.1365-246X.2000.00298.x.
- Milbert, D.G., 1991. Computing GPS-derived orthometric heights with the GEIOD90 geoid height model. Technical Papers of the 1991 ACSM-ASPRS Fall Convention. American Congress on Surveying and Mapping, Washington, D.C., pp. A46-55.
- Miller, D.S., Smith, R.B., 1999. P and S velocity structure of the Yellowstone volcanic field from local earthquake and controlled-source tomography. *J. Geophys. Res.* 104, 15,105–15,121.
- Montelli, R., Nolet, G., Dahlen, F., Masters, G., Engdahl, E.R., Hung, S.H., 2004. Finite-frequency tomography reveals a variety of plumes in the mantle. *Science* 303, 338–343. doi:10.1126/science.1092485.
- Morgan, W.J., 1971. Convection plumes in the lower mantle. *Nature* 230, 42–43.
- Morgan, W.J., 1972. Plate motions and deep mantle convection. *Geol. Soc. Am. Memoir* 132, 7–22.
- Morgan, L.A., McIntosh, W.C., 2005. Timing and development of the Heise volcanic field, Snake River Plain, Idaho, western USA. *Geol. Soc. Am. Bull.* 117 (3/4), 288–306.
- Morgan, L.A., Doherty, D.J., Leeman, W.P., 1984. Ignimbrites of the eastern Snake River Plain: Evidence for major caldera-forming eruptions. *J. Geophys. Res.* 89 (B10), 8665–8678.
- Morgan, J.P., Morgan, W.J., Price, E., 1995. Hotspot melting generates both hotspot volcanism and a hotspot swell? *J. Geophys. Res.* 100, 8045–8062.

- Müller, R.D., Royer, J.-Y., Lawver, L.A., 1993. Revised plate motions relative to the hotspots from combined Atlantic and Indian Ocean hotspot tracks. *Geol.* 16, 275–278.
- Myers, W.B., Hamilton, W., 1964. Deformation accompanying the Hebgen Lake earthquake of August 17, 1959. The Hebgen Lake, Montana earthquake of August 17, 1959.: U.S. Geol. Surv. Professional Paper, vol. 435. U.S. Geological Survey, Denver, CO, pp. 55–98.
- Nabelek J., Xia, G., 1995. Moment-tensor analysis using regional data: application to the 25 March, 1993, Scotts Mills, Oregon, earthquake. *Geophys. Res. Lett.* 22 (1), 13–16.
- Nash, B.P., Perkins, M.E., Christensen, J.N., Lee, D.C., Halliday, A., 2006. The Yellowstone hotspot in space and time: Nd and Hf isotopes in silicic magmas. *Earth Planet. Sci. Lett.* 247 (1–2), 143–156.
- Nolet, G., Karato, S., Montelli, R., 2006. Plume fluxes from seismic tomography. *Earth Planet. Sci. Lett.* 248, 685–699.
- Nolet, G.R., Allen, D., Zhao, D., 2007. Mantle plume tomography. *Geochem. Geol.* 241, 248–263. doi:10.1016/j.chemgeo.2007.01.022.
- Olson, P., Schubert, G., Anderson, C., 1987. Plume formation in the D' layer and the roughness of the core-mantle boundary. *Nature* 327, 409–413.
- O'Neill, C., Müller, D., Steinberger, B., 2005. On the uncertainties in hot spot reconstructions and the significance of moving hot spot reference frames. *Geochem. Geophys. Geosys.* 6 (4), Q04003. doi:10.1029/2004GC000784.
- Parsons, T., Thompson, G.A., Smith, R.P., 1994. Mantle plume influence on the Neogene uplift and extension of the U.S. western Cordillera? *Geology* 22, 83–86.
- Parsons, T., Thompson, G.A., Smith, R.P., 1998. More than one way to stretch: a tectonic model for extension along the plume track of the Yellowstone hotspot and adjacent Basin and Range Province. *Tect.* 17 (2), 221–234.
- Pechmann, J.C., Nava, S.J., Terra, F.M., Bernier, J.C., 2007. Local Magnitude Determinations for Intermountain Seismic Belt Earthquakes from Broadband Digital Data. *Bull. Seismol. Soc. Am.* 97 (2), 557–574.
- Pelton, J.R., Smith, R.B., 1982. Contemporary vertical surface displacements in Yellowstone National Park. *J. Geophys. Res.* 87, 2745–2761.
- Peng, X., Humphreys, E.D., 1998. Crustal velocity structure across the eastern Snake River Plain and the Yellowstone swell. *J. Geophys. Res.* 103, 7171–7186.
- Perkins, M.E., Nash, B.P., 2002. Explosive silicic volcanism of the Yellowstone hotspot: the ash fall tuff record. *Geol. Soc. Am. Bull.* 114 (3), 367–381.
- Perkins, M.E., Brown, F.H., Nash, W.P., McIntosh, W., Williams, S.K., 1998. Sequence, age, and source of silicic fallout tuffs in middle to late Miocene basins of the northern Basin and Range province. *Geol. Soc. Am. Bull.* 110 (3), 344–360.
- Pierce, K.L., Morgan, L.A., 1990. The track of the Yellowstone hotspot: Volcanism, faulting, and uplift. *U.S. Geol. Surv. Open-File Report 90-415*. *Geol. Surv., Denver, CO*, 49 pp.
- Pierce, K.L., Morgan, L.A., 1992. The track of the Yellowstone hot spot: Volcanism, faulting, and uplift. In: Link, P.K., Kuntz, M.A., Platt, L.B. (Eds.), *Regional Geology of Eastern Idaho and Western Wyoming*: Geological Society of America Memoir 179. Geological Society of America, Boulder, CO, pp. 1–53.
- Pierce, K.L., Morgan, L.A., 2009. Is the track of the Yellowstone hotspot driven by a deep mantle plume? – A review of volcanism, faulting, and uplift in light of new data. *J. Volcanol. Geotherm. Res.* 188, 1–25.
- Pierce, K.L., Morgan, L.A., Saltus, R.W., 2000. Yellowstone plume head: Postulated tectonic relations to the Vancouver slab, continental boundaries. *U.S. Geol. Surv. Open-File Report 00-498*.
- Pierce, K.L., Morgan, L.A., Saltus, R.W., 2002. Yellowstone plume head: Postulated relations to the Vancouver slab, continental boundaries, and climate. In: Bonnicksen, B., White, C.M., McCurry, Michael (Eds.), *Tectonic and Magmatic Evolution of the Snake River Plain Volcanic Province*: Idaho Geological Survey Bulletin, vol. 30, pp. 5–33.
- Piper, J. D. A., Proterozoic crustal distribution, mobile belts and apparent polar movements. *Nature* 251: 381–384.
- Pitt, A.M., Weaver, C.S., Spence, W., 1979. The Yellowstone Park earthquake of June 30, 1975. *Bull. Seismol. Soc. Am.* 69, 187–205 *Geol. Surv., Denver, CO*, 39 pp.
- Puskas, C.M., Smith, R.B., 2009. Intraplate deformation and microplate tectonics of the Yellowstone Hotspot and surrounding western U.S. Interior. *J. Geophys. Res.* 114, B04410. doi:10.1029/2008JB005940.
- Puskas, C.M., Smith, R.B., Meertens, C.M., Chang, W.L., 2007. Crustal deformation of the Yellowstone-Snake River Plain volcanic system: campaign and continuous GPS observations, 1987–2004. *J. Geophys. Res.* 112, B03401. doi:10.1029/2006JB004325.
- Richards, M.A., Hager, B.H., Sleep, N.H., 1988. Dynamically supported geoid highs over hotspots: Observation and theory. *J. Geophys. Res.* 93 (B7), 7690–7708.
- Richards, M.A., Duncan, R.A., Courtillot, V.E., 1989. Flood basalts and hot spot tracks: Plume heads and tails. *Science* 246, 103–107.
- Ritter, J.R.R., 2005. Small-scale mantle plumes: imaging and geodynamic aspects. In: Wenzel, F. (Ed.), *Perspectives in Modern Seismology*, Lecture Notes in Earth Sciences, vol. 105. Springer Verlag, Heidelberg, pp. 69–94. doi:10.1007/b97731.
- Ritter, J.R.R., Jordan, M., Christensen, U.R., Achauer, U., 2001. A mantle plume below the Eifel volcanic fields Germany. *Earth Planet. Sci. Lett.* 186 (1), 7–14.
- Rodgers, D.W., Hackett, W.R., Ore, H.T., 1990. Extension of the Yellowstone Plateau, eastern Snake River Plain, and Owyhee plateau. *Geology* 18, 1138–1141.
- Roman, D.R., Wang, Y.M., Henning, W., Hamilton, J., 2004. Assessment of the new national geoid height model-GEIOD3. *Surv. Land Info. Sci.* 64 (3), 153–162.
- Ruppel, E.T., 1972. Geology of pre-Tertiary rocks in the northern part of Yellowstone National Park, Wyoming, with a section on Tertiary laccoliths, sills, and stocks in and near the Gallatin Range, Yellowstone National Park. *Geology of Yellowstone National Park*: U.S. Geol. Surv. Prof. Pap. 729-A. U.S. Geol. Surv., Denver, CO, 66 pp.
- Saltzer, R.L., Humphreys, E.D., 1997. Upper mantle P wave velocity structure of the eastern Snake River Plain and its relationship to geodynamic models of the region. *J. Geophys. Res.* 102, 11,829–11,841.
- Schilly, M.M., Smith, R.B., Braile, L.W., Anson, J., 1982. 1978 Yellowstone-eastern Snake River Plain seismic profiling experiment: Data and upper crustal structure of the Yellowstone region. *J. Geophys. Res.* 87 (B4), 2692–2704.
- Schmitz, M., Heinschohn, W.D., Schilling, F.R., 1997. Seismic, gravity and petrological evidence for partial melt beneath the thickened Central Andean crust (21–23 S). *Tectonophysics* 270 (3–4), 313–326. doi:10.1016/S0040-1951(96)00217-X.
- Schutt, D.L., Humphreys, E.D., 2004. P and S wave velocity and V-P/V-S in the wake of the Yellowstone hot spot. *J. Geophys. Res.* 109, B01305. doi:10.1029/2003JB002442.
- Schutt, D.L., Dueker, K., 2008. Temperature of the plume layer beneath the Yellowstone Hotspot. *Geology* 36 (8), 623–628. doi:10.1130/G24089A.1.
- Schutt, D.L., Dueker, K., Yuan, H., 2008. Crust and upper mantle velocity structure of the Yellowstone hot spot and surroundings. *J. Geophys. Res.* 113, B03310. doi:10.1029/2007JB005109.
- Shervais, J.W., Hanan, B.B., 2008. Lithospheric topography, tilted plumes, and the track of the Snake River–Yellowstone hot spot. *Tectonics* 27, TC5004. doi:10.1029/2007TC002181.
- Shervais, J.W., Vetter, S.K., Hanan, B.B., 2006. Layered mafic sill complex beneath the eastern Snake River Plain: Evidence from cyclic geochemical variations in basalt. *Geology* 34, 365–368.
- Sigloch, K., McQuarrie, N., Nolet, G., 2008. Two-stage subduction history under N. America inferred from multiple-frequency tomography. *Nat. Geosci.* 1, 458–462. doi:10.1038/ngeo231.
- Simmons, N.A., Forte, A.M., Grand, S.P., 2006. Constraining mantle flow with seismic and geodynamic data: a joint approach. *Earth Planet. Sci. Lett.* 46, 109–124.
- Sleep, N.H., 1990. Hotspots and mantle plumes: some phenomenology. *J. Geophys. Res.* 95 (B5), 6715–6736.
- Sleep, N.H., 1992. Hotspot volcanism and mantle plumes. *Annu. Rev. Earth Planet. Sci.* 20, 19–43.
- Sleep, N.H., 2006. Mantle plumes from top to bottom. *Earth-Science Reviews* 77 (4), 231–271.
- Smith, R.B., 1977. Intraplate tectonics of the Western North American Plate. *Tectonophysics* 37, 323–336.
- Smith, R.B., 1978. Seismicity, crustal structure, and intraplate tectonics of the western Cordillera. In: Smith, R.B., Eaton, G.P. (Eds.), *Cenozoic Tectonics and Regional Geophysics of the Western Cordillera*: Geological Society of America Memoir 152. *Geol. Soc. Am. Bull.*, Boulder, CO, pp. 111–144.
- Smith, R.B., Sbar, M., 1974. Contemporary tectonics and seismicity of the Western United States with emphasis on the Intermountain Seismic Belt. *Geol. Soc. Am. Bull.* 85, 1205–1218.
- Smith, R.B., Bruhn, R.L., 1984. Intraplate extensional tectonics of the eastern Basin-Range: inferences on structural style from seismic reflection data, regional tectonics, and thermal-mechanical models of brittle-ductile deformation. *J. Geophys. Res.* 89 (B7), 5733–5762.
- Smith, R.B., Braile, L.W., 1984. Crustal structure and evolution of an explosive silicic volcanic system at Yellowstone National Park. *Studies In Geophysics: Explosive Volcanism: Inception, Evolution, and Hazards*. National Academy Press, Washington, D.C, pp. 96–109.
- Smith, R.B., Arabasz, W.J., 1991. Seismicity of the Intermountain Seismic Belt. In: Slemmons, D.B., Engdahl, E.R., Zoback, M.L., Blackwell, D.D. (Eds.), *Neotectonics of North America*. Geological Society of America, Boulder, CO, pp. 185–228.
- Smith, R.B., Braile, L.W., 1993. Topographic signature, space-time evolution, and physical properties of the Yellowstone-Snake River Plain volcanic system: the Yellowstone hotspot. In: Snoke, A.W., Steidtmann, J., Roberts, S.M. (Eds.), *Geology of Wyoming*: Geological Survey of Wyoming Memoir No. 5. Wyoming State Geological Survey, Laramie, WY, pp. 694–754.
- Smith, R.B., Braile, L.W., 1994. The Yellowstone hotspot. *J. Volcanol. Geotherm. Res.* 61, 121–187.
- Smith, R.B., Siegel, L., 2000. Windows into the Earth's interior; The geologic story of Yellowstone and Grand Teton National Parks. Oxford University Press. ISBN-13: 9780195105971, 256 pp.
- Smith, R.B., Shuey, R.T., Freidline, R., Otis, R., Alley, L., 1974. Yellowstone Hot Spot: New magnetic and seismic evidence. *Geology* 2, 451–455.
- Smith, R.B., Shuey, R.T., Pelton, J.R., Bailey, J.P., 1977. Yellowstone Hot Spot, crustal properties from new earthquake and magnetic data. *J. Geophys. Res.* 82, 3665–3676.
- Smith, R.B., Braile, L.W., Schilly, M.M., Anson, J., Prodehl, C., Baker, M., Healey, J.H., Mueller, S., Greensfelder, R., 1982. The Yellowstone- eastern Snake River Plain seismic profiling experiment: Crustal structure of Yellowstone. *J. Geophys. Res.* 84, 2583–2599.
- Smith, R.B., Richins, W.D., Doser, D.I., Smith, R.B., Richins, W.D., Doser, D.I., 1985. The 1983 Borah Peak, Idaho, earthquake: Regional seismicity, kinematics of faulting, and tectonic mechanism. Workshop XXVIII on the "Borah Peak Earthquake", U.S. Geol. Surv. Open-File Report 85-290. U.S. Geological Survey, Denver, CO, pp. 236–263.
- Smith, R.P., Jackson, S.M., Hackett, W.R., 1996. Paleoseismology and seismic hazards evaluations in extensional volcanic terrains. *J. Geophys. Res.* 101 (B3), 6277–6292.
- Smith, R.B., Jordan, M., Puskas, C., Waite, G., Farrell, J., 2005. Geodynamic models of the Yellowstone Hotspot constrained by seismic and GPS imaging and volcano-tectonic data. 2005 Salt Lake City Annual Meeting, *Geol. Soc. Am. Abstract* 54-2.
- Sonder, L.J., Jones, C.H., 1999. Western United States Extension: How the West was widened. *Annu. Rev. Earth Planet. Sci.* 27, 417–462.
- Sparlin, M.A., Braile, L.W., Smith, R.B., 1982. Crustal structure of the eastern Snake River Plain determined from ray trace modeling of seismic refraction data. *J. Geophys. Res.* 87 (B4), 2619–2633.
- Stachnik, J.C., Dueker, K., Schutt, D.L., Yuan, H., 2008. Imaging Yellowstone plume-lithosphere interactions from inversion of ballistic and diffusive Rayleigh wave dispersion and crustal thickness data. *Geochem. Geophys. Geosys.* 9 (6), Q06004. doi:10.1029/2008GC001992.
- Steck, L.K., Prothero, W.A., 1991. A 3-D raytracer for teleseismic body-wave arrival times. *Bull. Seis. Soc. Am.* 81, 1332–1339.
- Steinberger, B., 2000a. Plumes in a convecting mantle: models and observations from individual hotspots. *J. Geophys. Res.* 105, 11,127–11,152.

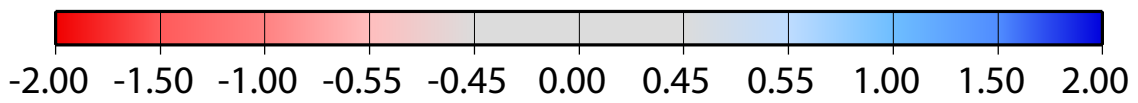
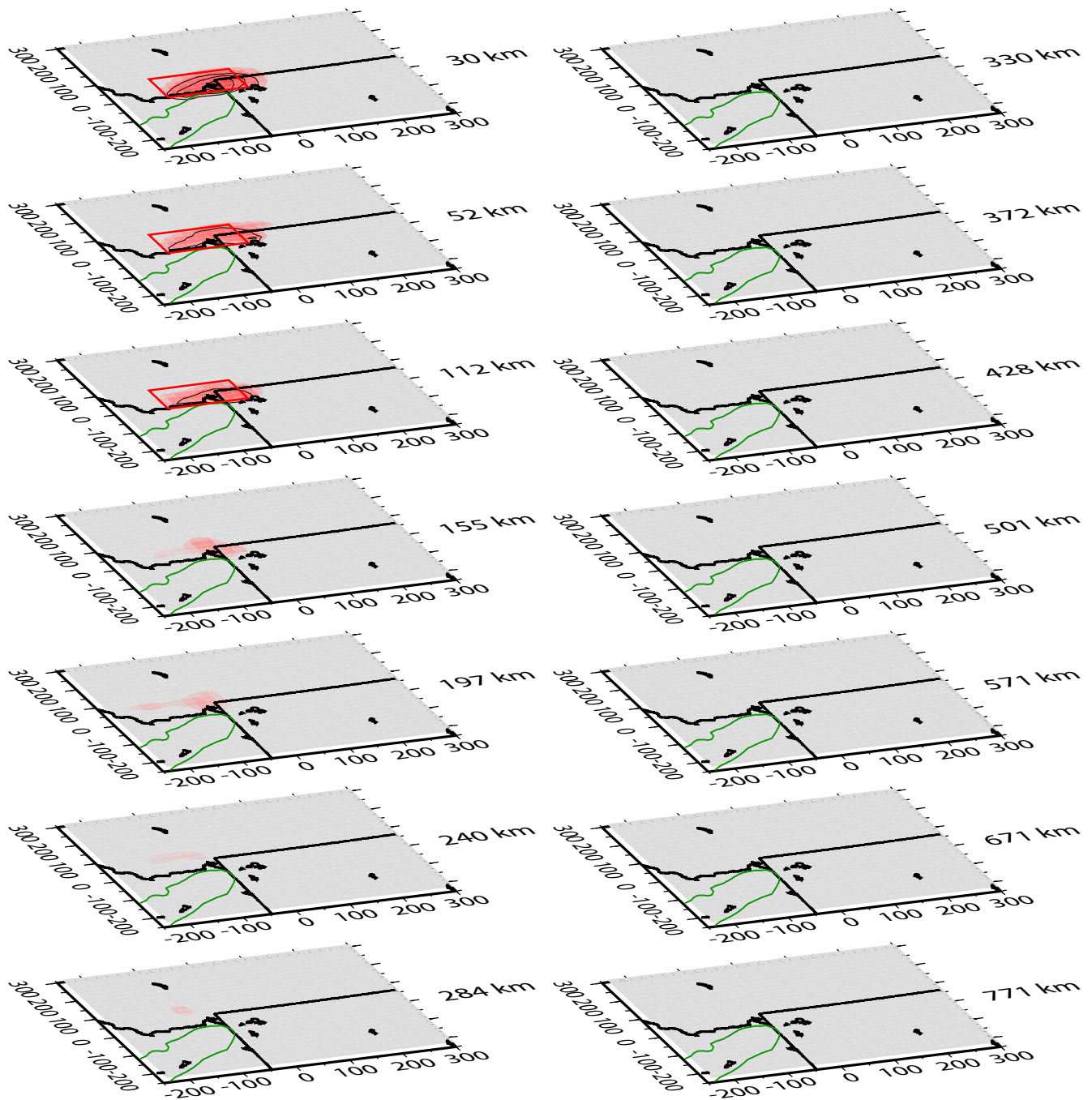
- Steinberger, B., 2000b. Slabs in the lower mantle – results of dynamic modelling compared with tomographic images and the geoid. *Phys. Earth Planet. Inter.* 118, 241–257.
- Steinberger, B., O'Connell, R.J., 1998. Advection of plumes in mantle flow; implications for hot spot motion, mantle viscosity and plume distribution. *Geophys. J. Int.* 132, 412–434.
- Steinberger, B., O'Connell, R.J., 2000. Effects of mantle flow on hotspot motion. *Geophys. Mono.* 121, 377–398.
- Steinberger, B., Antretter, A., 2006. Conduit diameter and buoyant rising speed of mantle plumes: implications for the motion of hot spots and shape of plume conduits. *Geochem. Geophys. Geosys.* 7, Q11018. doi:10.1029/2006GC001409.
- Steinberger, B., Calderwood, A.R., 2006. Models of large-scale viscous flow in the Earth's mantle with constraints from mineral physics and surface observations. *Geophys. J. Int.* 167, 1461–1481.
- Steinberger, B., Sutherland, R., O'Connell, R.J., 2004. Prediction of Emperor-Hawaii seamount locations from a revised model of global plate motion and mantle flow. *Nature* 430, 167–173.
- Su, W.-J., Woodward, R.L., Dziewonski, A.M., 1994. Degree 12 model of shear velocity heterogeneity in the mantle. *J. Geophys. Res.* 99, 6945–6980.
- Suppe, J., Powell, C., Berry, R., 1975. Regional topography, seismicity, Quaternary volcanism, and the present-day tectonics of the western United States. *Am. J. Sci.* 275 (A), 397–436.
- Takahashi, E., Nakajima, K., Wright, T.L., 1998. Origin of the Columbia River basalts: Melting model of a heterogeneous mantle plume head. *Earth Planet. Sci. Lett.* 162, 63–80.
- Tapley, B., Ries, J., Bettadpur, S., Chambers, D., Cheng, M., Condi, F., Gunter, B., Kang, Z., Nagel, P., Pastor, R., Pekker, T., Poole, S., Wang, F., 2005. GGM02 – An improved Earth gravity field model from GRACE. *J. Geod.* 79, 467–478. doi:10.1007/s00190-005-0480-z.
- Tarantola, A., Valette, B., 1982. Generalized nonlinear inverse problems solved using the least squares criterion. *Rev. Geophys. Space Phys.* 20, 219–232.
- Thompson, R.N., 1977. Columbia/Snake River-Yellowstone magmatism in the context of western U.S.A. Cenozoic geodynamics. *Tectonophysics* 39, 621–636.
- Van Decar, J.C., Crosson, R., 1990. Determination of teleseismic relative phase arrival times using multi-channel cross-correlation and least squares. *Bull. Seismol. Soc. Am.* 80, 150–159.
- van der Hilst, R.D., de Hoop, M.V., 2005. Banana-doughnut kernels and mantle tomography. *Geophys. J. Int.* 163, 956–961.
- Vasco, D.W., Johnson, L.R., Goldstein, N.E., 1988. Using surface displacement and strain observations to determine deformation at depth, with an application to Long Valley Caldera. *Calif. J. Geophys. Res.* 93, 3232–3242.
- Vasco, D.W., Smith, R., Taylor, C., 1990. Inversion of Yellowstone vertical displacements and gravity changes, 1923 to 1975–1977 to 1986. *J. Geophys. Res.* 95, 19,839–19,856.
- Vasco, D.W., Puskas, C.M., Smith, R.B., Meertens, C.M., 2007. Crustal deformation and source models of the Yellowstone volcanic field from geodetic data. *J. Geophys. Res.* 112, B07402. doi:10.1029/2006JB004641.
- Waite, G. P., 1999. Seismicity of the Yellowstone Plateau: Space-time patterns and stresses from focal mechanism inversion. M.S. thesis, University of Utah, Salt Lake City, UT.
- Waite, G.P., 2004. Upper mantle structure of the Yellowstone hotspot from teleseismic body-wave velocity tomography and shear-wave anisotropy. University of Utah, Salt Lake City, Utah, Ph.D. dissertation.
- Waite, G.P., Schutt, D.L., Smith, R.B., 2005. Models of lithosphere and asthenosphere anisotropic structure of the Yellowstone hot spot from shear wave splitting. *J. Geophys. Res.* 110, B11304. doi:10.1029/2004JB003501.
- Waite, G.P., Smith, R.B., 2002. Seismic evidence for fluid migration accompanying subsidence of the Yellowstone caldera. *J. Geophys. Res.* 107 (B9), 2177. doi:10.1029/2001JB000586.
- Waite, G.P., Smith, R.B., 2004. Seismotectonics and stress field of the Yellowstone volcanic plateau from earthquake first motions and other indicators. *J. Geophys. Res.* 109, B02301. doi:10.1029/2003JB002675.
- Waite, G.P., Smith, R.B., Allen, R.M., 2006. Vp and Vs structure of the Yellowstone hot spot: evidence for an upper mantle plume. *J. Geophys. Res.* 111 (B4), B04303. doi:10.1029/2005JB003867.
- Waschbusch, P., McNutt, M., 1994. Yellowstone: A continental midplate (Hot Spot) swell. *Geophys. Res. Lett.* 21 (16), 1703–1706.
- Weil, A.B., Van der Voo, R., Mac Niocaill, C., Meert, J.G., 1998. The Proterozoic supercontinent Rodinia: paleomagnetically derived reconstructions for 1100 to 800 Ma. *Earth Planet. Sci. Lett.* 154, 13–24.
- White, B.J.P., Smith, R.B., Farrell, J., Husen, S., Wong, I., 2009. Seismicity and earthquake hazard analysis of the Teton-Yellowstone region, Wyoming. *J. Volcanol. Geotherm. Res.* 188, 277–296.
- Whitehead, J.A., 1982. Instabilities of fluid conduits in a flowing Earth: are plates lubricated by the asthenosphere? *Geophys. J. R. Astr. Soc.* 70, 415–433.
- Wicks, C., Thatcher, W., Dzurisin, D., 1998. Migration of fluids beneath Yellowstone caldera inferred from satellite radar interferometry. *Science* 282 (5388), 458–462. doi:10.1126/science.282.5388.458.
- Wicks, C., Thatcher, W., Dzurisin, D., Svarc, J., 2006. Uplift, thermal unrest and magma intrusion at Yellowstone caldera. *Nature* 440, 72–75. doi:10.1038/nature04507.
- Wilson, J.T., 1963. A possible origin of the Hawaiian Islands. *Can. J. Phys.* 41, 863–870.
- Wolfe, C.J., Solomon, S.C., Laske, G., Collins, J.A., Detrick, R.S., Orcutt, J.A., Bercovici, D.A., Hauri, E.H., 2008. S-wave tomographic imaging of the mantle beneath the Hawaiian Islands from the PLUME deployments of ocean-bottom and land seismometers. *Eos Trans., AGU, Fall Supplement* 89:53, D121A–1725.
- Wüllner, U., Christensen, U.R., Jordan, M., 2006. Joint geodynamical and seismic modeling of the Eifel plume. *Geophys. J. Int.* 165 (1), 357–372. doi:10.1111/j.1365-246X.2006.02906.x.
- Xue, M., Allen, R.M., 2007. The fate of the Juan de Fuca plate: Implications for a Yellowstone plume head. *Earth Planet. Sci. Lett.* 264 (1), 266–276.
- Xue, M., Allen, R. M., 2009. Mantle structure beneath the western U.S. and its implications for convection processes. *J. Geophys. Res.*, (preprint).
- Yuan, H., Dueker, K., 2005. Teleseismic P-wave tomogram of the Yellowstone plume. *Geophys. Res. Lett.* 32, L07304. doi:10.1029/2004FL022056.
- Zeyen, H., Achauer, U., 1997. Joint inversion of teleseismic delay times and gravity anomaly data for regional structures: theory and synthetic examples. In: Fuchs, K. (Ed.), *Upper Mantle Heterogeneities from Active and Passive Seismology*. Kluwer Academic Publishers, Dordrecht, Netherlands, pp. 155–168.
- Zoback, M.L., Thompson, G.A., 1978. Basin and Range rifting in northern Nevada: Clues from a mid-Miocene rift and its subsequent offsets. *Geology* 6, 111–116.
- Zoback, M.D., Zoback, M.L., 1991. Tectonic stress field of North America and relative plate motions. In: Slemmons, D.B., Engdahl, E.R., Zoback, M.D., Blackwell, D.D. (Eds.), *Neotectonics of North America*. Geological Society of America, Boulder, CO, pp. 339–366.

WLWY Time Series

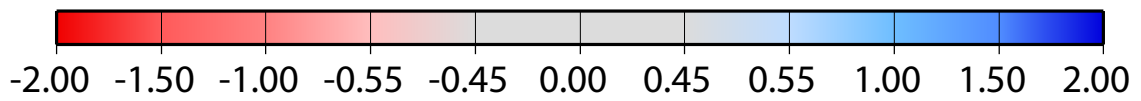
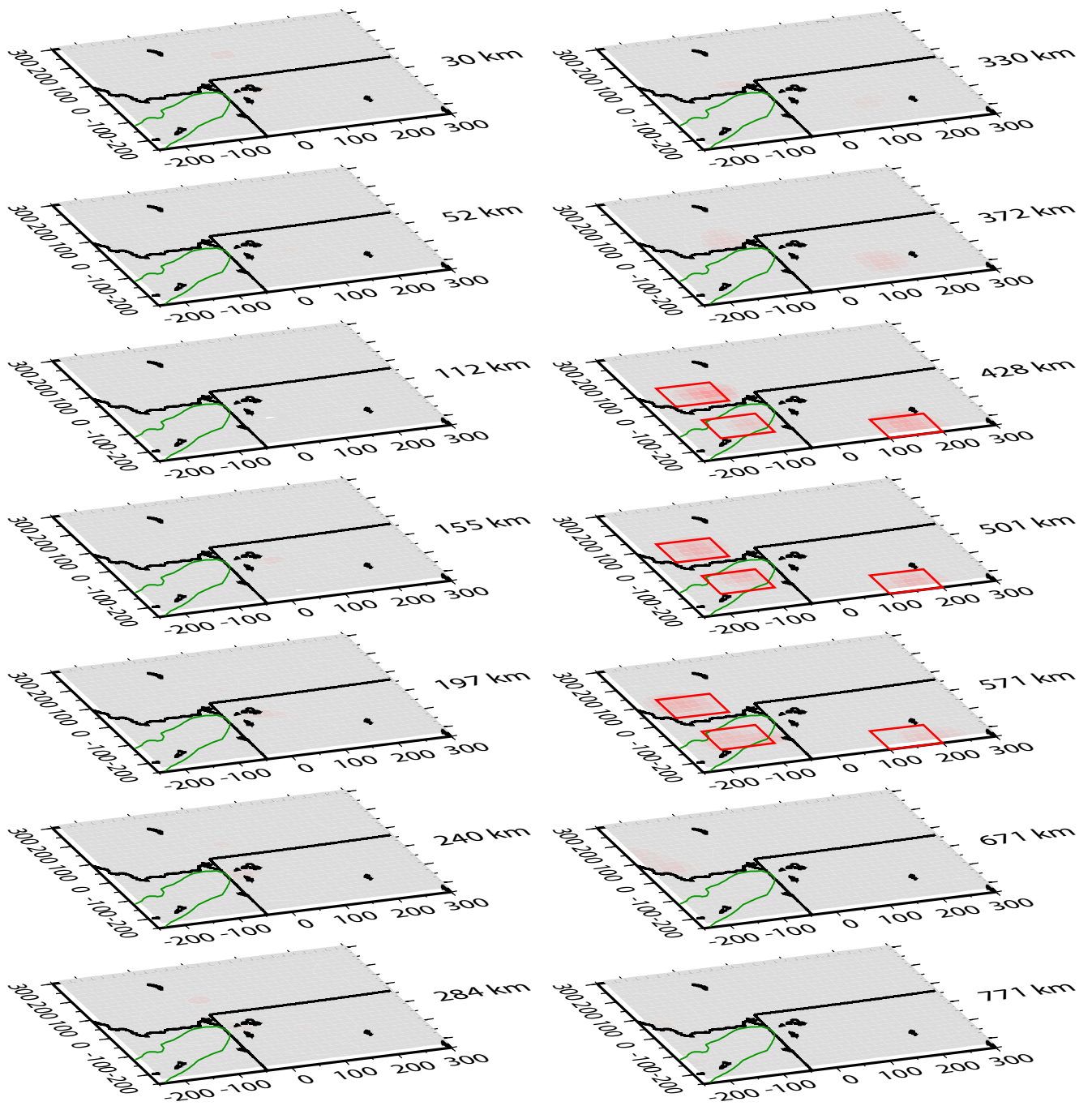




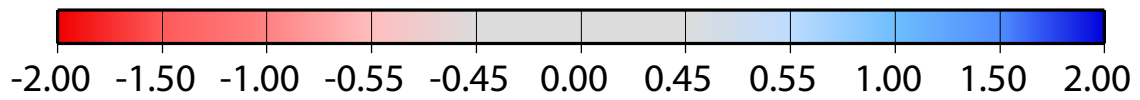
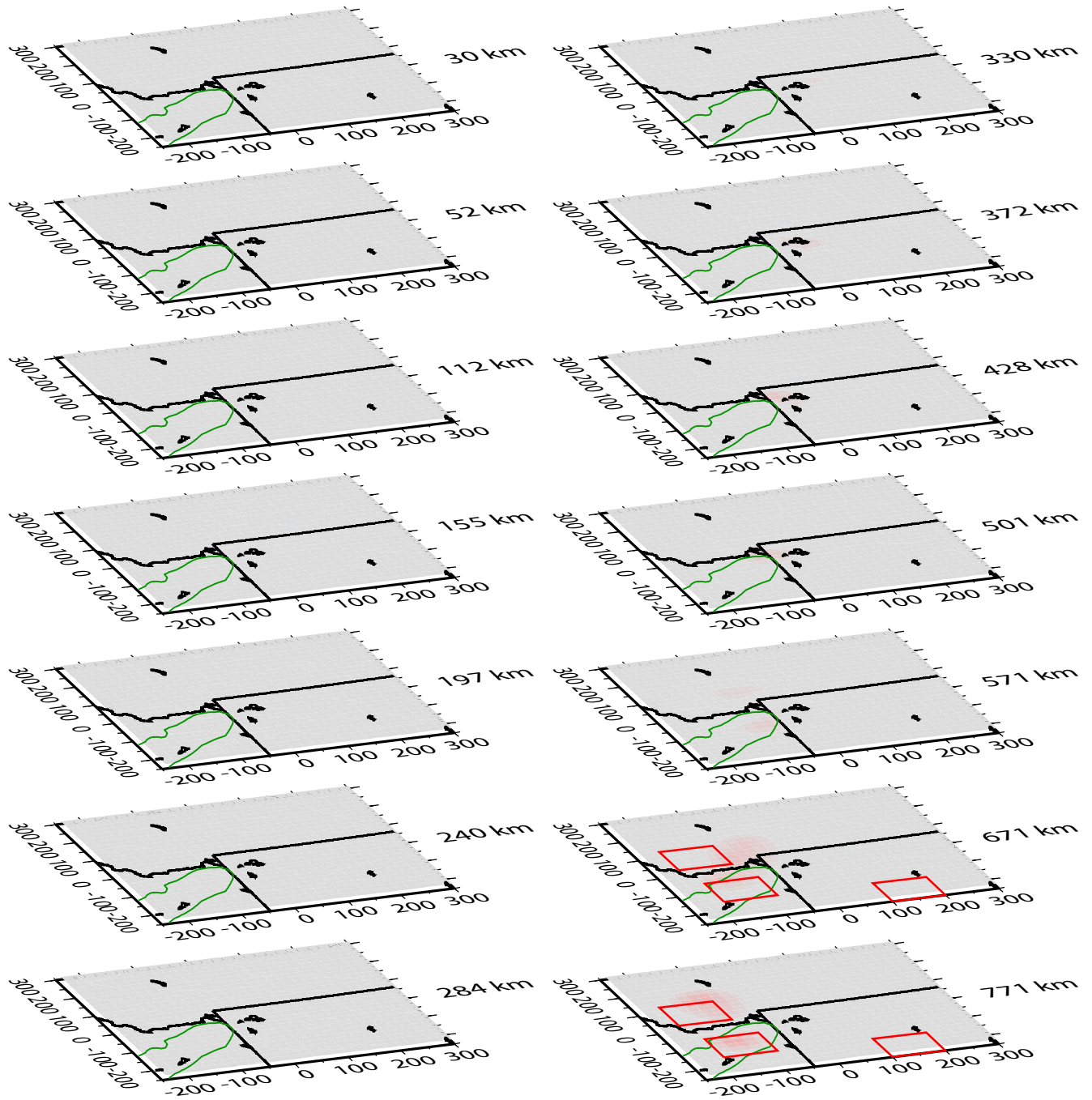
P-wave velocity perturbation (%)



P-wave velocity perturbation (%)

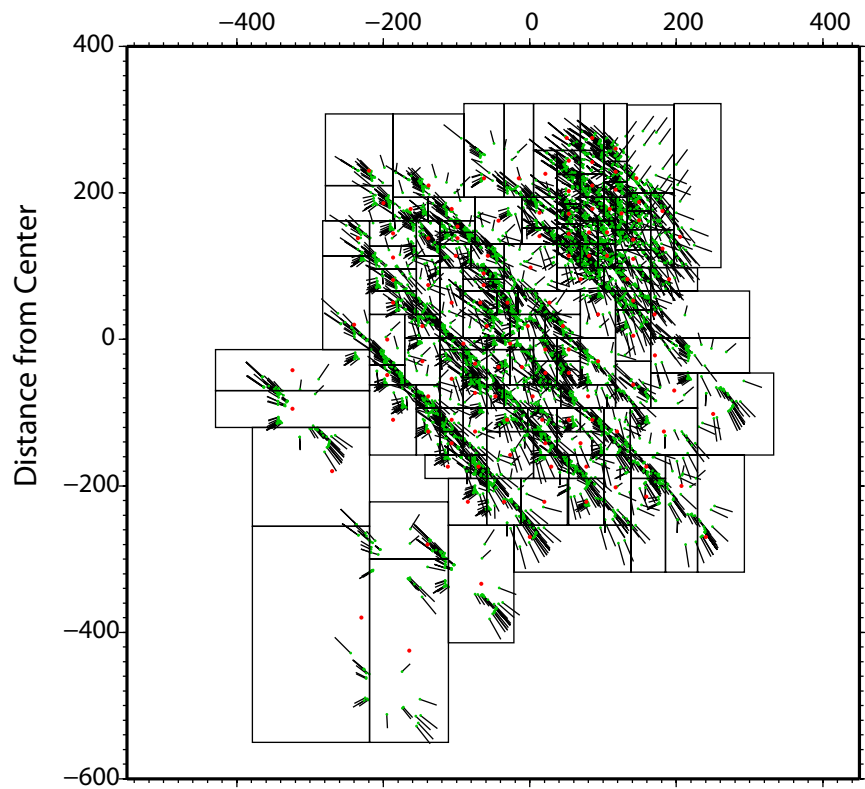


P-wave velocity perturbation (%)

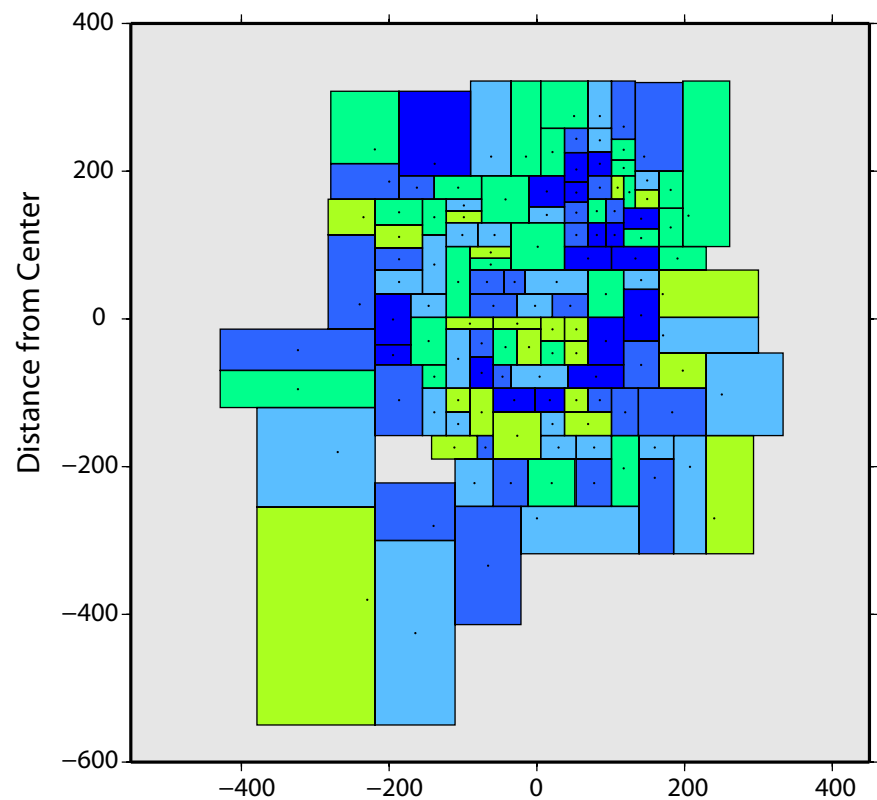


P-wave velocity perturbation (%)

Layer 9 (215–285 km)

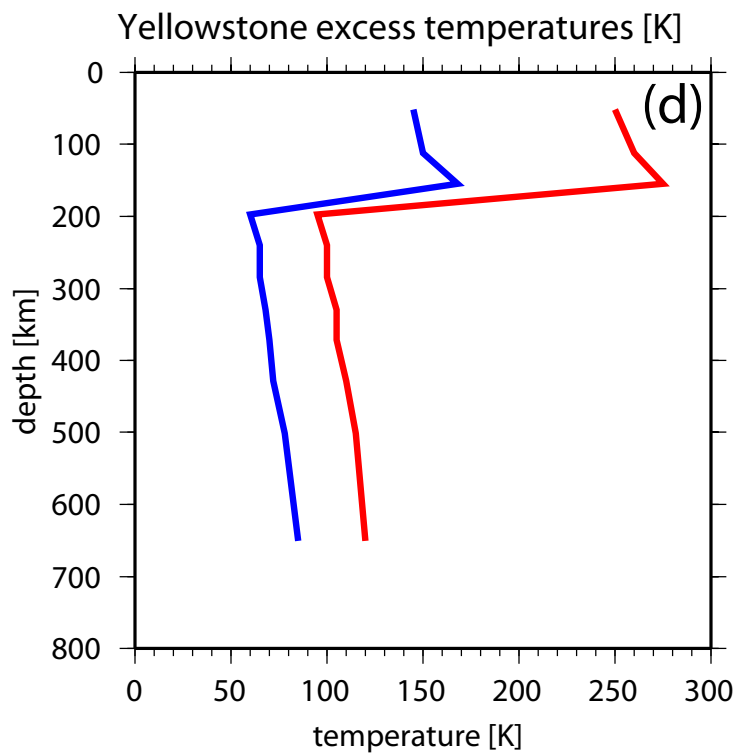
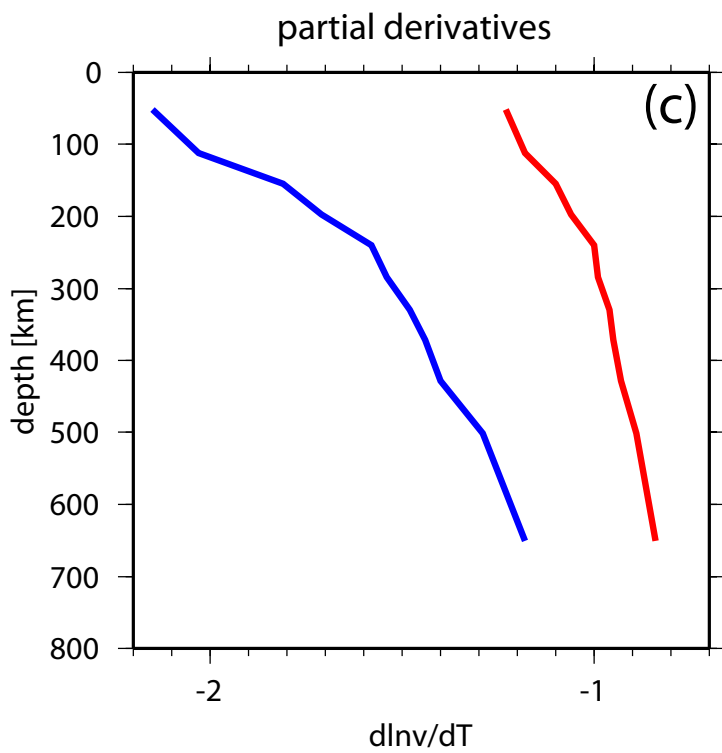
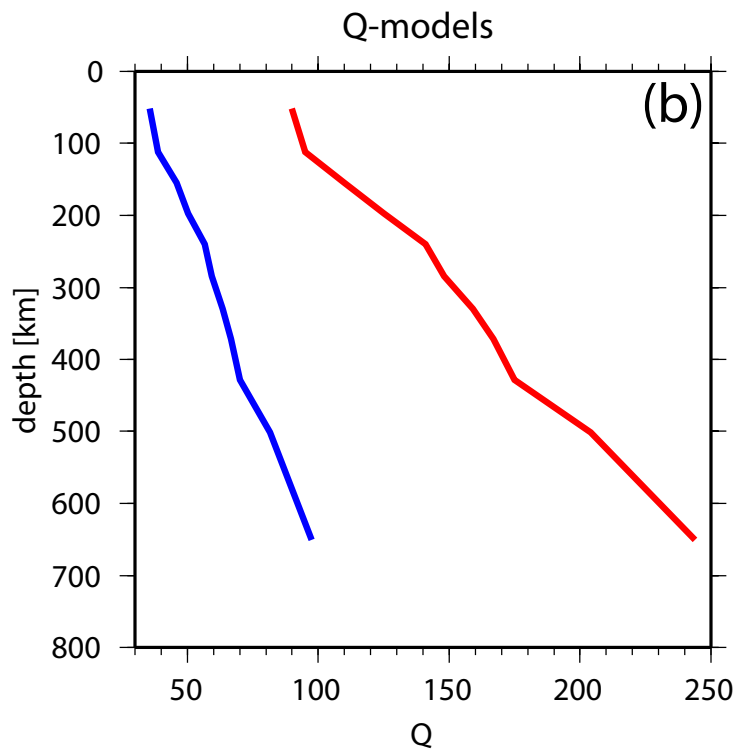
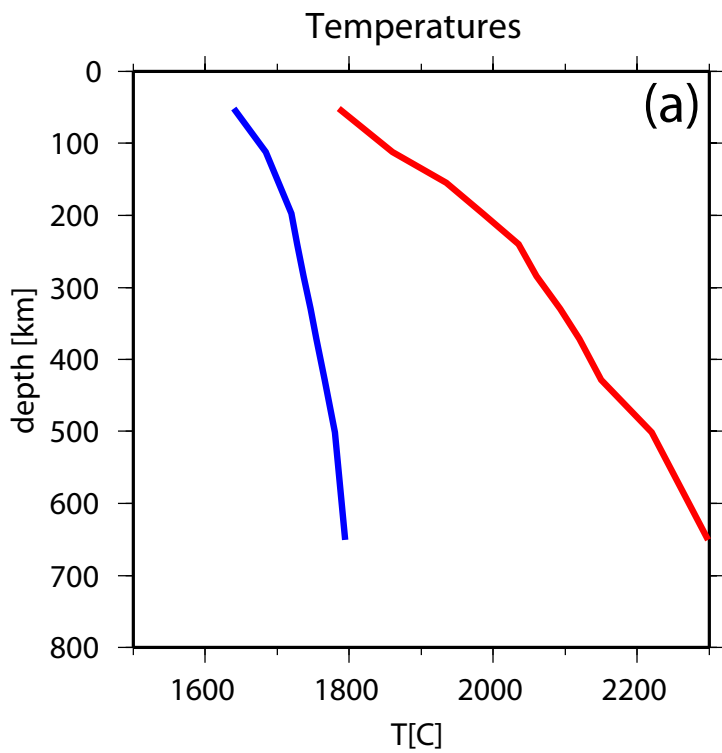


Layer 9



Distance from Center





1 **Supplemental Section 1: Tomographic Model Parameterization**

2 We employed a one-dimensional IASP91 whole-earth P-wave velocity (Kennett and
3 Engdahl, 1991) homogenous starting model. The model extends to 790 km depth and consists of 22
4 layers. Layers corresponding to the crustal structure at 14 km depth, the Moho, and the 410 km and
5 660 km discontinuities, respectively, were included as *a priori* information with their parameters
6 fixed during the inversion process by attributing small values in the *a priori* covariance matrix of
7 the velocity model parameters. The JI-3D program relies on an optimized parameterization
8 (Jordan, 2003) that is variable and performed strictly according to the information distribution in
9 the model space, i.e., the angular distribution of rays.

10 Blocks and nodes define the 3D velocity model. While a particular block defines the region
11 that contributes to the calculation of the each model parameter, the actual model parameter is
12 defined at a node, located in the center of the ray coverage of the block. Because the velocity is
13 interpolated linearly between the nodes, this also avoids artificial velocity jumps at block
14 boundaries. The parameterization itself is an iterative process that uses the diagonal elements of the
15 resolution matrix as a measure to decide if the model parameters are equally well resolved and the
16 inversion is stable. The resulting model is defined by small blocks and dense nodal spacing where
17 the ray distribution has the highest density. The block sizes in our model range from 10 km in the
18 best-sampled areas of the model space to several hundred kilometers at the lateral edges of the
19 model.

20 The crustal component of the *a priori* information was comprised of three-dimensional P-
21 wave models from high-resolution local earthquake tomography in the Yellowstone National Park
22 area (Husen et al., 2004) and of the entire Intermountain seismic belt by Lynch et al., (1997). For
23 the remaining crustal model area, the *a priori* information was provided by the global CRUST2.0
24 model (Bassin et al., 2000). Important contributions to the *a priori* crustal model are the two

25 resolved low-velocity bodies by Husen et al. (2004) in the mid to upper crust beneath Yellowstone.
26 The Moho topography and velocities also are taken from CRUST2.0, while the topography data at
27 410 and 660 km were obtained from a model by Fee and Dueker (2004). These data are
28 transformed into velocity contrasts of layers at the respective depths and also treated as *a priori*
29 information. The 95% confidence bounds of the depths of the 410 and 660 km discontinuities are
30 1-3 km (Fee and Dueker, 2004). The maximum effects of a 3 km error on the residuals are 0.013s
31 for the 410 km discontinuity and 0.015s for the 660 km discontinuity, which is an order of
32 magnitude smaller than the data errors. Hence, we do not expect any significant effect of these
33 uncertainties on our tomography results.

34 **Supplemental Section 2: Optimized Seismic Tomography Methodology.**

35 The inversion is performed in several steps, starting from a homogeneous model, until a
36 realistic model is obtained. The parameterization was checked and adapted for each step. In the
37 last step the final result was obtained after four iterations, i.e., after more iterations no further
38 variance improvement was obtained. The maximum variance improvement was 30.5%. Although
39 the achieved variance reduction is relatively low, the resolution power of the inversion is not
40 compromised. This low value is due to using large blocks to represent heterogeneous structure, so
41 that the data sampling these blocks often sample different velocity contrasts and thus contradict
42 each other. To reduce the effect of arbitrarily positioned blocks and nodes (with respect to the true
43 structure) we apply an offset and average procedure (Evans and Achauer, 1993) during the last
44 iteration step.

45 Checkerboard tests are often applied to examine the resolution of one or more layers at the
46 same time. However, due to the irregular parameterization in our approach, the ability to recover
47 the synthetic input structure depends on the block size and relative position of the cells of the

48 checkerboard with respect to the blocks of the inversion model. Therefore we do not consider
49 checkerboard tests as suitable in this case but instead used an equivalent “reconstruction” scheme.

50 The resolution of an inversion solution can also be assessed using either the full resolution
51 matrix or its diagonal elements to evaluate the spatial distribution of well and less well-resolved
52 model parameters. The inversion method applied in this paper is a new scheme that relies on the
53 optimized parameterization, i.e. to keep the diagonal elements of the resolution matrix constant. As
54 a consequence, the resolution matrix cannot be used to assess the resolution properties of the
55 inversion since it is designed to possess near identical values, yielding no further insight. Hence we
56 employ reconstruction tests to evaluate the resolution of our inversion results (see Fig. S2-S5).

57 **Supplemental Section 3: Seismic Model Reconstruction Tests**

58 Our first reconstruction test addresses the resolution of our model within the upper mantle in
59 terms of geometry and amplitudes, especially possible smearing effects along the main ray
60 directions. The synthetic structure consists of an anomaly in the shape of a rectangular pillar with a
61 P-wave velocity contrast of -1% (see Fig. S7). This anomaly extends vertically from 30 to 400 km
62 depth, with horizontal boundaries of -150 km and 0 km in EW, and -100 km and 0 km in NS
63 direction, which corresponds to the position of the imaged plume. The results of this test (Fig. S7)
64 show no signs of vertical smearing into the transition zone and below the boundaries of the original
65 anomaly. The recovered amplitude is generally lower than the input value of -1%. While from 30
66 km to 284 km depth, the relative perturbation amplitudes range between -1.0% and -0.8%, the
67 amplitudes are significantly lower (-0.6%) for the two deepest layers in 330 km and 372 km depth.
68 It is also visible that the maximum values of the amplitudes in each layer of the recovered structure
69 migrate from the SW corner at the top to the center of the structure at the bottom, which may be
70 linked to the main ray direction. However, the input structure is well resolved within the limits of
71 the modeling parameters and significant smearing is not observed.

72 The second reconstruction test examines if the imaged anomaly could be caused by a
73 downward smearing of a larger anomaly in the uppermost mantle along the main ray direction to
74 create an artificial plume tail tilting to the NW. The input anomaly of the corresponding
75 reconstruction test consists of a -3% P-wave anomaly located in three layers at 30 km, 52 km and
76 112 km depth. The horizontal extent of the anomaly is identical to the one described before. The
77 input anomaly could be well recovered within its original limits, with light vertical smearing mainly
78 into the two adjacent lower layers. Significant smearing in the main ray direction was not observed.
79 The recovered amplitudes of the P-wave velocity perturbations were -1.5% for the uppermost layer
80 on the anomaly and -1% for the other two layers of the structure.

81 The last two reconstruction tests examine the resolution of the plume and the blob-like
82 anomalies within and beneath the transition zone. In order to examine the resolution of these
83 structures within the transition zone, we utilize three synthetic -1% P-wave perturbation anomalies
84 placed in the layers at 428 km, 501 km, and 571 km depth. The horizontal boundaries of the
85 synthetic anomaly related to the plume are -200 km and -100 km in EW direction and 30 km and
86 130 km in NS direction. The boundaries of the anomaly related to the “blob” south of the plume
87 are -180 km and -80 km in EW and -150 km and -50 km in NS direction. Those of the “blob” east
88 of the plume are 100 km and 200 km in EW, and -250 km and -150 km in NS direction.

89 The plume-related anomaly is recovered in all three layers with a mean maximum P-wave
90 perturbation of \sim -0.5%. We observe light smearing in the predominant ray direction into the
91 immediately adjacent layers above and below the transition zone. The anomaly to the south of the
92 plume is recovered with similar maximum amplitudes of \sim -0.5%, but reduced size in the two upper
93 layers. Vertical smearing is not observed. The anomaly to the east of the plume is also observed
94 with the same maximum amplitude. However, the horizontal position of this structure in the

95 lowermost layer of the transition zone is shifted to the east, following the main ray direction in this
96 part of the model. We also observe weak upward smearing to the layer labeled 372 km.

97 We examine the resolution properties beneath the transition zone using three anomalies with
98 the same horizontal positions as described above to check for possible upward smearing. These
99 anomalies with -1% P-wave velocity perturbation are located in the two lowermost layers labeled
100 671 km and 771 km. The reconstruction test shows that the anomaly east of the plume cannot be
101 resolved sufficiently, while the other two anomalies could be recovered with an anomaly of \sim -0.4%
102 in the lowermost layer. The horizontal position is slightly shifted due to the coarse
103 parameterization, which does not match the anomalies. Likewise the anomaly recovered in the
104 layer labeled 671 km is not located on either of the original positions, but shifted according to the
105 parameterization. We also observe weak upward smearing of the anomalies into the transition
106 zone.

107 **Supplementary Section 4: Geoid Modeling Methodology**

108 Since both the reference values for the geoid data and the velocity and density models are
109 not well-resolved, the observed and the forward calculated geoid data have to be compared on a
110 relative basis. To do so, we shifted the forward modelled geoid profile so that its maximum
111 amplitude matches the peak of the observed geoid profile (Fig. 23c). This does not affect the lateral
112 position or the shape of the geoid.

113 The geoid data were taken along the profile at a 5-km spacing and are plotted in Fig. 23a.
114 The profile A-A' coordinates were adapted from the seismic tomography model (the origin of the
115 Yellowstone tomography coordinate system is located at kilometer 700 along the profile). Since
116 the geoid signal shows high-frequency components that are not associated with a deep plume model
117 and are likely of local tectonic or topographic origin, we applied a one-dimensional filter to the
118 geoid data using an optimum window length of 300 km to remove short-wavelength crustal

119 contributions. Since regional effects are obvious in the data but are not contained in the model, we
120 calculated the misfit between 250 km and 1000 km along the profile (Fig. 23c). Only the plume
121 effect is calculated and the surrounding velocity and density variations are not taken into account.

122 Density variations were forward calculated from the velocity perturbations assuming initial
123 B-values between 2 and 6 for each layer. The effect on the geoid of the resulting density structure
124 was calculated separately for each body based on the algorithms of Tsuboi (1954). The results were
125 then superimposed to give the full geoid signal. The B-values of bodies 5 to 9 were fixed to a
126 median B-value of 3.0, since the corresponding variation between the minimum and maximum
127 effect on the geoid surface expression is about 0.3 m for body 5 and even less for the deeper bodies.

128

129 **Electronic Supplement 1: Animation of the three-dimensional structure of the Yellowstone**
130 **plume**

131 Three-dimensional animated digital image of the tomographic images of the Yellowstone
132 plume, crustal magma chamber, and related features interpreted from this paper. This image can be
133 viewed in a QuickTime Player, mpg format, that is a free viewer, which can be downloaded from:
134 <http://www.apple.com/quicktime/download/>

135

136

137

138

139

140

141

142

143 **References**

144 Bassin, C., Laske, G., Masters, G., 2000. The current limits of resolution for surface wave
145 tomography in North America. *Eos Trans. AGU* 81 (48), F897.

146 Evans, J.R., Achauer, U., 1993. Teleseismic velocity tomography using the ACH-method. Theory
147 and application to continental scale studies. In: Iyer, H.M., Hirahara, K. (Eds.), *Seismic
148 Tomography Theory and Practice*. Chapman and Hall, London, pp. 319–360.

149 Tsuboi, C., 1954. A new and simple method for calculating the deflections of the vertical
150 from gravity anomalies with the aid of BESSEL FOURIER series. *Proc. Jpn. Acad.* 30 (6), 461–
151 466.